

# APPLIED COMPUTATIONAL ELECTROMAGNETICS SOCIETY JOURNAL

**Special Issue on Mode-inspired  
Antennas/Circuits for 5G/6G Applications**

**Guest Editors:**

Gang Zhang  
Xiao Zhang  
Yun-Peng Lyu  
Neng-Wu Liu  
Le Chang

October 2023  
Vol. 38 No. 10  
ISSN 1054-4887

The ACES Journal is abstracted in INSPEC, in Engineering Index, DTIC, Science Citation Index Expanded, the Research Alert, and to Current Contents/Engineering, Computing & Technology.

The illustrations on the front cover have been obtained from the ARC research group at the Department of Electrical Engineering, Colorado School of Mines

Published, sold and distributed by: River Publishers, Alsbjergvej 10, 9260 Gistrup, Denmark

# THE APPLIED COMPUTATIONAL ELECTROMAGNETICS SOCIETY

<http://aces-society.org>

## EDITORS-IN-CHIEF

**Atef Elsherbeni**

Colorado School of Mines, EE Dept.  
Golden, CO 80401, USA

**Sami Barmada**

University of Pisa, ESE Dept.  
56122 Pisa, Italy

## ASSOCIATE EDITORS

**Maokun Li**

Tsinghua University  
Beijing 100084, China

**Wei-Chung Weng**

National Chi Nan University, EE Dept.  
Puli, Nantou 54561, Taiwan

**Paolo Mezzanotte**

University of Perugia  
I-06125 Perugia, Italy

**Mauro Parise**

University Campus Bio-Medico of Rome  
00128 Rome, Italy

**Alessandro Formisano**

Seconda Università di Napoli  
81031 CE, Italy

**Luca Di Rienzo**

Politecnico di Milano  
20133 Milano, Italy

**Yingsong Li**

Harbin Engineering University  
Harbin 150001, China

**Piotr Gas**

AGH University of Science and Technology  
30-059 Krakow, Poland

**Lei Zhao**

Jiangsu Normal University  
Jiangsu 221116, China

**Riyadh Mansoor**

Al-Muthanna University  
Samawa, Al-Muthanna, Iraq

**Long Li**

Xidian University  
Shaanxi, 710071, China

**Sima Noghianian**

Commscope  
Sunnyvale, CA 94089, USA

**Lijun Jiang**

University of Hong Kong, EEE Dept.  
Hong Kong

**Steve J. Weiss**

US Army Research Laboratory  
Adelphi Laboratory Center (RDRL-SER-M)  
Adelphi, MD 20783, USA

**Nunzia Fontana**

University of Pisa  
56122 Pisa, Italy

**Shinishihiro Ohnuki**

Nihon University  
Tokyo, Japan

**Jiming Song**

Iowa State University, ECE Dept.  
Ames, IA 50011, USA

**Stefano Selleri**

DINFO - University of Florence  
50139 Florence, Italy

**Kubilay Sertel**

The Ohio State University  
Columbus, OH 43210, USA

**Toni Bjorninen**

Tampere University  
Tampere, 33100, Finland

**Yu Mao Wu**

Fudan University  
Shanghai 200433, China

**Giulio Antonini**

University of L'Aquila  
67040 L'Aquila, Italy

**Santanu Kumar Behera**

National Institute of Technology  
Rourkela-769008, India

**Fatih Kaburcuk**

Sivas Cumhuriyet University  
Sivas 58140, Turkey

**Antonio Musolino**

University of Pisa  
56126 Pisa, Italy

**Daniele Romano**

University of L'Aquila  
67100 L'Aquila, Italy

**Huseyin Savci**

Istanbul Medipol University  
34810 Beykoz, Istanbul

**Abdul A. Arkadan**

Colorado School of Mines, EE Dept.  
Golden, CO 80401, USA

**Alireza Baghai-Wadji**

University of Cape Town  
Cape Town, 7701, South Africa

**Zhixiang Huang**

Anhui University  
China

**Salvatore Campione**

Sandia National Laboratories  
Albuquerque, NM 87185, USA

**Marco Arjona López**

La Laguna Institute of Technology  
Torreon, Coahuila 27266, Mexico

**Amin Kargar Behbahani**

Florida International University  
Miami, FL 33174, USA

**Ibrahim Mahariq**

American University of the Middle East  
Kuwait and University of  
Turkish Aeronautical Association  
Turkey

**Kaikai Xu**

University of Electronic Science  
and Technology of China  
China

**Laila Marzall**

University of Colorado, Boulder  
Boulder, CO 80309, USA

**Sheng Sun**

University of Electronic Science and  
Tech. of China  
Sichuan 611731, China

## EDITORIAL ASSISTANTS

**Matthew J. Inman**  
University of Mississippi, EE Dept.  
University, MS 38677, USA

**Shanell Lopez**  
Colorado School of Mines, EE Dept.  
Golden, CO 80401, USA

## EMERITUS EDITORS-IN-CHIEF

**Duncan C. Baker**  
EE Dept. U. of Pretoria  
0002 Pretoria, South Africa

**Allen Glisson**  
University of Mississippi, EE Dept.  
University, MS 38677, USA

**Ahmed Kishk**  
Concordia University, ECS Dept.  
Montreal, QC H3G 1M8, Canada

**Robert M. Bevensee**  
Box 812  
Alamo, CA 94507-0516

**Ozlem Kilic**  
Catholic University of America  
Washington, DC 20064, USA

**David E. Stein**  
USAF Scientific Advisory Board  
Washington, DC 20330, USA

## EMERITUS ASSOCIATE EDITORS

**Yasushi Kanai**  
Niigata Inst. of Technology  
Kashiwazaki, Japan

**Mohamed Abouzahra**  
MIT Lincoln Laboratory  
Lexington, MA, USA

**Alexander Yakovlev**  
University of Mississippi, EE Dept.  
University, MS 38677, USA

**Levent Gurel**  
Bilkent University  
Ankara, Turkey

**Sami Barmada**  
University of Pisa, ESE Dept.  
56122 Pisa, Italy

**Ozlem Kilic**  
Catholic University of America  
Washington, DC 20064, USA

**Erdem Topsakal**  
Mississippi State University, EE Dept.  
Mississippi State, MS 39762, USA

**Alistair Duffy**  
De Montfort University  
Leicester, UK

**Fan Yang**  
Tsinghua University, EE Dept.  
Beijing 100084, China

**Rocco Rizzo**  
University of Pisa  
56123 Pisa, Italy

**Atif Shamim**  
King Abdullah University of Science and  
Technology (KAUST)  
Thuwal 23955, Saudi Arabia

William O'Keefe Coburn  
US Army Research Laboratory  
Adelphi, MD 20783, USA

**Mohammed Hadi**  
Kuwait University, EE Dept.  
Safat, Kuwait

**Amedeo Capozzoli**  
Univerita di Naoli Federico II, DIETI  
I-80125 Napoli, Italy

**Wenxing Li**  
Harbin Engineering University  
Harbin 150001, China

**Qiang Ren**  
Beihang University  
Beijing 100191, China

## EMERITUS EDITORIAL ASSISTANTS

**Khaleb ElMaghoub**  
Trimble Navigation/MIT  
Boston, MA 02125, USA

**Kyle Patel**  
Colorado School of Mines, EE Dept.  
Golden, CO 80401, USA

**Christina Bonnington**  
University of Mississippi, EE Dept.  
University, MS 38677, USA

**Anne Graham**  
University of Mississippi, EE Dept.  
University, MS 38677, USA

**Madison Lee**  
Colorado School of Mines, EE Dept.  
Golen, CO 80401, USA

**Allison Tanner**  
Colorado School of Mines, EE Dept.  
Golden, CO 80401, USA

**Mohamed Al Sharkawy**  
Arab Academy for Science and Technology, ECE Dept.  
Alexandria, Egypt

## **OCTOBER 2023 REVIEWERS**

**Le Chang  
Neng-Wu Liu  
Yun-Peng Lyu  
Gang Zhang  
Xiao Zhang**

TABLE OF CONTENTS

Compact Integrated Circular Polarization Filtering Antenna based on SIW Cavity  
Qiyue Gao, Yuyao Zhu, Xinyu Yang, and Rui Li ..... 756

Compact Series-fed Circularly-polarized Patch Array based on Microstrip Line  
Gengming Wei, Le Chang, and Yu Wu ..... 761

Low-profile Dual-polarized Filtering Antenna with Improved Gain and Impedance  
Bandwidth using Characteristic Mode Analysis  
Zong-Zhuo Wang, Neng-Wu Liu, and Liang Fang ..... 767

Wideband Center-fed Stacked Patch Circularly Polarized Antenna used in Phased Array  
Jiaxin Wang, Xiao Liu, Pengfei Zhang, Zheng Xu, Anqi Li, Zhengtian Chen,  
and Jin Fan ..... 774

Miniaturized Wideband Circularly Polarized Triangular Patch Antennas based on  
Characteristic Mode Analysis  
Tian-Long Yang, Xiao Zhang, Qiong-Sen Wu, and Tao Yuan ..... 783

A Low-profile Dual-band Dual-polarization Co-aperture Array Antenna with High  
Isolation  
Liang-Xin Xia, Qi lei Zhou, Neng-Wu Liu, and Guang Fu ..... 792

A 4-Element UWB MIMO Antenna System with High Isolation Performance  
Tongyu Ding, Haobin Yang, Zhiwei Chen, Zhen Lin, Bin He, and Chong-Zhi Han ..... 799

Rigorous Analysis and Design of Resistor-Loaded Patch Antennas with Flexible Gain for  
Indoor Radar Sensors  
Shu-Wei Yu, Xiao Zhang, Qiong-Sen Wu, Lei Zhu, Tao Yuan, and Xian-Qin Hu ..... 807

Four-way SIW Filtering Power Divider with In- and Out-of-phase Characteristics and  
Large Power Division Ratio  
Minghan Shu, Nengcai Huang, Qiyue Gao, Chenxin Ma, and Xin Zhou ..... 817

A Low-power, High-gain and Excellent Noise Figure GaN-on-SiC LNA Monolithic  
Microwave Integrated Circuit (MMIC) operating at *Ka*-band for 5G/6G Application  
Zhou Dai, Chunyu Li, Junda Yan, Tiancheng Zhang, and Huaguang Bao ..... 822

# Compact Integrated Circular Polarization Filtering Antenna based on SIW Cavity

Qiyue Gao<sup>1</sup>, Yuyao Zhu<sup>1</sup>, Xinyu Yang<sup>1</sup>, and Rui Li<sup>1,2\*</sup>

<sup>1</sup>School of Electrical and Automation Engineering  
Nanjing Normal University, Nanjing, 210046, China

<sup>2</sup>School of Electronic Science and Engineering  
Jilin University, Changchun 130012, China  
lirui202069@163.com

\*Corresponding Author

**Abstract** – In this paper, a compact integrated circular polarization filtering antenna is proposed based on substrate integrated waveguide (SIW) cavity. Firstly, a dual-mode (TE<sub>102</sub> and TE<sub>201</sub> modes) rectangular cavity is utilized as a common feeding cavity to achieve a dual-mode filtering response. And then, an additional rectangular patch with a slot is coupled from the feeding cavity for circular polarization radiation. To verify the proposed concept, a prototype circular polarization filtering antenna is simulated. The circular polarized filtering antenna resonates at 4.225 GHz with a low cross-polarization and a high gain of 7.23 dBi.

**Index Terms** – Circular polarization (CP), filtering antenna, patch antenna, substrate integrated waveguide (SIW).

## I. INTRODUCTION

With the rapid development of wireless communication systems, the integration and miniaturization of RF front-end have attracted more and more attention. Filter and antenna, as two important components of the RF front-end, are often employed in cascaded form. However, the form not only generates harmonics but also causes the system to be bulky. Thus, it is significant to integrate filter [1] and antenna [2] into a single component with dual functions. A filtering antenna [3] combines an antenna and a filter. It can provide the conversion between electrical power and radio waves, as well as the shaping of a filter-like response to antenna gain and input return loss. The integration of antennas and filters has been proven to be an effective method to reduce the cost and function block size of microwave systems.

Some filtering antennas are designed using different transmission structures in [4–5]. In previous designs, their gain responses cannot be achieved well. In recent years, because the substrate integrated waveguide (SIW) structure can achieve the interconnection of passive and

active devices. Therefore, it reduces the volume of the millimeter wave system and the cost. In addition, SIW have the merits of low insertion loss, high quality factor, and high-power capacity. Because of these advantages, the combination of SIW and filtering antenna is also attracting more and more attention.

Circularly polarized (CP) antennas have been widely investigated in recent years due to their advantages of suppressing interference and reducing polarization mismatch [6–7]. Only a few reports of CP filtering antennas have much room for improvement in bandwidth and miniaturization. In [8], by seamlessly integrating a high-Q SIW filter with a CP patch antenna, a planar CP filtering antenna is achieved. But the axial ratio (AR) bandwidth for the single antenna element is narrow, and a complicated rotated feeding network and an array are required to enhance the bandwidth. In [9], a novel single-fed low-profile CP antenna with a bandpass filtering response and a wider AR bandwidth is proposed. Although filtering response and wider AR bandwidth are achieved, the size of the presented antenna is still bulky. In addition, there are two perturbation modes on either side of the passband that affect the performance of the antenna.

In this paper, a CP filtering antenna is proposed with a compact double-layer SIW structure. By exploiting the electric field distributions from a feeding cavity with two orthogonal modes and a coupled symmetry radiation patch, good AR bandwidth and low cross-polarization are well attained. The operating principles and design method will be extensively illustrated as follows.

## II. DESIGN OF CIRCULAR POLARIZATION FILTERING ANTENNA

### A. Circular polarization filtering antenna configuration

Figure 1 (a) shows the construction of the proposed circular filtering antenna. In the bottom layer, a rectangular cavity with a pair of orthogonal modes based

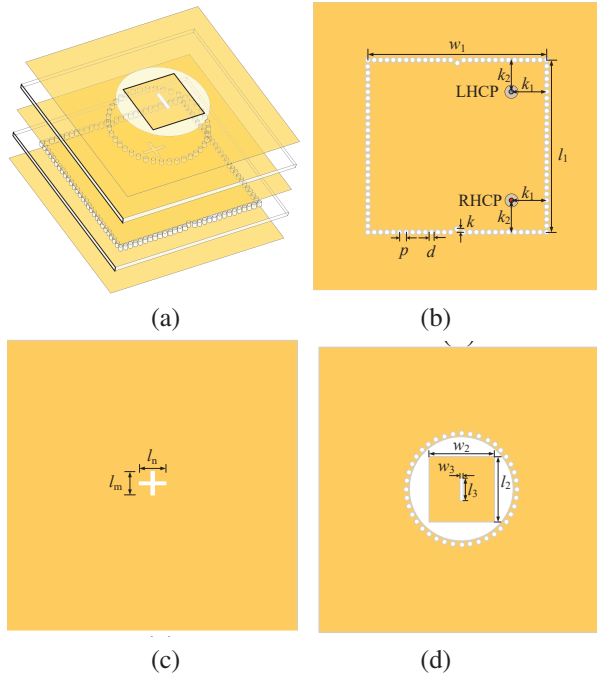


Fig. 1. The structure of the proposed filtering antenna: (a) 3D-view, (b) bottom-layer view, (c) middle-layer view, and (d) top-layer view.

on SIW is illustrated in Fig. 1 (b). And two metal via holes are placed in a particular position to control frequency. In Fig. 1 (c), two coupling apertures of the middle layer are used to transfer energy. As shown in Fig. 1 (d), a square patch with a slot is used to radiate circularly polarized beams. It is worth noting that the proposed design scheme can achieve a reverse circularly polarized beam by changing only the feed position without changing other parameters. The locations of the feed ports to achieve left- and right-handed CP are presented in Fig. 1 (b).

**B. Operating principles**

In order to explain the operating principles of the proposed circular polarization filtering antenna, a cou-

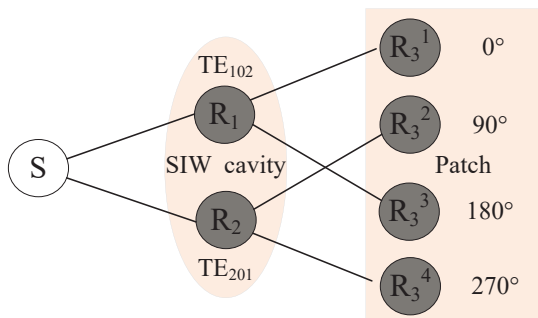


Fig. 2. Coupling topology.

pling topology corresponding to the configuration is described, as shown in Fig. 2.  $R_1$  and  $R_2$  represent TE<sub>102</sub> mode and TE<sub>201</sub> mode, respectively.  $R_1$ ,  $R_2$ ,  $R_3$ ,  $R_3$ , and  $R_4$  represent TM<sub>01</sub>, TM<sub>10</sub>, TM<sub>01</sub>, and TM<sub>10</sub> mode, respectively. A progressive phase difference of 90° in sequence among the four radiation modes is obtained. Circles represent resonant modes and input sources/ radiating load, and lines represent coupling between them. In addition, in Fig. 3, the two orthogonal modes of TE<sub>102</sub> mode and TE<sub>201</sub> mode would be coupled electrically with each other, which exhibits a phase difference of 90°. To further explain the CP radiation, the vector electric field distribution of the proposed right-handed CP antenna is presented in Figs. 4 and 5 for different phase stages. As shown in Fig. 4, the electric field inside the SIW cavity rotates counterclockwise within one period.

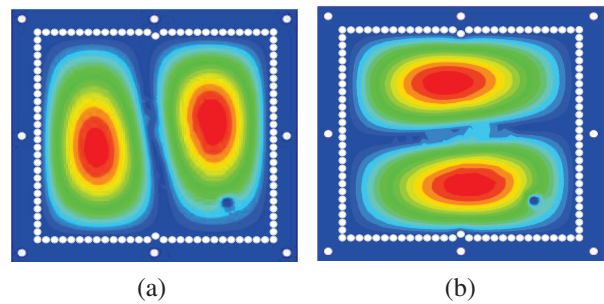


Fig. 3. E-field distributions of the bottom square cavity: (a) TE<sub>102</sub> mode and (b) TE<sub>201</sub> mode.

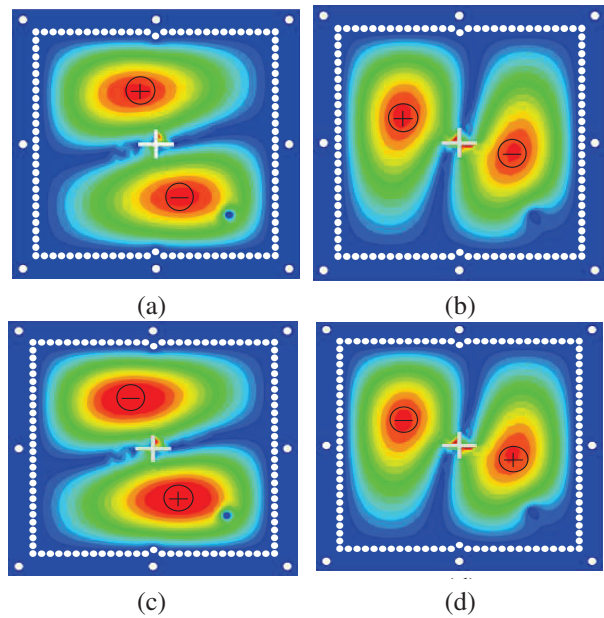


Fig. 4. Electric field distributions within one period for middle metal layer: (a)  $t = 0$ , (b)  $t = T/4$ , (c)  $t = T/2$ , and (d)  $t = 3T/4$ .

Similarly, within one period,  $TM_{01}$  mode and  $TM_{10}$  mode of the patch can be transformed into each other and rotated counterclockwise, as shown in Fig. 5. Therefore, the proposed antenna structure can radiate right-handed CP beams. In addition, a rectangular slot is introduced at

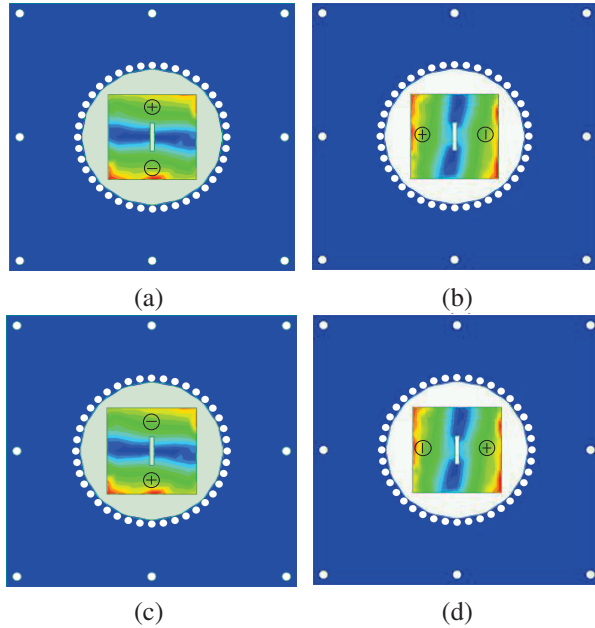


Fig. 5. Electric field distributions within one period for top metal layer: (a)  $t = 0$ , (b)  $t = T/4$ , (c)  $t = T/2$ , and (d)  $t = 3T/4$ .

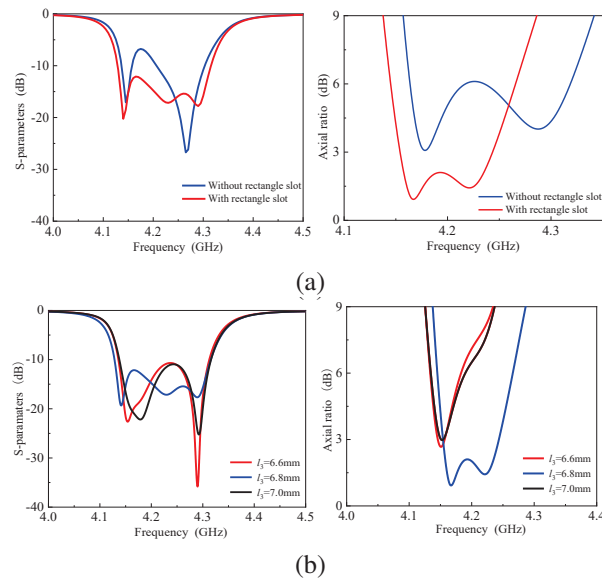


Fig. 6. Simulated reflection coefficient (left) and AR (right) for the proposed CP filtering antenna for different conditions: (a) with and without rectangle slot and (b) by varying  $l_3$ .

the center of the patch to optimize the impedance matching and AR bandwidth. Simulated reflection coefficient and AR of the proposed circulation polarization filtering antenna with different conditions are shown in Fig. 6. By removing the slot of the patch and fine-tuning the antenna size, it is found that the simulated impedance matching and AR become worse, as shown in Fig. 6 (a). And the effects of the length of the slot etched into the patch on the antenna reflection coefficient and axial ratio are studied in Fig. 6 (b). It can be found that the length of the slot has a slight influence on the reflection coefficient of the antenna and can obviously improve the AR of the antenna.

### III. IMPLEMENTATION AND RESULTS

For experimental validation, a compact right-handed CP filtering antenna is designed, prototyped, and tested. The photograph of the prototype is shown in Fig. 7. The CP filtering antennas are designed on Rogers Duroid 5880 substrate with the relative dielectric constant of 2.2 and loss tangent of 0.001, and the thickness  $h = 1.58$

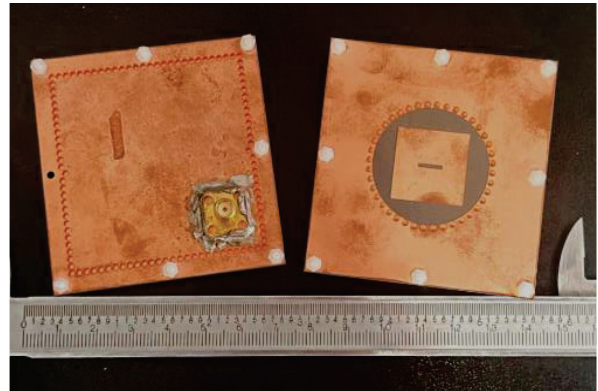


Fig. 7. The photograph of the fabricated prototype.

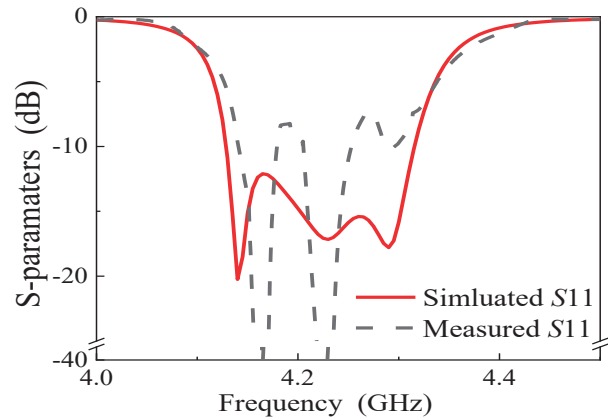


Fig. 8. Simulated and measured results for the proposed right-handed CP filtering antenna.

mm. The dimensions of the proposed filtering antenna are eventually determined as follows:  $w_1 = 56$  mm,  $l_1 = 54$  mm,  $p = 2$  mm,  $d = 1.6$  mm,  $k = 1$  mm,  $k_1 = 11$  mm,

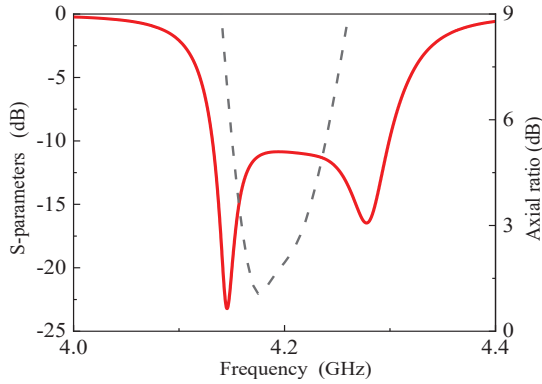


Fig. 9. The reflection coefficient and AR of the proposed left-handed CP filtering antenna.

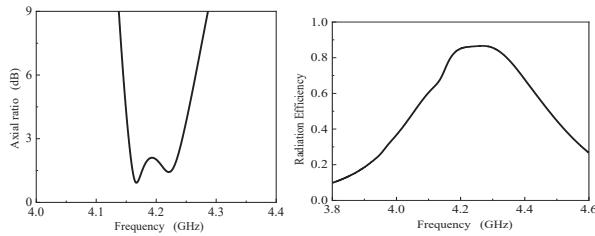


Fig. 10. The AR (left) and the radiation efficiency (right) of the proposed right-handed CP filtering antenna.

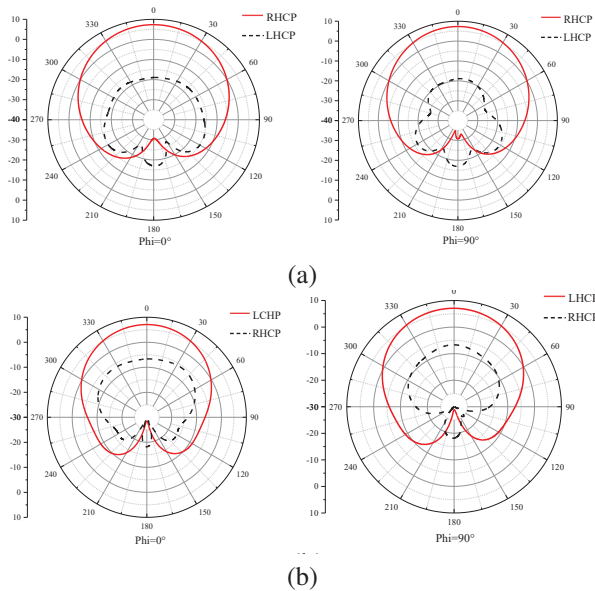


Fig. 11. The radiation patterns for the proposed CP filtering antenna: (a) Right-handed CP filtering antenna and (b) left-handed CP filtering antenna.

$k_2 = 10$  mm,  $l_n = 8.4$  mm,  $l_m = 7.2$  mm,  $l_2 = 20.6$  mm,  $w_2 = 20.6$  mm,  $w_3 = 1$  mm,  $l_3 = 6.8$  mm.

The measured reflection coefficients are presented in Fig. 8. The 10-dB fractional bandwidth is 4.5%. Figure 10 shows that the fractional AR bandwidth of the right-handed CP filtering antenna is 2.2% and the radiation efficiency is better than 86%. In order to validate the feasibility of the proposed design method, the left-handed CP filtering antenna is designed by only changing the feed position of the antenna without changing other parameters. The simulated reflection coefficients and the AR are presented in Fig. 9. It is obvious that it has 4.1% fractional bandwidth and 1.5% AR bandwidth.

Figure 11 shows the radiation patterns of the proposed right- and left-handed CP filtering antenna at 4.225 GHz. As observed, the cross-polarizations are better than 23 dB at 4.225 GHz for the right-handed circular polarization filtering antenna. The gain is better than 7.34 dBi in the right-handed circularization filtering antenna and is better than 7.1 dBi in the left-handed CP filtering antenna. The radiation patterns show that the proposed circular polarization filtering antenna has good polarization purity for right- and left-handed CP filtering antennas. The developed antenna is compared with the previously reported antenna in Table 1. The proposed filtering antenna performs to advantage in terms of relatively wider AR bandwidth and competitive gain as well as compact size.

Table 1: Comparison with related antennas

Reference	Filtering Response	AR (%)	Gain (dBi)	Size ( $\lambda_0^2$ )
[10]	No	1.1	5.0	1.96*1.01
[11]	No	1.0	9.2	1.33*1.33
[12]	Yes	8.8	5.8	1.07*1.07
[13]	Yes	4.9	5.1	0.89*0.89
[8]	Yes	1.3	6.8	0.56*0.44
[9]	Yes	3.9	8.0	1.01*1.01
Our work	Yes	2.2	7.4	0.84*0.92

## IV. CONCLUSION

In this paper, a compact integrated CP filtering antenna is proposed with good filtering and polarization purity based on a dual-mode SIW cavity. It is believed that the proposed design with these advantages will have the opportunity to be used in future wireless communication systems.

## ACKNOWLEDGMENT

This work was supported in part by the Postgraduate Research and Practice Innovation Program of Jiangsu Province under Grant KYCX23\_1763. (Corresponding author: Rui Li)

## REFERENCES

- [1] G. Zhang, Y. Liu, E. Wang, and J. Yang, "Multilayer packaging siw three-way filtering power divider with adjustable power division," *IEEE Trans. Circuits and Syst. II, Exp. Briefs*, vol. 67, no. 12, pp. 3003-3007, Dec. 2020.
- [2] L. Zhu and N. Liu, "Multimode resonator technique in antennas: A review," *Electromagnetic Science*, vol. 1, no.1, pp. 1-17, Mar. 2023.
- [3] H. Chu, C. Jin, J. Chen, and Y. Guo, "A 3-D millimeter-wave filtering antenna with high selectivity and low cross-polarization," *IEEE Trans. Antennas Propagat.*, vol. 63, no. 5, pp. 2375-2380, May 2015.
- [4] A. Abbaspour-Tamijani, J. Rizk, and G. Rebeiz, "Integration of filters and microstrip antennas," *IEEE Int. Antennas Propag. Symp. Dig.*, vol. 2, pp. 874-877, June 2002.
- [5] W. Wu, Y. Yin, S. Zuo, Z. Zhang, and J. Xie, "A new compact filter-antenna for modern wireless communication systems," *IEEE Antennas Wireless Propag. Lett.*, vol. 10, pp. 1131-1134, 2011.
- [6] S. A. Razavi and M. H. Neshati, "A low profile, broadband linearly and circularly polarized cavity backed antenna using halved-dual mode SIW cavity," *Applied Computational Electromagnetics Society (ACES) Journal*, vol. 31, no. 8, pp. 953-959, Aug. 2016.
- [7] F. Azamian, M. Naghi Azarmanesh, and C. Ghobadi, "A novel compact CPW-fed antenna with circular polarization characteristics for UWB applications," *Applied Computational Electromagnetics Society (ACES) Journal*, vol. 30, no. 1, pp. 93-98, Jan. 2015.
- [8] T. Li and X. Gong, "Vertical integration of high-Q filter with circularly polarized patch antenna with enhanced impedance-axial ratio bandwidth," *IEEE Trans. Microw. Theory Techn.*, vol. 66, no. 6, pp. 3119-3128, June 2018.
- [9] S. Ji, Y. Dong, Y. Pan, Y. Zhu, and Y. Fan, "Planar circularly polarized antenna with bandpass filtering response based on dual-mode SIW cavity," *IEEE Trans. Antennas Propagat.*, vol. 69, no. 6, pp. 3119-3128, June 2021.
- [10] Q. Wu, J. Yin, C. Yu, H. Wang, and W. Hong, "Low-profile millimeter wave SIW cavity-backed dual-band circularly polarized antenna," *IEEE Trans. Antennas Propagat.*, vol. 65, no. 12, pp. 7310-7315, Dec. 2017.
- [11] Z. C. Hao, X. M. Liu, X. P. Huo, and K. K. Fan, "Planar high-gain circularly polarized element antenna for array applications," *IEEE Trans. Antennas Propagat.*, vol. 63, no. 5, pp. 1937-1948, May 2015.
- [12] Q. S. Wu, X. Zhang, and L. Zhu, "Co-design of a wideband circularly polarized filtering patch antenna with three minima in axial ratio response," *IEEE Trans. Antennas Propagat.*, vol. 66, no. 10, pp. 5022-5030, Oct. 2018.
- [13] Y. T. Liu, K. W. Leung, J. Ren, and Y. X. Sun, "Linearly and circularly polarized filtering dielectric resonator antennas," *IEEE Trans. Antennas Propagat.*, vol. 67, no. 6, pp. 3629-3640, June 2019.



and antennas.



and antennas.



include microwave/millimeter-wave circuits and antennas.



circuits and antennas.

**Qiyue Gao** was born in Jiangsu, China, in 2003. She is currently pursuing the B.E. degree in electrical engineering and automation at Nanjing Normal University (NNU), Nanjing, China. Her current research interests include multifunctional microwave passive circuits

**Yuyao Zhu** was born in Jiangsu, China, in 2004. She is currently pursuing the B.E. degree in electrical engineering and automation at Nanjing Normal University (NNU), Nanjing, China. Her current research interests include multifunctional microwave passive circuits

**Xinyu Yang** was born in Anhui, China, in 1997. She received the B.E. degree from the Shanghai Maritime University (SMU), Shanghai, China, in 2019. She is currently pursuing the M.E. degree at Nanjing Normal University, Nanjing, China. Her current research interests

**Rui Li** was born in Jiangsu, China, in 1996. He received the M.E. degree from the Nanjing Normal University (NNU), Nanjing, China, in 2023. He is currently pursuing the Ph.D. degree at Jilin University, Jilin, China. His current research interests include microwave/millimeter-wave

# Compact Series-fed Circularly-polarized Patch Array based on Microstrip Line

Gengming Wei<sup>1,2</sup>, Le Chang<sup>3</sup>, and Yu Wu<sup>4</sup>

<sup>1</sup>School of Electronic Engineering  
Xidian University, Xi'an, 710071, China  
wud9032@163.com

<sup>2</sup>Global Big Data Technologies Centre  
University of Technology Sydney, Ultimo, NSW 2007, Australia  
wud9032@163.com

<sup>3</sup>Shaanxi Key Laboratory of Deep Space Exploration Intelligent Information Technology  
School of Information and Communications Engineering, Xi'an Jiaotong University, Xi'an, 710071, China  
changle4015@126.com

<sup>4</sup>Apple R&D  
Beijing, 100022, China  
q2770c@126.com

**Abstract** – A compact single-layer circularly polarized (CP) antenna array is proposed in this paper for 5G/6G applications. The conventional microstrip line is modified as a feeding network by periodically and alternatively loading field blocking stubs, producing a linearly polarized in-phase radiative field aperture. By adding CP corner-truncated patches beside these in-phase fields, a linear high-gain CP antenna array excited by a single feed is obtained. The feasibility of the proposed design is demonstrated through the fabrication and measurement of a 16-element linear array. The results indicate that the 3 dB axial ratio bandwidth is 3.5% (19.60~20.30 GHz), the -10 dB impedance bandwidth totally covers the 3 dB axial ratio bandwidth, and the peak realized gain is 14.9 dBi under an antenna length of  $5.69\lambda_0$ . This proposed strategy provides a very compact antenna structure to achieve high-gain CP radiation without the requirement of impedance transformers, phase shifters, and open-stop-band suppressing measures. Moreover, the antenna has a per-unit-length CP gain of  $5.5/\lambda_0$ , which is superior to many single-layer high-gain CP antennas.

**Index Terms** – Circularly-polarized antenna, microstrip line, microstrip patch antenna, series-fed antenna array.

## I. INTRODUCTION

Circularly-polarized (CP) planar antenna arrays are widely used in 5G/6G mobile communications and sensing systems due to their advantages of low profile,

reduced polarization mismatch, and improved robustness to environmental interference [1–3]. There are two primary types of feeding approaches: parallel and series feed. Parallel-fed arrays often require a large area to accommodate multiple power dividers/combiners, resulting in a large circuit area and associated loss [1–5]. The design becomes more complex when sequential rotation method is implemented to improve axial ratio bandwidth due to the newly introduced phase shifters [5–9]. Series-fed arrays are usually constructed by cascading the basic radiators along one dimension. They possess a more compact and simple design and have lower feed loss compared to parallel-fed arrays [3]. There exist two types of series-fed arrays, including standing-wave and traveling-wave arrays. The difference lies in whether the main line connecting these radiators is with a standing or traveling wave [3]. This simple and compact design strategy makes series-fed arrays a good choice for communication and sensing applications that require high-gain planar antennas [2].

Several transmission lines, such as waveguides, substrate-integrated waveguides, strip lines, and microstrip lines, can be used to construct series-fed CP arrays [1–4]. Waveguide-based arrays are known for their low loss and high-power capacity, but they have bulky volume [10]. Substrate-integrated waveguide arrays are a widely used solution due to their simple fabrication process of printed circuit board technology [11–19]. Microstrip lines are more preferred when designing single-layer CP antenna arrays. They

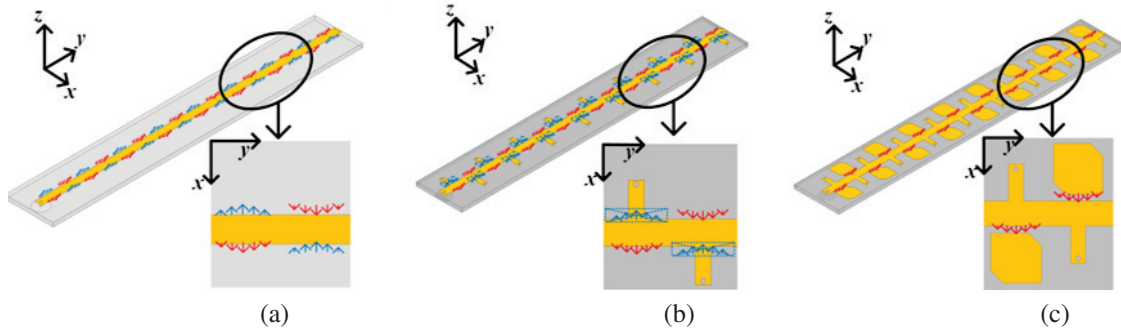


Fig. 1. Radiation principle to produce CP radiation. Field distributions of (a) a microstrip line with a shorted end, (b) an end-shortened microstrip line with blocking stubs, and (c) the proposed antenna.

have a simple structure and are easy to integrate with microwave components and circuits [20–26].

A compact high-gain CP array faces some challenges, such as complicated design and extra power loss. The former is reflected in newly introduced impedance transformers, phase shifters, and open-stop-band (OSB) suppressing measures. The most common series-fed patch array needs to calculate and tune impedance transformers individually from the last element to the first, so multiple impedance transformers are indispensable [25]. Sometimes, phase shifters are required to guarantee all the array elements with identical excitation phase in order to produce a broadside beam [24, 25]. When a leaky-wave antenna is adopted, the OSB effect needs to be eliminated for broadside radiation, which can be realized by two main measures. One is designing reflection-canceling unit cells [11, 13, 21, 27]. Another measure is to introduce axial-asymmetrical transmission lines [28]. At the end of the leaky-wave antenna, a terminal load is added to absorb the residual power to maintain the traveling wave property [11, 13, 20, 21, 27, 28]. It will introduce extra loss, especially when the leaky-wave antenna scale is small.

In this paper, a single-layer CP patch array is presented that utilizes a specially-designed feeding network. The network is constructed by alternately and periodically loading blocking stubs on a microstrip line, which can excite a series of corner-truncated CP patches. The proposed strategy is verified through the fabrication and measurement of a 16-element CP patch array. This innovative design has several advantages: 1) It provides a compact high-gain CP antenna strategy that eliminates the need for impedance transformers, phase shifters, and OSB suppressing measures. 2) The proposed antenna achieves a relatively high per-unit-length CP gain compared to other reported single-layer high-gain CP antennas. 3) Compared to leaky-wave antennas, the proposed antenna is with reduced dissipated power loss, particularly when the array size is limited.

## II. ANTENNA DESIGN

### A. Radiation principle

Figure 1 (a) shows the field distribution of a microstrip line with a shorted end. It is known that an electromagnetic wave is confined and propagates within the microstrip line due to the symmetric and periodic fields along the line. The introduction of blocking stubs on the fields with the same orientation can suppress the fringing fields on one side, generating a microstrip line with fringing fields pointing in the same direction, as depicted in Fig. 1 (b), where the fields pointing to the +X direction denoted by the red arrow lines are produced, and the ones along the -X denoted by blue are suppressed. The length of the blocking stubs should be selected to be approximately a quarter wavelength to transform the shorted end generated by the metallic via to the open end at the interconnection point. In this way, the transmission mode of the microstrip line could be maintained. This concept has been applied to construct a linearly polarized aperture previously in [29]. Here, it is employed as a feeding network to generate a CP antenna array.

Figure 1 (c) depicts the field distribution of the proposed antenna. The high-gain CP beam is obtained by utilizing the compact feeding network to capacitively couple power to the CP patches along the microstrip line. The CP patch is created by modifying a rectangular patch with diagonal perturbations. Figure 2 shows current distributions on an arbitrarily chosen patch at 20 GHz under different phases. The current rotates in an anticlockwise direction, which follows the right-handed rule. So, right-hand circular polarization (RHCP) broadside radiation is achieved.

### B. Scalability

Figure 3 depicts the broadside directivities at 20 GHz as a function of element numbers. The directivity increases as the element increases, and the directivity increase trend follows a logarithmic distribution.

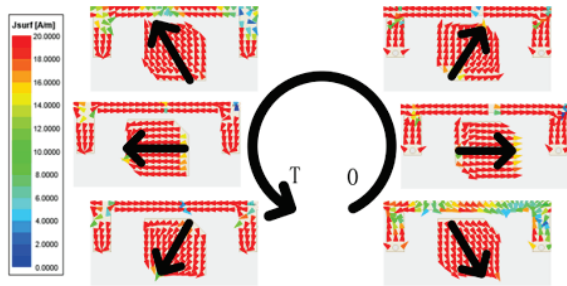


Fig. 2. Current distributions on an arbitrarily chosen patch at 20 GHz under different phases.

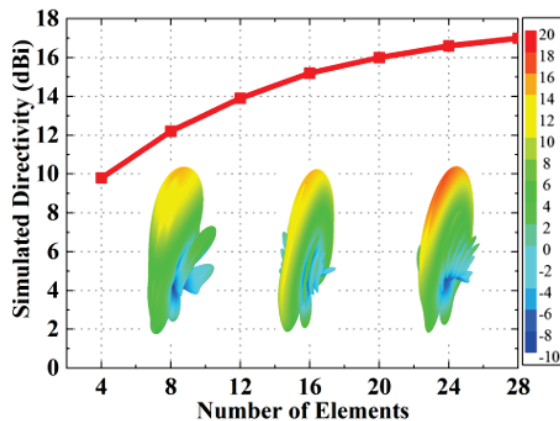


Fig. 3. Simulated broadside directivities at 20 GHz with different element numbers.

Elements numbering 16 is a nice compromise between array size and directivity. Further increasing the elements contributes little to directivity improvement.

### C. Antenna geometry

The geometry of the proposed antenna is presented in Fig. 4. It is a single-layer structure based on a 1.016 mm-thick TLX-8 substrate ( $\epsilon_r = 2.55$ ,  $\tan\delta = 0.0019$ ). The proposed antenna consists of a compact feeding network and 16 CP radiating patches. The feeding network is a blocking-stubs-loaded microstrip line with its rear end shorted. The microstrip line has width  $w_l = 2$  mm, and its shorted end is realized by using two vias with diameter 0.4 mm and spacing 1 mm. The blocking stubs are shorted rectangular metal slices with length  $l_s = 2.6$  mm and width  $w_s = 1.2$  mm. Their shorted ends are realized by using shorted vias with diameter 0.4 mm. The patches are located at the openings of the feeding network with a gap of  $d_p = 0.4$  mm. The corner-truncated patch chamfered with length  $a_p = 0.9$  mm achieves the RHCP radiation. These patches are with the length, width, and spacing of  $l_p = 4.1$  mm,  $w_p = 4$  mm, and  $d_s = 5$  mm, respectively.

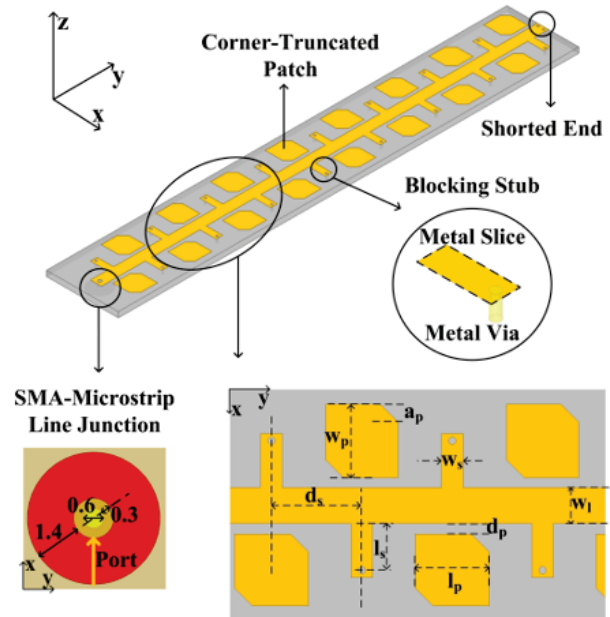


Fig. 4. Geometry of the proposed antenna. The parameters are  $w_l = 2$  mm,  $d_s = 5$  mm,  $w_p = 4$  mm,  $l_p = 4.1$  mm,  $w_s = 1.2$  mm,  $l_s = 2.6$  mm,  $d_p = 0.4$  mm,  $a_p = 0.9$  mm.

The input port locates at the bottom surface, as shown in the enlarged inset on the bottom-left corner of Fig. 4. The feeding probe is a metallic via hole with a diameter of 0.6 mm, which is situated at the center of a metal ring with a width of 0.3 mm. The circular ring with a width of 1.4 mm, marked by red, is where the lumped port is located.

## III. VALIDATION AND PERFORMANCE COMPARISON

### A. Fabrication and measurement

The proposed antenna is manufactured using standard printed circuit board technology. The fabricated prototype is depicted in Fig. 5. The S parameter of the developed array was measured using a Keysight N5244B PNA-X Microwave Network Analyzer. The radiation

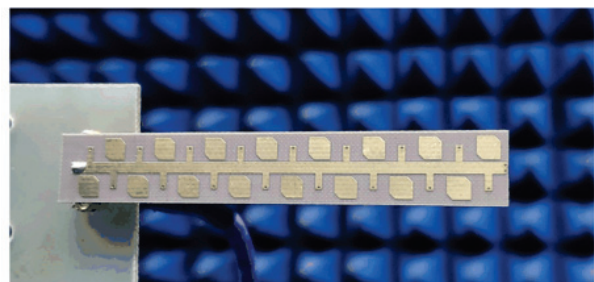


Fig. 5. Fabricated prototype.

pattern was measured with a NSI2000 antenna measurement system. The simulated and measured results are shown in Figs. 6 and 7. They agree very well. The simulated and measured reflection coefficients are depicted in Fig. 6. The measured -10 dB impedance bandwidth exceeds 4.4% (19.50~20.38 GHz), while the simulated exceeds 4.8% (19.50~20.45 GHz). Acceptable impedance bandwidth is obtained. Simulated and measured normalized radiation patterns at 20 GHz in two principal planes (XOZ and YOZ) are shown in Figs. 7 (a) and (b). A fan-shaped beam for co-polarization (RHCP) is observed. It is with a wide 2-D pattern in the XOZ plane, a narrow beam in the YOZ plane. The results exhibit excellent RHCP performance with good cross-polarization discrimination (XPD). In the broadside direction, the measured XPD is 30.7 dB, while the simulated exceeds 40.0 dB. In the upper space, the measured XPDs of both planes are superior to 9.5 dB, while the simulated are better than 8.0 dB. Figures 7 (c) and (d) show the axial ratio and realized

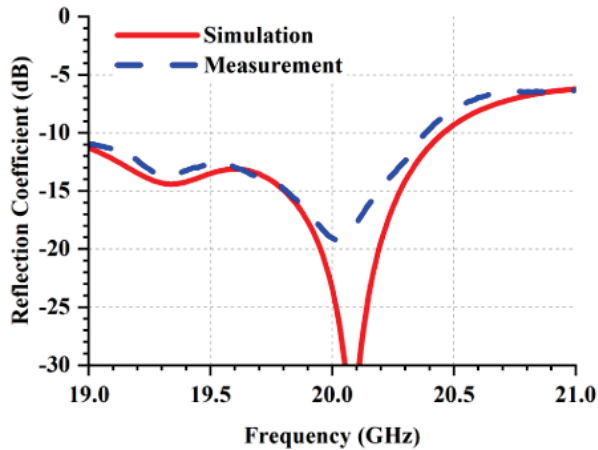


Fig. 6. Simulated and measured reflection coefficients.

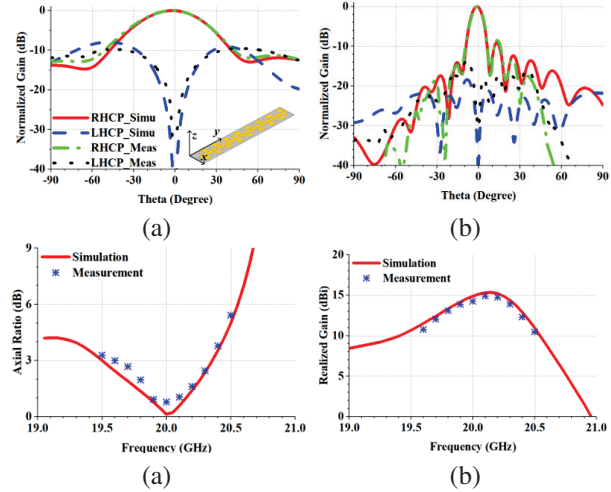


Fig. 7. Simulated and measured results of the (a) normalized radiation pattern in XOZ plane at 20 GHz, (b) normalized radiation pattern in YOZ plane at 20 GHz, (c) axial ratio, and (d) realized gain.

gain at broadside. The measured 3 dB axial ratio bandwidth is 3.5% (19.60~20.30 GHz), while the simulated is 4.3% (19.50~20.35 GHz). The measured peak gain is 14.9 dBi, while the simulated is 15.4 dBi, both appearing at 20.10 GHz.

## B. Performance comparison

The performance comparison between the proposed antenna and other recently reported single-layer series-fed CP arrays is presented in Table 1. As seen from the table, the proposed antenna exhibits two significant merits.

Firstly, the proposed antenna offers a compact design strategy for achieving a high-gain patch array. The existing strategies either need impedance transformers [13, 19, 24–26], phase shifters [24, 25], or extra OSB

Table 1: Performance comparison between the proposed antenna and other recently reported single-layer series-fed CP arrays

Refs.	Array Scale	Antenna Length ( $\lambda_0$ )	Freq. (GHz)	Peak Gain (dBi)	CP Gain Per Unit Length ( $/\lambda_0$ )	No Impedance Transformers?	No Phase Shifters?	No Need to Suppress OSB?
[11]	1 × 16	14.41	17.00	17.0	3.5	✓	✓	×
[13]	1 × 16	15.20	16.00	18.9	5.1	×	✓	×
[19]	1 × 4	4.10	6.65	10.3	2.6	×	✓	✓
[21]	1 × 12	5.83	7.82	12.5	3.1	✓	✓	✓
[24]	2 × 6	4.28	7.14	16.3	10.0	×	×	✓
[25]	1 × 4	2.25	2.37	10.0	4.4	×	×	✓
[26]	1 × 4	4.24	3.00	16.0	9.4	×	✓	✓
This Work	1 × 16	5.69	20.10	14.9	5.5	✓	✓	✓

suppressing designs [11, 13]. In contrast, the proposed antenna is so compact that all three factors are unnecessary.

Secondly, the proposed antenna exhibits a high per-unit-length gain (refers to the absolute gain value produced by unit length). It is with the per-unit-length realized gain of  $5.5/\lambda_0$ , which is higher than 5 of the 7 references [11, 13, 19, 21, 25].

In addition, the proposed antenna is a standing-wave antenna compared to leaky-wave antennas. It is with a shorted end rather than a terminal load, so the proposed strategy is especially beneficial to design a small-scale patch array [11, 13, 21]. In contrast, the small-scale leaky-wave antenna suffers from dissipated power absorbed by the terminal load.

#### IV. CONCLUSION

This paper proposes a compact strategy to produce a single-layer high-gain CP antenna array. By introducing blocking stubs periodically and alternatively on a one-end-shortened microstrip line, a design-friendly feeding network is obtained. By adding CP corner-truncated patches beside these in-phase fields, a linear high-gain CP antenna array excited by a single feed is obtained. A fabricated prototype has demonstrated its feasibility. The design is so simple because it eliminates the requirement of impedance transformers, phase shifters, and additional OSB suppressing measures.

#### REFERENCES

- [1] Y. T. Lo and S. W. Lee, *Antenna Handbook*. New York: Van Nostrand Reinhold, pp. 21-23, 1993.
- [2] S. Gao, Q. Luo, and F. Zhu, *Circularly Polarized Antennas*. John Wiley & Sons, pp. 191-258, 2014.
- [3] J. R. James and P. S. Hall, *Handbook of Microstrip Antennas (IEE Electromagnetic Waves Series; 28)*, London, U.K.: P. Peregrinus on behalf of the Institution of Electrical Engineers, pp. 219-272, 1989.
- [4] D. M. Pozar, *Microwave Engineering*, 4th ed., Hoboken, NJ: Wiley, pp. 95-158, 2012.
- [5] J. Huang, "A technique for an array to generate circular polarization with linearly polarized elements," *IEEE Trans. Antennas Propag.*, vol. 34, no. 9, pp. 1113-1124, Sep. 1986.
- [6] Y. Li, Z. Zhang, and Z. Feng, "A sequential-phase feed using a circularly polarized shorted loop structure," *IEEE Trans. Antennas Propag.*, vol. 61, no. 3, pp. 1443-1447, Mar. 2013.
- [7] C. Deng, Y. Li, Z. Zhang, and Z. Feng, "A wideband sequential-phase fed circularly polarized patch array," *IEEE Trans. Antennas Propag.*, vol. 62, no. 7, pp. 3890-3893, July 2014.
- [8] S. X. Ta and I. Park, "Compact wideband circularly polarized patch antenna array using metasurface," *IEEE Antennas Wireless Propag. Lett.*, vol. 16, pp. 1932-1936, Mar. 2017.
- [9] A. R. Weily and Y. J. Guo, "Circularly polarized ellipse-loaded circular slot array for millimeter-wave WPAN applications," *IEEE Trans. Antennas Propag.*, vol. 57, no. 10, pp. 2862-2870, Oct. 2009.
- [10] G. Montisci, "Design of circularly polarized waveguide slot linear arrays," *IEEE Trans. Antennas Propag.*, vol. 54, no. 10, pp. 3025-3029, Oct. 2006.
- [11] P. Sanchez-Olivares and J. L. Masa-Campos, "Novel four cross slot radiator with tuning vias for circularly polarized SIW linear array," *IEEE Trans. Antennas Propag.*, vol. 62, no. 4, pp. 2271-2275, Apr. 2014.
- [12] C. Zhijun, W. Hong, K. Zhenqi, C. Jixin, and K. Wu, "Circularly polarized slot array antenna based on substrate integrated waveguide," *2008 Int. Conf. on Microwave and Millimeter Wave Technology*, Apr. 2008.
- [13] P. Chen, W. Hong, Z. Kuai, and J. F. Xu, "A substrate integrated waveguide circular polarized slot radiator and its linear array," *IEEE Antennas Wireless Propag. Lett.*, vol. 8, pp. 120-123, Apr. 2009.
- [14] J. Zhu, S. Liao, Y. Yang, S. Li, and Q. Xue, "60 GHz dual-circularly polarized planar aperture antenna and array," *IEEE Trans. Antennas Propag.*, vol. 66, no. 2, pp. 1014-1019, Feb. 2018.
- [15] H. Zhou and W. Hong, "Compact circularly polarized patch array antenna," *IEEE Antennas Wireless Propag. Lett.*, vol. 15, pp. 778-781, Aug. 2016.
- [16] Y. Li, Z. N. Chen, X. Qing, Z. Zhang, J. Xu, and Z. Feng, "Axial ratio bandwidth enhancement of 60-GHz substrate integrated waveguide-fed circularly polarized LTCC antenna array," *IEEE Trans. Antennas Propag.*, vol. 60, no. 10, pp. 4619-4626, Oct. 2012.
- [17] J. Huang, W. Lin, F. Qiu, C. Jiang, D. Lei, and Y. J. Guo, "A low profile, ultra-lightweight, high efficient circularly-polarized antenna array for Ku band satellite applications," *IEEE Access*, vol. 5, pp. 18356-18365, Sep. 2017.
- [18] D. F. Guan, C. Ding, Z. P. Qian, Y. S. Zhang, Y. J. Guo, and K. Gong, "Broadband high-gain SIW cavity-backed circular-polarized array antenna," *IEEE Trans. Antennas Propag.*, vol. 64, no. 4, pp. 1493-1497, Apr. 2016.
- [19] Z. Hao, X. Liu, X. Huo, and K. Fan, "Planar high-gain circularly polarized element antenna for array applications," *IEEE Trans. Antennas Propag.*, vol. 63, no. 5, pp. 1937-1948, May 2015.

- [20] S. Ogurtsov and S. Koziel, "A conformal circularly polarized series-fed microstrip antenna array design," *IEEE Trans. Antennas Propag.*, vol. 68, no. 2, pp. 873-881, Feb. 2020.
- [21] T. R. Cameron, A. T. Sutinjo, and M. Okoniewski, "A circularly polarized broadside radiating "herringbone" array design with the leaky-wave approach," *IEEE Antennas Wireless Propag. Lett.*, vol. 9, pp. 826-829, Aug. 2010.
- [22] S. J. Chen, C. Fumeaux, Y. Monnai, and W. Withayachumnankul, "Dual circularly polarized series-fed microstrip patch array with coplanar proximity coupling," *IEEE Antennas Wireless Propag. Lett.*, vol. 16, pp. 1500-1503, Jan. 2017.
- [23] N. Nguyen-Trong, S. J. Chen, and C. Fumeaux, "High-gain dual-band dual-sense circularly polarized spiral series-fed patch antenna," *IEEE Open Journal of Antennas and Propagation*, vol. 3, pp. 343-352, Mar. 2022.
- [24] Q. Chen, Y. Wei, J. Zhang, and W. Wu, "Dual-band circularly polarized shared-aperture array with wideband and small frequency ratio," *2016 IEEE Int. Conf. on Ubiquitous Wireless Broadband*, pp. 1-3, Oct. 2016.
- [25] P. D. Hilario Re, D. Comite, and S. K. Podilchak, "Single-layer series-fed planar array with controlled aperture distribution for circularly polarized radiation," *IEEE Trans. Antennas Propag.*, vol. 68, no. 6, pp. 4973-4978, June 2020.
- [26] K. Hirose, K. Shinozaki, and H. Nakano, "A comb-line antenna modified for wideband circular polarization," *IEEE Antennas Wireless Propag. Lett.*, vol. 14, pp. 1113-1116, May 2015.
- [27] H. Lee, J. H. Choi, C.-T. M. Wu, and T. Itoh, "A compact single radiator CRLH-inspired circularly polarized leaky-wave antenna based on substrate-integrated waveguide," *IEEE Trans. Antennas Propag.*, vol. 63, no. 10, pp. 4566-4572, Oct. 2015.
- [28] S. Otto, Z. Chen, A. Al-Bassam, A. Rennings, K. Solbach, and C. Caloz, "Circular polarization of periodic leaky-wave antennas with axial asymmetry: theoretical proof and experimental demonstration," in *IEEE Trans. Antennas Propag.*, vol. 62, no. 4, pp. 1817-1829, Apr. 2014.
- [29] L. Chang, Z. Zhang, Y. Li, and M. F. Iskander, "Single-layer magnetic current antenna array with high realized aperture usage rate based on microstrip line structure," *IEEE Trans. Antennas Propag.*, vol. 65, no. 2, pp. 584-592, Dec. 2017.



**Gengming Wei** received the B.S. degree from Xidian University, Xi'an, China, in 2012. He is currently pursuing the collaborative Ph.D. degree between Xidian University and the University of Technology Sydney, Sydney, NSW, Australia. His research interests include UWB antennas, high-gain antennas with low profile, wireless power transfer systems, and antenna measurement systems.



**Le Chang** received the B.S. degree in electronics and information engineering from Xidian University, Xi'an, China, in 2012, and the Ph.D. degree in electrical engineering from Tsinghua University, Beijing, China, in 2017. In July 2017, he joined Huawei Technology Ltd., Beijing, China, as a senior antenna engineer. Since 2021, he has been with Xi'an Jiaotong University, where he is currently an associate professor. He has authored or co-authored over 34 journal articles. His current research interests include mobile antennas and mmW/THz antennas.



**Yu Wu** received the M.S. degree in electronics and information engineering from Xidian University, Xi'an, China, in 2016.

He is currently a senior engineer with Apple R&D, Beijing, China. His current research interests include mobile antennas, mobile device signal measurements in all kinds of scenarios.

# Low-profile Dual-polarized Filtering Antenna with Improved Gain and Impedance Bandwidth using Characteristic Mode Analysis

Zong-Zhuo Wang<sup>1</sup>, Neng-Wu Liu<sup>1\*</sup>, and Liang Fang<sup>2</sup>

<sup>1</sup>National Key Laboratory of Antennas and Microwave Technology  
Xidian University, Xi'an, 710071, China  
zzhwang@stu.xidian.edu.cn, \*yb47448@umac.mo

<sup>2</sup>Aviation Key Lab of Science and Technology on High Performance Electromagnetic Windows AVIC Research  
Institute for Special Structures of Aeronautical Composites, Ji'nan, Shandong, 250023, China  
fangl005@avic.com

**Abstract** – A low-profile dual-polarized filtering microstrip patch antenna (MPA) with improved gain and bandwidth is realized without requirement of filtering circuit. Herein, the characteristic mode analysis (CMA) method is adopted to analyze the antenna performances. Initially, the resonant modes of the MPA are deeply analyzed, which indicates that its resonant frequencies of CM1 and CM3 could be moved close to each other by loading slots and shorting pins, thus broadening the impedance bandwidth. Then, the influence of the slots on radiation patterns of the antenna is further studied. The results demonstrate that the non-broadside radiation beam of its CM1 could be reshaped as the broadside beam, and the sidelobe level of its CM3 could be reduced by cutting the slots, leading to the improved gain. After that, the effect of the pins on the gain-response is investigated, It shows that the gain nulls of the MPA could be controlled at both lower and upper bands, especially for the non-filtering scheme. Finally, the proposed dual-polarized antenna is fabricated and tested. The results prove that its impedance bandwidth reaches to about 7.4% with a low-profile of about 0.038 free-space wavelength. Besides, a stable enhanced gain of around 10 dBi is achieved over the operating band.

**Index Terms** – Characteristic mode analysis (CMA), filtering response, high-gain, low-profile, non-filtering scheme.

## I. INTRODUCTION

With the rapid development of wireless communication technology, communication systems tend to be miniaturized, integrated, and multifunctional. In order to reduce the interference between the antennas of different frequency bands in the communication system, and to meet the system miniaturization, it is more meaningful to integrate the filter with antenna design.

In recent years, more extensive research and design of filter antennas have been carried out. Firstly, one approach is to cascade the filter and the antenna, with the antenna radiator as the last stage of the filter [1–4]. This cascading method requires the separation of the feeding part and the antenna, which is not conducive to the miniaturization of the antenna. At the same time, due to the existence of the filter, the antenna still has transmission loss, which will deteriorate the radiation gain of the antenna. Secondly, incorporating or embedding filtering structures into the original antenna is a mainstream design approach. For example, the filtering performance is obtained by adopting novel feeding structures [5–10] and loading same-layer or stacked parasitic elements [11–17]. However, the above methods increase the complexity of the design and still have the problems of large size and high profile of the antenna. A more efficient method is to slot or load shorting pins in the antenna to obtain one or more radiation gain nulls [18–24]. This greatly simplifies the complexity of the antenna design while maintaining the characteristics of miniaturization and low profile. The dual-polarization design of the filtering antenna will improve the capability of the antenna, alleviate the polarization mismatch problem caused by the multipath effects, and improve the utilization rate of spectrum resources.

In this paper, a novel dual-polarized filtering antenna is proposed with no extra filtering circuit and high gain. While maintaining the low-profile characteristics, the filtering response is obtained by loading the shorting pins, and the frequency band is widened by the combination of the loading the shorting pins and slotting.

## II. GEOMETRY AND WORKING PRINCIPLE

The configuration of the proposed low-profile dual-polarized filtering microstrip patch antenna (MPA) with improved gain and impedance bandwidth is depicted in

Fig. 1. It shows that a radiating patch with the dimensions of  $L_1 \times L_1$  is printed on the top surface of a substrate ( $L \times L$ ), which has the thickness  $H_1 = 0.8$  mm, loss tangent of about 0.001, and dielectric constant  $\epsilon r_1 = 2.17$ .

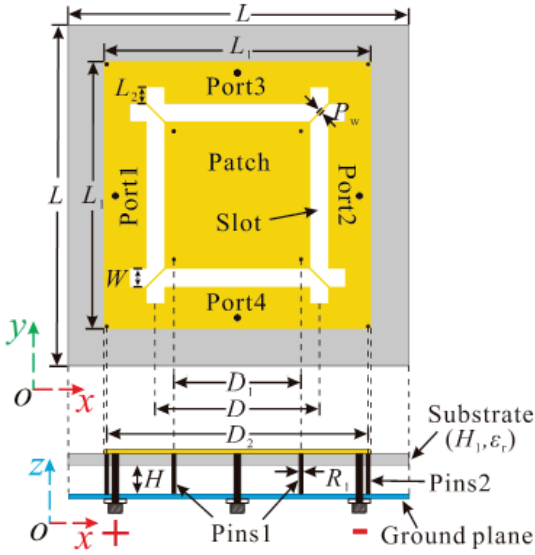


Fig. 1. Configuration of the proposed dual-polarized filtering MPA:  $L = 160$ ,  $L_1 = 120$ ,  $L_2 = 4$ ,  $W = 9$ ,  $H = 4$ ,  $H_1 = 0.8$ ,  $D = 78$ ,  $D_1 = 60$ ,  $D_2 = 118$ ,  $P_w = 0.4$ ,  $R_1 = 0.2$ . Unit: mm.

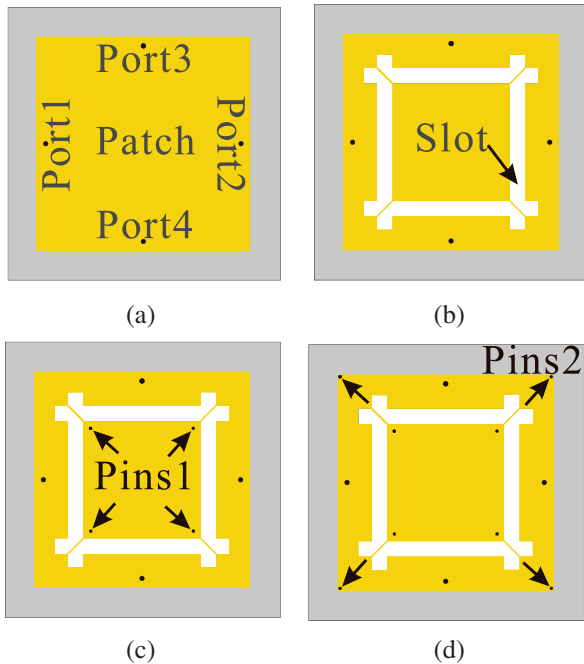


Fig. 2. Evolution process of our proposed MPA: (a) Antenna I, (b) antenna II, (c) antenna III, and (d) the proposed antenna.

Besides, the ground plane ( $L \times L$ ) is placed below the substrate with an air gap of  $H = 4$  mm. Figure 2 gives an evolution process of the MPA. By loading two pairs of bent slots with spacing  $D$ , the desired CM1 and CM3 could be shifted close to each other, and it also contributes to improve the radiation beams of these two modes. In addition, four shorting pins are loaded inside antenna II to generate the radiation gain null at the upper band, while four shorting pins are loaded on the edge of antenna III to generate the radiation gain null at the lower band. In the following, the proposed MPA is extensively analyzed with all the simulated results to be provided.

**A. Mode selection**

Initially, characteristic mode analysis (CMA) is used to select the desired modes of the traditional MPA for simultaneous gain and bandwidth enhancements. Note that the following analyses, conducted as port 1 and port 2, are excited differentially. Figure 3 plots the modal significance (MS) and modal weighting coefficient (MWC) of antenna I. As can be seen, there are four resonant modes (CM1, CM2, CM3, and CM4) in the wide frequency band. As such, the corresponding electric fields and radiation patterns of these four modes are illustrated in Figs. 4 and 5. It shows that only CM3 has the maxi-

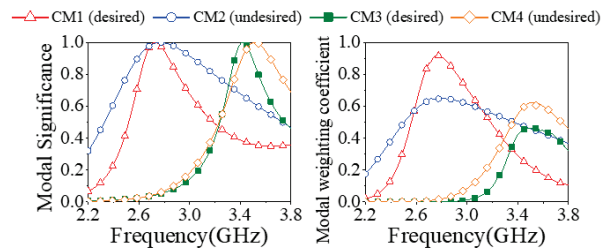


Fig. 3. Modal significance and modal weighting coefficient of the antenna I.

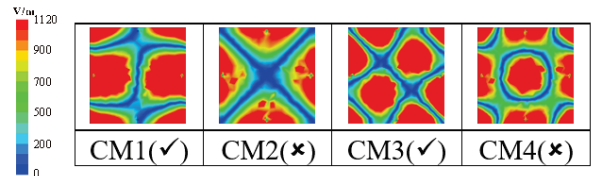


Fig. 4. Modal electric fields of the antenna I.

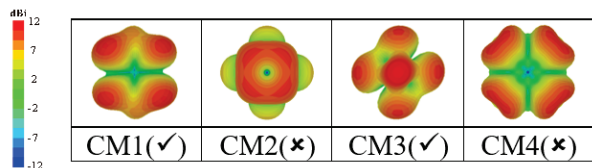


Fig. 5. Modal radiation patterns of the antenna I.

imum gain in the normal direction, while the other modes have radiation nulls in this direction. Most importantly, the maximum gains of its CM1, CM2, CM3, and CM4 reach to about 9.77 dBi, 8.87 dBi, 12.1 dBi, and 8.99 dBi, respectively. Hence, CM1 and CM3 are selected as the desired modes for the realization of wide-bandwidth and high-gain simultaneously.

### B. Gain improvement

The results Fig. 5 indicate that CM1 suffers from the non-broadside radiation beam, and the CM3 simultaneously has a high sidelobe level. Hence, in order to reshape radiated fields of these dual modes, a set of four slots are cut on the radiating patch as shown in Fig. 2 (b) or Fig. 6. Due to the symmetrical loaded slots, these four slots will cross each other when they reach a large length and therefore are bent.

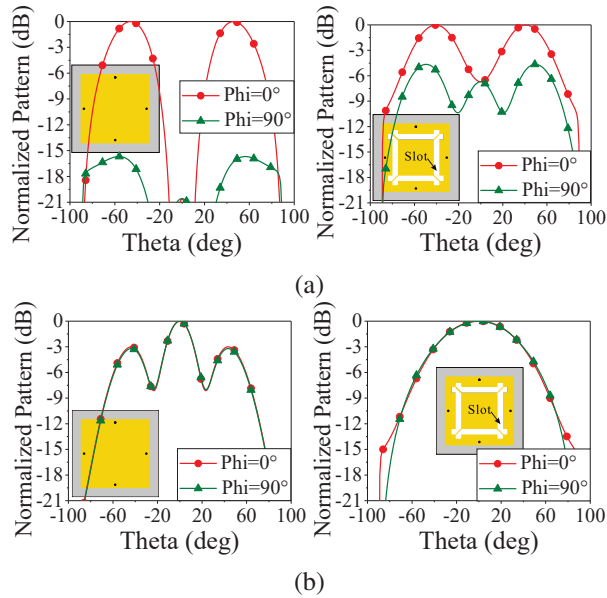


Fig. 6. Normalized patterns of the MPA with and without the slots: (a) CM1 and (b) CM3.

Besides, the normalized radiation patterns of the MPA with and without these slots are compared under these two modes (see Fig. 6). As can be seen in Fig. 6, the gain of the antenna in the broadside direction could be enhanced by loading these slots at CM1. This working principle has been proven from the previous works [25–26]. Meanwhile, the sidelobe level of its CM3 could be gradually reduced from 3.2 dB to 0 dB via these components.

### C. Filtering response generation

Apart from gain improvement, the antenna with filtering response is in high demand. As shown in Fig. 7, when four shorting pins are loaded around the diagonal position inside antenna II, the resonant frequency

of CM3 could be shifted up significantly to a high frequency band as compared to that of CM1. As such, the dual modes are successfully moved close to each other.

The peak realized gain curves of the antennas with and without the loaded pins are illustrated in Fig. 8, where it can be seen that a radiation gain null in the upper band is generated by loading the pins. To be extended, the electric current distributions of antenna II and antenna III are compared in Fig. 9. Compared with antenna II, the current inside the antenna III undergoes a reversal after loading the pins. At this point, along the  $x$ -axis or  $y$ -axis, the surface current flows symmetrically in the opposite direction, which results in the far-field radiation of the antenna to be cancelled out in the broadside direction, thus generating a radiation null in the upper band.

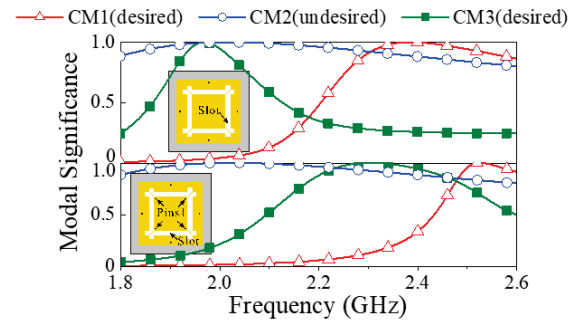


Fig. 7. Modal significance of the MPA with and without the loaded pins.

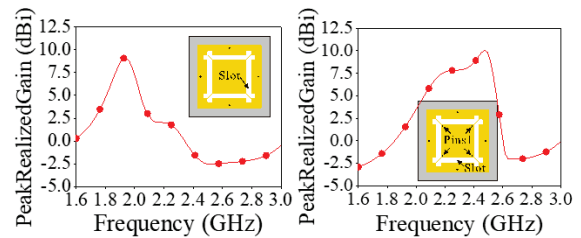


Fig. 8. Peak realized gain curves of the MPA with and without the loaded pins.

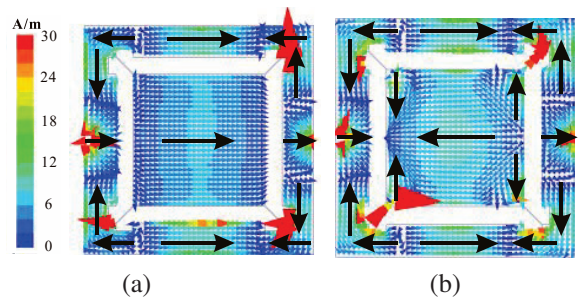


Fig. 9. Electric current distribution on the patch at 2.7 GHz for (a) antenna II and (b) antenna III.

After that, the effect of four shorting pins<sub>2</sub> on the resonant frequencies of antenna III is further studied. As can be seen from Fig. 10, the frequency spacing between two modes is further reduced. By comparing the peak realized gain curves before and after loading pins<sub>2</sub>, it can be found in Fig. 11 that a new radiation gain null in the lower band is generated.

Moreover, the electric current distributions of antenna III and the proposed antenna are compared in Fig. 12. It can be seen that there is almost no current distribution inside the two antennas, but the current at the edge of the proposed antenna has changed. At this point, the current at the edge of the antenna flows symmetrically and reversely along the  $y$ -axis, and the current along

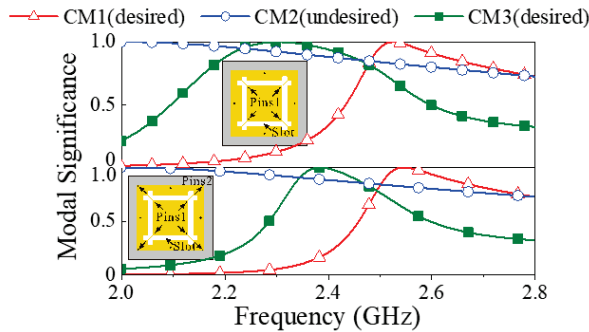


Fig. 10. Modal significance of the antenna with and without the loaded pins<sub>2</sub>.

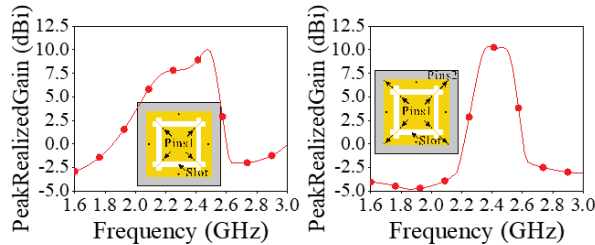


Fig. 11. Modal significance of the antenna with and without the loaded pins<sub>2</sub>.

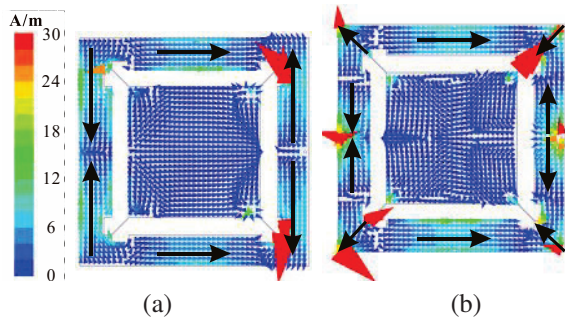


Fig. 12. Electric current distribution on the patch at 1.9 GHz for (a) antenna III and (b) proposed antenna.

the  $x$ -axis is offset by the current in the diagonal direction, which results in the far-field radiation of the antenna to cancel out in the broadside direction, thus generating a radiation gain null in the lower band.

### III. RESULTS AND EXPERIMENTAL VALIDATION

To validate the performance mentioned above, the proposed antenna is fabricated and measured, with the prototype shown in Fig. 13. Initially, the  $|S_{dd11}|$  of our proposed antenna is measured by using the R&S ZNB20 Vector Network Analyzer, and the relevant simulated and measured results are presented in Fig. 14. As can be seen, the measured S-parameter is matched well with the simulated S-parameter under the two polarization operations. The impedance bandwidth of the proposed antenna for  $|S_{dd11}| < -10$  dB is 7.4% ranging from 2.34 to 2.52 GHz.

After that, the radiation patterns, peak realized gains, and radiation efficiencies of the proposed antenna are measured by employing a near-field SATIMO antenna test system. As shown in Fig. 15, the measured radiation patterns are in good agreement with the simulated radiation patterns at 2.37 and 2.49 GHz, and the cross-polarization is lower than -20 dB.

In addition, the simulated and measured peak realized gains and radiation efficiencies of the proposed antenna are presented in Fig. 16. As can be seen, the

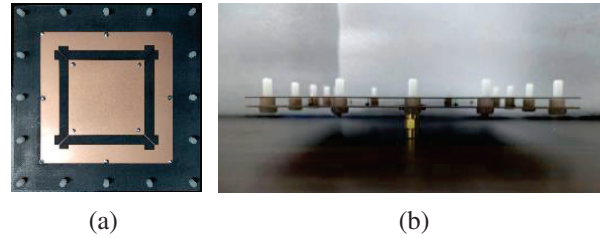


Fig. 13. Photograph of the fabricated MPA: (a) Top view and (b) side view.

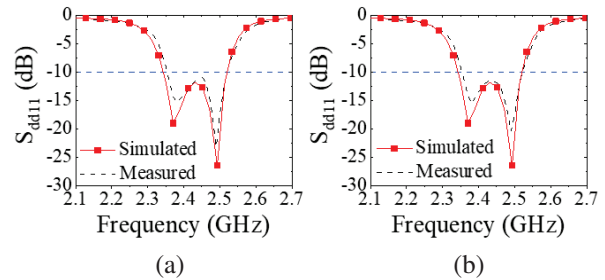


Fig. 14. Simulated and measured S-parameter of the proposed antenna: (a) Port 1 and port 2 are differentially excited and (b) port 3 and port 4 are differentially excited.

Table 1: Performance comparison with the previous filtering antennas

Ref.	Polarization	Filtering Method	Radiator Volume	Gain (dBi)	Extra Filtering Circuit	Easy for Integration
[10]	single	Filtering circuit	$0.056\lambda_0^3 \uparrow$	8.7 $\downarrow$	Yes	No
[11]	single	Stacked patch + Slots	$0.13\lambda_0^3 \uparrow$	7.2 $\downarrow$	No	No
[5], [7]	dual	Filtering circuit	$\geq 0.145\lambda_0^3 \uparrow$	$\approx 8\text{dBi} \downarrow$	Yes	No
[8]	dual	Filtering circuit	$0.022\lambda_0^3$	8.8dBi $\downarrow$	Yes	Yes
[12], [16]	dual	Stacked patch	$\geq 0.095\lambda_0^3 \uparrow$	$\approx 9.2\text{dBi} \downarrow$	No	No
[15]	dual	Stacked patch	$0.036\lambda_0^3 \uparrow$	5.2dBi $\downarrow$	No	No
[20], [22]	dual	Slots + Pins	$0.144\lambda_0^3 \uparrow$	9.5dBi $\downarrow$	No	Yes
[21], [24]	dual	Slots	$0.137\lambda_0^3 \uparrow$	9.5dBi $\downarrow$	No	No

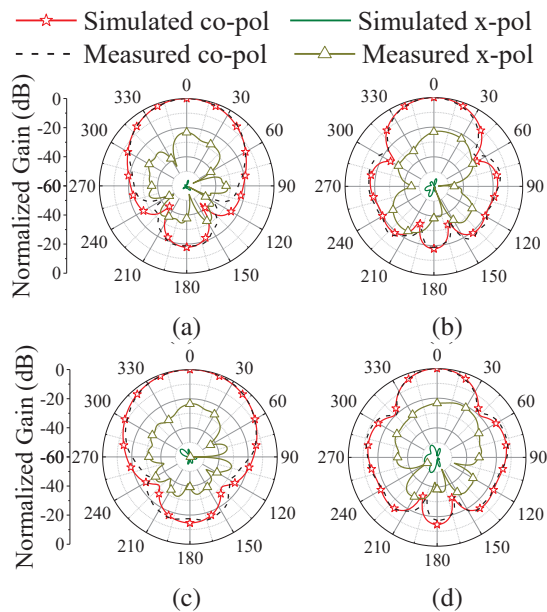


Fig. 15. Simulated and measured radiation patterns of the proposed antenna: (a) xoz plane at 2.37 GHz, (b) yoz plane at 2.37 GHz, (c) xoz plane at 2.49 GHz, and (d) yoz plane at 2.49 GHz.

antenna has obtained a stable peak gain of around 10.1 dBi in the operating frequency band, and the radiation efficiency of the antenna is around 90%. Hence, the proposed antenna has the single-layer, low-profile ( $0.038\lambda_0$ ), high-gain properties as desired without extra feeding networks.

Finally, a comparison between the proposed antenna and previous filtering antennas is presented in Table 1. The antennas in [10–11] exhibit good single-polarization filtering performance but cannot meet the requirements in a multi-polarization scenario. The antennas in [5], [7], and [8] achieved good filtering performance through the design of extra filter circuits, but these filter circuits increase design complexity and introduce insertion loss.

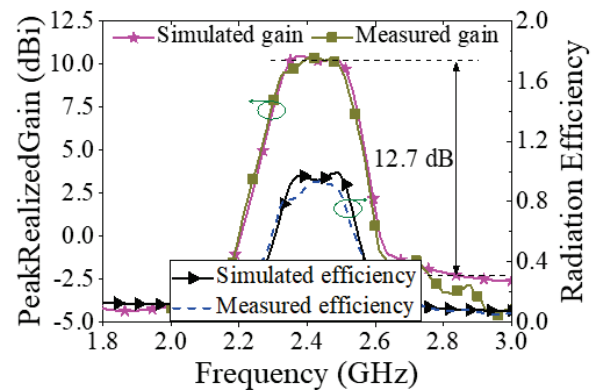


Fig. 16. Simulated and measured gains and efficiencies of the proposed antenna.

Additionally, the antennas in [12], [15], and [16] use the method of adding stacked patches to obtain good filtering performance, but they are not suitable for integration. Both the antenna proposed by us and the antennas in [20–22] and [24] achieve good filtering performance by slotting or loading shorting pins, and no extra filtering circuit is used. However, our proposed antenna has more advantages in terms of radiator volume and gain.

#### IV. CONCLUSION

In this paper, a novel dual-polarized filtering antenna without extra filtering circuit is proposed. Initially, the desired operating mode is selected by analyzing the electric field and radiation field of each characteristic mode. Next, the frequency spacing between the selected modes is reduced by slotting, and the radiation pattern with radiation nulls in broadside direction is improved. Finally, without using extra filter circuits, two flexibly controllable radiation nulls are introduced by loading the shorting pins inside the antenna and at the edge of the antenna, thus to achieve the wide impedance bandwidth and filtering performance of the realized gain simultaneously. The measured results indicate that the antenna has an

impedance bandwidth of 7.4% in the range of 2.34 - 2.52 GHz, and a stable peak gain of  $10.1 \pm 0.45$  dBi is obtained in the operating frequency band. In particular, the characteristics of low profile ( $0.038 \lambda_0$ ) and no extra filtering circuit make this antenna a good candidate for dual-polarization filtering applications.

### ACKNOWLEDGMENT

This work is supported by the National Natural Science Foundation of China under General Program (62271364), Key Research and Development Program of Shaanxi (Program No. 2023-GHZD-45), Fundamental Research Funds for the Central Universities (ZYTS23145), University of Macau (0080/2021/A2), and Special Grant CPG2023-00020-FST. (Corresponding author: Neng-Wu Liu)

### REFERENCES

- [1] C.-X. Mao, S. Gao, Y. Wang, F. Qin, and Q.-X. Chu, "Multimode resonator-fed dual-polarized antenna array with enhanced bandwidth and selectivity," *IEEE Trans. Antennas Propag.*, vol. 63, no. 12, pp. 5492-5499, Dec. 2015.
- [2] W.-J. Wu, Y.-Z. Yin, S.-L. Zuo, Z.-Y. Zhang, and J.-J. Xie, "A new compact filter-antenna for modern wireless communication systems," *IEEE Antennas Wireless Propag. Lett.*, vol. 10, pp. 1131-1134, 2011.
- [3] J.-F. Li, D.-L. Wu, G. Zhang, Y.-J. Wu, and C.-X. Mao, "Compact dual-polarized antenna for dual-band full-duplex base station applications," *IEEE Access.*, vol. 7, pp. 72761-72769, 2019.
- [4] C.-X. Mao, S. Gao, Y. Wang, Q. Luo, and Q.-X. Chu, "A shared-aperture dual-band dual-polarized filtering-antenna-array with improved frequency response," *IEEE Trans. Antennas Propag.*, vol. 65, no. 4, pp. 1836-1844, Apr. 2017.
- [5] Y. Zhang, X. Y. Zhang, L. Gao, Y. Gao, and Q. H. Liu, "A two-port microwave component with dual-polarized filtering antenna and single-band bandpass filter operations," *IEEE Trans. Antennas Propag.*, vol. 67, no. 8, pp. 5590-5601, Aug. 2019.
- [6] Y. Li, Z. Zhao, Z. Tang, and Y. Yin, "Differentially fed, dual-band dual-polarized filtering antenna with high selectivity for 5G sub-6 GHz base station applications," *IEEE Trans. Antennas Propag.*, vol. 68, no. 4, pp. 3231-3236, Apr. 2020.
- [7] S. J. Yang, Y. F. Cao, Y. M. Pan, Y. Wu, H. Hu, and X. Y. Zhang, "Balun-fed dual-polarized broadband filtering antenna without extra filtering structure," *IEEE Antennas Wireless Propag. Lett.*, vol. 19, no. 4, pp. 656-660, Apr. 2020.
- [8] J. Liu, H. Liu, X. Dou, Y. Tang, C. Zhang, L. Wang, R. Tang, and Y. Yin, "A low profile, dual-band, dual-polarized patch antenna with antenna-filter functions and its application in MIMO systems," *IEEE Access.*, vol. 9, pp. 101164-101171, 2021.
- [9] W. Duan, Y. F. Cao, Y.-M. Pan, Z. X. Chen, and X. Y. Zhang, "Compact dual-band dual-polarized base-station antenna array with a small frequency ratio using filtering elements," *IEEE Access.*, vol. 7, pp. 127800-127808, 2019.
- [10] P. F. Hu, Y. M. Pan, X. Y. Zhang, and S. Y. Zheng, "Broadband filtering dielectric resonator antenna with wide stopband," *IEEE Trans. Antennas Propag.*, vol. 65, no. 4, pp. 2079-2084, Apr. 2017.
- [11] K. Xu, J. Shi, X. Qing, and Z. N. Chen, "A substrate integrated cavity backed filtering slot antenna stacked with a patch for frequency selectivity enhancement," *IEEE Antennas Wireless Propag. Lett.*, vol. 17, no. 10, pp. 1910-1914, Oct. 2018.
- [12] W. Duan, X. Y. Zhang, Y.-M. Pan, J.-X. Xu, and Q. Xue, "Dual-polarized filtering antenna with high selectivity and low cross polarization," *IEEE Trans. Antennas Propag.*, vol. 64, no. 10, pp. 4188-4196, Oct. 2016.
- [13] Y. Liu, S. Wang, N. Li, J.-B. Wang, and J. Zhao, "A compact dual-band dual-polarized antenna with filtering structures for sub-6 GHz base station applications," *IEEE Antennas Wireless Propag. Lett.*, vol. 17, no. 10, pp. 1764-1768, Oct. 2018.
- [14] C. F. Ding, X. Y. Zhang, and M. Yu, "Simple dual-polarized filtering antenna with enhanced bandwidth for base station applications," *IEEE Trans. Antennas Propag.*, vol. 68, no. 6, pp. 4354-4361, June 2020.
- [15] S. J. Yang, Y. M. Pan, L.-Y. Shi, and X. Y. Zhang, "Millimeter-wave dual-polarized filtering antenna for 5G application," *IEEE Trans. Antennas Propag.*, vol. 68, no. 7, pp. 5114-5121, July 2020.
- [16] C. Hua, R. Li, Y. Wang, and Y. Lu, "Dual-polarized filtering antenna with printed Jerusalem-cross radiator," *IEEE Access.*, vol. 6, pp. 9000-9005, 2018.
- [17] Y. Zhang, Y. Zhang, D. Li, Z. Niu, and Y. Fan, "Dual-polarized low-profile filtering patch antenna without extra circuit," *IEEE Access.*, vol. 7, pp. 106011-106018, 2019.
- [18] Y. Y. Liu, X. Y. Zhang, and S. J. Yang, "Compact dual-band dual-polarized filtering antenna for 5G base station applications," *Proc. Int. Symp. Antennas Propag. (ISAP)*, pp. 791-792, 2021.
- [19] Y. F. Cao, X. Y. Zhang, and Q. Xue, "Compact shared-aperture dual-band dual-polarized array

- using filtering slot antenna and dual-function metasurface,” *IEEE Trans. Antennas Propag.*, vol. 70, no. 2, pp. 1120-1131, Feb. 2022.
- [20] W. Yang, M. Xun, W. Che, W. Feng, Y. Zhang, and Q. Xue, “Novel compact high-gain differential-fed dual-polarized filtering patch antenna,” *IEEE Trans. Antennas Propag.*, vol. 67, no. 12, pp. 7261-7271, Dec. 2019.
- [21] K. Xue, D. Yang, C. Guo, H. Zhai, H. Li, and Y. Zeng, “A dual-polarized filtering base-station antenna with compact size for 5G applications,” *IEEE Antennas Wireless Propag. Lett.*, vol. 19, no. 8, pp. 1316-1320, Aug. 2020.
- [22] Y. Q. Sun, Z. J. Zhai, D. H. Zhao, F. Lin, X. Y. Zhang, and H. J. Sun, “High-gain low cross-polarized dual-polarized filtering patch antenna without extra circuits,” *IEEE Antennas Wireless Propag. Lett.*, vol. 21, no. 7, pp. 1368-1372, July 2022.
- [23] S. J. Yang, Y. M. Pan, Y. Zhang, Y. Gao, and X. Y. Zhang, “Low-profile dual-polarized filtering magneto-electric dipole antenna for 5G applications,” *IEEE Trans. Antennas Propag.*, vol. 67, no. 10, pp. 6235-6243, Oct. 2019.
- [24] H. Yuan, F.-C. Chen, and Q.-X. Chu, “A wideband and high gain dual-polarized filtering antenna based on multiple patches,” *IEEE Trans. Antennas Propag.*, May 2022.
- [25] N.-W. Liu, L. Zhu, W.-W. Choi, and G. Fu, “A low-profile wideband aperture-fed microstrip antenna with improved radiation patterns,” *IEEE Trans. Antennas Propag.*, vol. 67, no. 1, pp. 562-567, Jan. 2019.
- [26] L. Zhu and N.-W. Liu, “Multimode resonator technique in antennas: A review,” *Electromagnetic Science*, vol. 1, no. 1, pp. 1-17, Mar. 2023.



**Zong-Zhuo Wang** was born in Liaocheng, China. He is currently pursuing the M.E degree from Xidian University, Xi’an, China. His current research interests include low-profile antennas, filtering antennas, and multifunctional antennas.



**Neng-Wu Liu** was born in Changde, China. Since 2018, he has been an associate professor with Xidian University. His current research interests include the designs of antenna theory, low-profile antennas, multimode antennas, wideband antennas, patch antennas, filtering antennas, and phased arrays.



**Liang Fang** was born in 1986, and he is a senior engineer at the AVIC Research Institute for Special Structures of Aeronautical Composites. His current research focuses on radio propagation and comprehensive design of electromagnetic windows.

# Wideband Center-fed Stacked Patch Circularly Polarized Antenna used in Phased Array

Jiaxin Wang<sup>1,2</sup>, Xiao Liu<sup>1</sup>, Pengfei Zhang<sup>1</sup>, Zheng Xu<sup>1</sup>, Anqi Li<sup>1</sup>, Zhengtian Chen<sup>1</sup>, and Jin Fan<sup>3</sup>

<sup>1</sup>Aerospace Information Research Institute  
Chinese Academy of Sciences, Beijing, 100190, China

<sup>2</sup>School of Electronic, Electrical and Communication Engineering  
University of Chinese Academy of Sciences, Beijing, 100190, China

<sup>3</sup>Beijing Institute of Control and Electronic Technology  
Beijing, 100074, China  
liuxiao@aircas.ac.cn

**Abstract** – A center-fed circularly polarized stacked patch antenna (CF-CPSPA) with enhanced axial-ratio (AR) bandwidth is proposed in this paper. The antenna is composed of two microstrip patches, the lower patch consists of a circular pad, an elliptical-ring, and two branch lines connecting them, which is used to realize the center-fed condition, and the upper patch is an elliptical patch to achieve the wide band performance. Firstly, two center-fed linearly polarized stacked patch antennas with wide band are designed, one mode radiated with  $x$  polarization, and the other generates  $y$  polarized radiation. Next, the orthogonal modes of two linearly polarized antennas are combined together by a specific design. Finally, the approximate equal amplitude and quadrature phase difference of the introduced modes are achieved in the operating frequency band with proper parameters analysis. And the impedance bandwidth and 3dB AR bandwidth is improved to 30.4% and 16.5%.

**Index Terms** – center-fed, stacked patch, unit in phased array, wideband circularly polarized antenna.

## I. INTRODUCTION

Circularly polarized (CP) antennas have been widely used in modern wireless communication systems due to the improved immunity to multipath interferences, polarization mismatch losses, and Faraday rotation effects [1–4]. Among the CP antennas, microstrip patch antennas are preferred because of the advantages of low profile, low cost, and easy integration [1].

CP patch antennas can be designed by a multi-fed technique or a single-fed technique [1]. The former can achieve a better axial ratio (AR) bandwidth compared with a single-fed antenna. However, the compli-

cated feeding networks limit their applications in phased arrays [5–9] when the unit spacing is restricted. For single-fed CP patch antennas, the AR bandwidth is generally narrow, and several methods have been proposed to enhance the AR bandwidth, such as using thick substrates with low permittivity to lower the high Q-factor [9], or using aperture coupling or some another coupling way to feed the patch antenna [10–12]. In [9], an approximately 12% 3 dB AR bandwidth was gained by using a foam substrate with thickness of  $0.2 \lambda_0$ .

Another way to enhance the AR bandwidth is to introduce multiple pairs of orthogonal modes, such as stacked patches. Currently, various stacked patch antennas have been proposed [13–21]. The stacked structures of metasurface and patch radiators provide an improved CP performance [22–24]. Several orthogonal linearly polarized (LP) modes are designed in [25, 26] with equal magnitude and quadrature phase difference. In [26], a stacked U-slot patch antenna is designed to generate five LP modes and four AR minima poles, and the 3 dB AR bandwidth is 55%. However, the planar size of this design limits its application in phased arrays.

In CP phased arrays, a sequential rotation is generally applied to suppress the cross-polarization [27]. To improve the scanning performance in the diagonal plane of the array, a secondary sequential rotation or a random sequential rotation is employed [28, 29]. Therefore, the center-fed CP antennas are significantly required in rotation arrays because the position of the feeding port will be unchanged when the element is rotated. This characteristic significantly simplifies the feeding structure from the transmit-receive (TR) modules to the antenna elements in the millimeter-wave phased arrays. However, the center-fed CP patch antennas were rarely investigated

in the past. Some center-fed CP patch antennas are proposed in [30, 31] with narrow AR bandwidths.

In this paper, a wide band CP stacked patch antenna fed by a coaxial probe located in the center of the lower patch is proposed. Firstly, two center-fed linearly polarized stacked patch antennas are designed. One generates two resonance modes in the  $x$  direction, and the other generates two resonance modes at higher frequencies in the  $y$  direction. Then, an elliptical design is applied to combine the orthogonal modes of two linearly polarized antennas together. Finally, with proper parameter analysis, the approximately equal magnitude and quadrature phase of the introduced split orthogonal modes are achieved in the band of interest. Compared with the center-fed patch antennas, the AR bandwidth of the proposed antenna is enhanced by an additional AR minima pole. The simulated and measured results are found in good agreement with each other, demonstrating that a -10 dB  $|S_{11}|$  bandwidth of 30.4% and a 3 dB AR bandwidth of 16.5% are achieved. The final results indicate that this design is a good candidate for millimeter-wave AiP phased arrays.

This paper is organized as follows: Section II introduces the configuration, working mechanism and design process, and parametric studies of the proposed antenna. Section III gives the simulation and measurement results of the proposed antenna. The last section is a brief summary.

## II. CENTER-FED CIRCULARLY POLARIZED STACKED PATCH ANTENNA

### A. Configuration

The configuration of the proposed center-fed circularly polarized stacked patch antenna (CF-CPSPA) is shown in Fig. 1. It consists of two TSM-DS3 dielectric substrates ( $\epsilon_{r1} = 2.94$ ,  $\tan\delta = 2.94$ ) with thickness of  $h_1$  and  $h_2$ , and two microstrip patches placed on them, respectively. The two substrates are bonded by FR28 material ( $\epsilon_{r1} = 2.76$ ,  $\tan\delta = 2.94$ ) with thickness of  $h_3$ . The size of the element is  $l_d \times l_d$ . The proposed antenna is fed by a coaxial probe located in the center of the lower patch. Moreover, a substrate integrated waveguide (SIW) back cavity based on the metalized vias is applied to suppress the propagation of surface waves and improve the scanning performance [34, 35], as shown in Fig. 1 (a).

The lower patch consists of a circular pad, an elliptical ring, and two branch lines connecting them as shown in Fig. 1 (b). The outer major radius and outer minor radius of the elliptical ring are  $r_{l1}$  and  $r_{s1}$ , and the inner radius is  $r_{in}$ . Also, the major axis is along the  $x$  axis, the two branch lines are at an angle of  $\theta_1$  and  $\theta_2$  relative to  $\varphi = 45^\circ$  plane. The upper patch is an elliptical patch whose direction of the major axis is consistent with that of the lower elliptical ring, as shown in Fig. 1 (c); the major radius and minor radius are  $r_{l2}$  and  $r_{s2}$ .

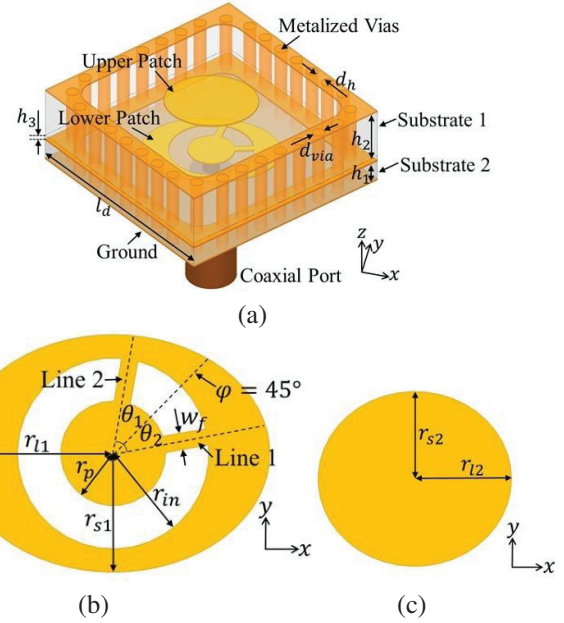


Fig. 1. Configuration of the proposed center-fed circularly polarized stacked patch antenna: (a) Perspective view, (b) lower patch, and (c) upper patch ( $r_{l1} = 1.64$ ,  $r_{s1} = 1.24$ ,  $r_{l2} = 1.11$ ,  $r_{s2} = 1$ ,  $r_{in} = 1$ ,  $r_p = 0.55$ ,  $\theta_1 = 35^\circ$ ,  $\theta_2 = 35^\circ$ ,  $r_p = 0.55$ ,  $w_f = 0.175$ ,  $h_1 = 0.508$ ,  $h_2 = 1.27$ ,  $h_3 = 0.11$ ,  $d_{via} = 0.3$ ,  $d_h = 0.6$ ,  $l_d = 5.5$ , all in millimetres).

### B. Working mechanism and design process

To illustrate the working mechanism of the proposed CF-CPSPA, four antennas with different configuration, named Ant. 1, Ant. 2, Ant. 3, and Ant. 4, are simulated and analyzed. The lower and upper patches of the four antennas are shown in Fig. 2, Ant. 1 and Ant. 2 are both linearly polarized, the upper and lower patches are circular, and the dimensional parameters are different. The directions of the two branch lines in the lower patch are orthogonal to each other. Ant. 3 and Ant. 4 are the proposed antenna structure in this paper. For Ant. 3, the parameters in  $xoz$  plane are the same as those of Ant. 1, and the parameters in  $yoz$  plane are the same as those of Ant. 2, and  $\theta_1$  and  $\theta_2$  are set as  $\theta_1 = \theta_2 = 45^\circ$ . Ant. 4 has the same parameters as listed in Fig. 1. Based on the studies of the four antennas, the design guidelines and methodology are summarized as follows. ( $f_0$  is the center operating frequency)

#### 1) Design of Ant. 1 and Ant. 2.

Figure 3 exhibits the simulated input resistance of Ant. 1 and Ant. 2. For Ant. 1, two resonance modes, mode  $1_a$  and mode  $1_b$ , are generated from the stacked patches. The initial parameters of the annular-ring patch can be calculated according to the formula given in [32], and the design of stacked patch antennas is referred to in [33]. As the centerline of the two branch lines in the

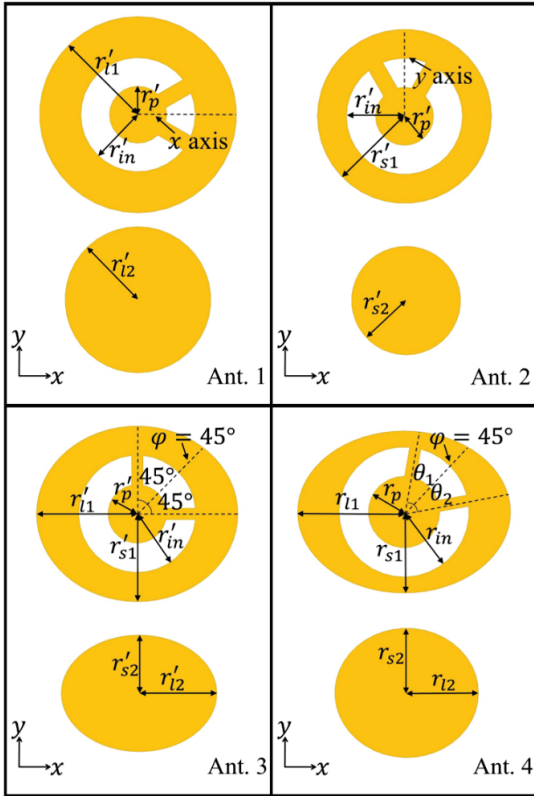


Fig. 2. Lower and upper patches of the four antennas ( $r'_{l1} = 1.55, r'_{s1} = 1.35, r'_{l2} = 1.2, r'_{s2} = 0.9, r'_{in} = 0.9, r'_p = 0.45$ , all in millimetres).

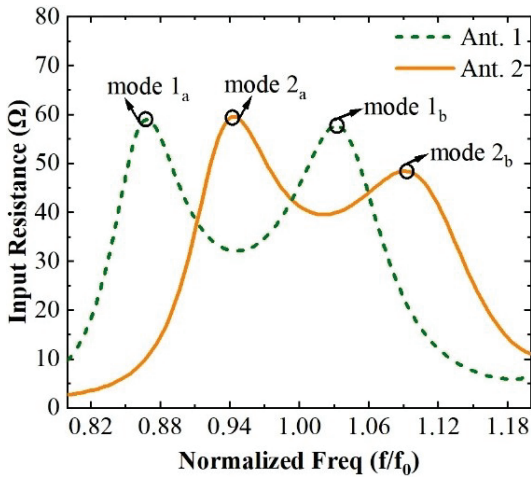


Fig. 3. Simulated input resistance of Ant. 1 and Ant. 2.

lower patch of Ant. 1 is along the  $x$  axis, the polarization of Ant. 1 is along the  $x$  direction. To further understand the two resonance modes, Fig. 4 displays the E-field distributions in the  $xoz$  plane of the two modes of Ant. 1. The E-field of mode  $1_a$  is concentrated between

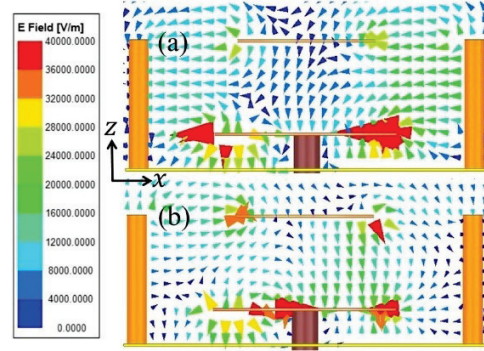


Fig. 4. Simulated E-field distributions in  $xoz$  plane of (a) mode  $1_a$  and (b) mode  $1_b$ .

the lower patch and the cavity, while for mode  $1_b$ , the coupling between the lower and upper patches is significantly enhanced. As for Ant. 2, two resonance modes, mode  $2_a$  and mode  $2_b$ , are generated at higher frequencies due to the smaller dimensional parameters. Moreover, the centerline of the two branch lines in the lower patch of Ant. 2 is along the  $y$  axis; therefore, the polarization of Ant. 2 is along the  $y$  direction, which means mode  $2_a$  and mode  $2_b$  are orthogonal to mode  $1_a$  and mode  $1_b$ .

2) Design of Ant. 3 with an elliptical patch.

Ant. 3 introduces mode  $1_a$  and mode  $1_b$  by setting the parameters in the  $xoz$  plane the same as those of Ant. 1, and introduce mode  $2_a$  and mode  $2_b$  by setting the parameters in the  $yo z$  plane the same as those of Ant. 2. Meanwhile, the variations of the parameters in the  $yo z$  plane affect mode  $1_a$  and mode  $1_b$  slightly, and the variations of the parameters in the  $xoz$  plane affect mode  $2_a$  and mode  $2_b$  slightly. Therefore, the operating frequency of the orthogonal mode can be adjusted separately. The two branch lines of the lower patch of Ant. 3 are reset along the  $x$  axis and  $y$  axis, respectively, to excite the introduced orthogonal modes. Figure 5 shows the magnitude of far-field broadside  $E_x$  and  $E_y$  components of Ant. 1, Ant. 2, and Ant. 3, and agreement of the working frequencies can be observed. The differences in the magnitude of  $E_x$  and  $E_y$  of the three antennas result from the coupling between modes. As shown in Fig. 6, there are two AR minima poles satisfying  $AR < 3\text{dB}$ , and if these two minima poles are close enough to each other, a wide 3dB AR bandwidth will be generated.

3) Tune the parameters to optimize the CP performance of Ant. 3.

To achieve approximately equal magnitude and quadrature phase difference of the orthogonal modes in the operating frequency band, the dimensional parameters of Ant. 3 need to be optimized. The critical parameters included the outer major radius of the lower patch ( $r_{l1}$ ), the ratio of  $r_{s1}$  to  $r_{l1}$  ( $ar_1=r_{s1}/r_{l1}$ ), the angle of

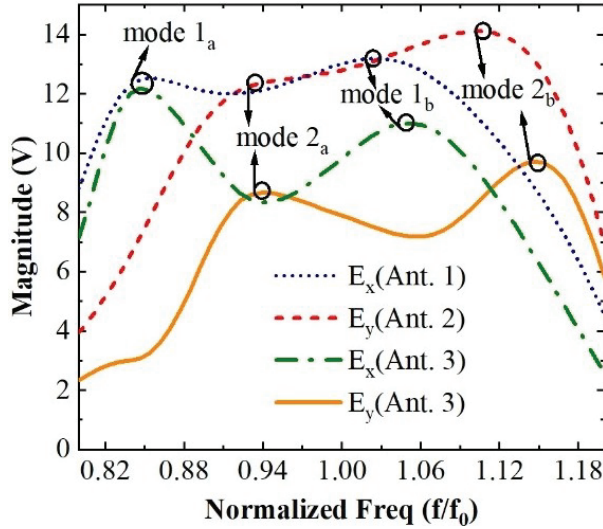


Fig. 5. Simulated magnitude of far-field broadside  $E_x$  and  $E_y$  components of Ant. 1, Ant. 2, and Ant. 3.

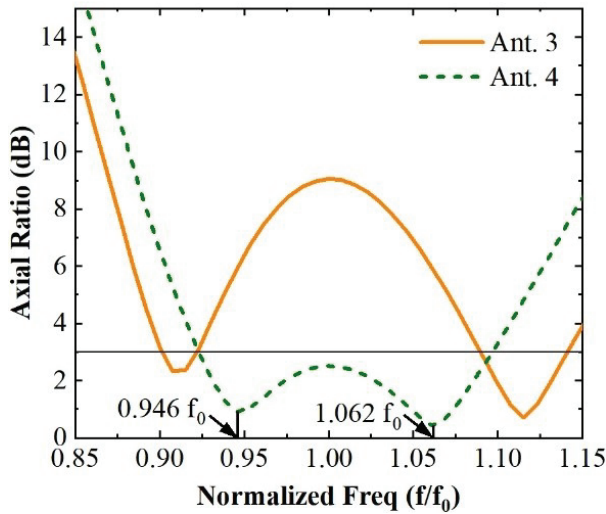


Fig. 6. Simulated boresight AR of Ant. 3 and Ant. 4.

the branch lines relative to the plane at  $\varphi = 45^\circ$  ( $\theta_1$ ,  $\theta_2$ ), and the major radius and minor radius of the upper elliptical patch ( $r_{l2}$ ,  $r_{s2}$ ) is slightly tuned. Finally, Ant. 4 is obtained, the simulated AR result is plotted in Fig. 6, showing an improved CP performance compared with Ant. 3, and a 3 dB AR bandwidth of 17.3% is realized.

Besides, Fig. 7 demonstrates the surface currents on the lower and upper patches of Ant. 4 varying with time. Whether at  $0.946f_0$  or  $1.062f_0$ , the surface currents on the upper and lower patches are both along the  $x$  direction when  $t = 0$ , and the surface currents on the upper and lower patches are both along the  $y$  direction when  $t = T/4$ , meeting the CP wave generation condition. The difference is that the surface current on the upper patch

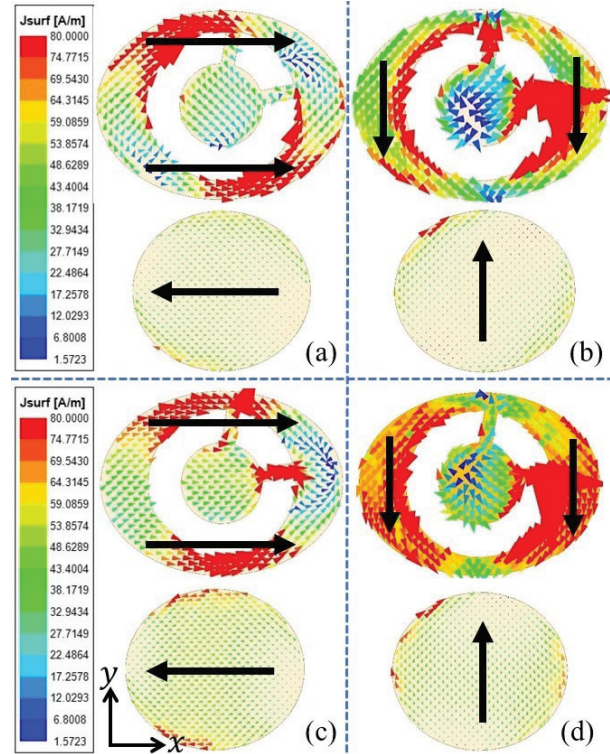


Fig. 7. Simulated surface currents on the lower and upper patches of Ant. 4: (a) When  $t = 0$  at  $0.946f_0$ , (b) when  $t = T/4$  at  $0.946f_0$ , (c) when  $t = 0$  at  $1.062f_0$ , and (d) when  $t = T/4$  at  $1.062f_0$ , where  $T$  is the period of time.

at  $1.062f_0$  is slightly stronger than that at  $0.946f_0$ , which is consistent with the coupling of the upper and lower patches being enhanced at higher frequencies, as displayed in Fig. 4.

### C. Effect of parameters on the far-field broadside $E_x$ and $E_y$ components

To quantitatively investigate the influence of the dimensional parameters on the CP performance, the effects of some critical parameters on the far-field broadside  $E_x$  and  $E_y$  components of the proposed CF-CPSPA are studied. Compared with AR,  $E_x$  and  $E_y$  components can reveal the CP performance more essentially and visibly. In this paper, to assess the  $E_x$  and  $E_y$  components, the parameter “ $rE$ ” in HFSS software is selected, which eliminates the effect of distance; in other words, the unit of “ $rE$ ” is “V”.

Figure 8 shows the effects of some critical parameters on the magnitude or the phase difference of  $E_x$  and  $E_y$  components of the proposed CF-CPSPA, including the ratio of  $r_{s1}$  to  $r_{l1}$  ( $ar_1 = r_{s1}/r_{l1}$ ), the angle of the branch lines relative to the plane at  $\varphi = 45^\circ$  ( $\theta_1$ ,  $\theta_2$ ), and the major radius and minor radius of the upper elliptical patch ( $r_{l2}$ ,  $r_{s2}$ ).

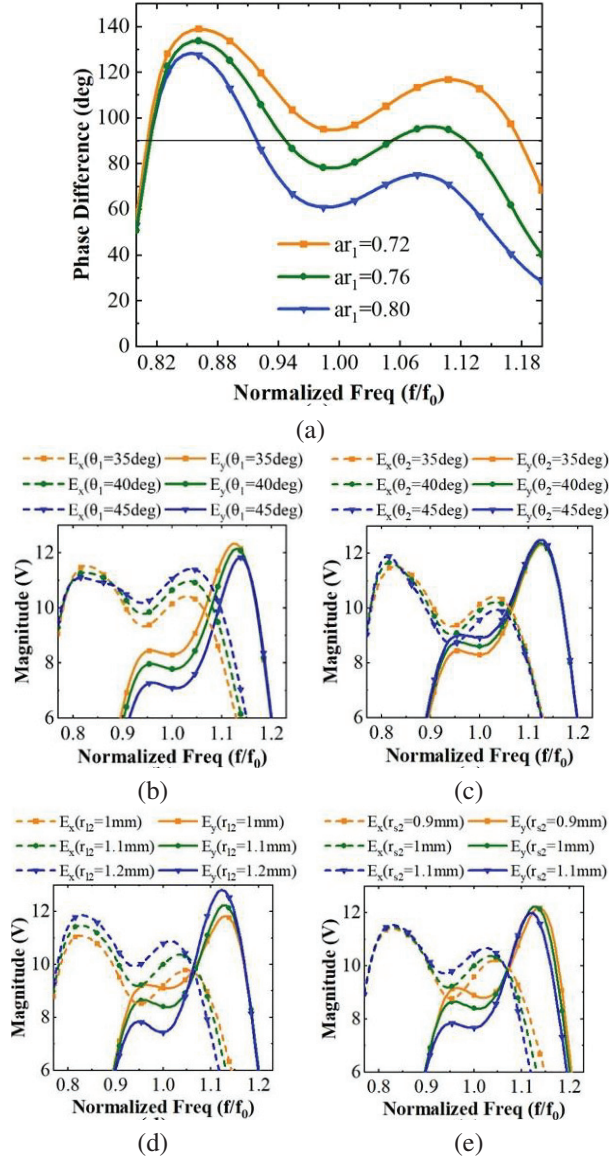


Fig. 8. Simulated results of the magnitude or phase difference of far-field broadside  $E_x$  and  $E_y$  components under different parameters: (a)  $ar_1$ , (b)  $\theta_1$ , (c)  $\theta_2$ , (d)  $r_{12}$ , and (e)  $r_{s2}$ .

As shown in Fig. 6 (a),  $ar_1$  mainly affects the phase difference of  $E_x$  and  $E_y$  components, and a phase difference of about  $90^\circ$  in the operating frequency band can be achieved with a proper value of  $ar_1$ .  $ar_1$  controls the ratio of  $r_{s1}$  to  $r_{11}$ , which splits the two pairs of degenerate resonance modes. Therefore,  $ar_1$  is the most important parameter for the CP performance and should be tuned first.

Figures 8 (b) and (c) exhibit the magnitude of  $E_x$  and  $E_y$  components at different values of  $\theta_1$  and  $\theta_2$ . It indicates that when line 1 is along the major axis of the

elliptical ring, i.e.,  $\theta_1 = 45^\circ$ , the two resonances of  $E_x$  are the most strongly excited, and as  $\theta_1$  reduces, both of the ring, i.e.,  $\theta_1 = 45^\circ$ , the two resonances of  $E_x$  are the most strongly excited, and as  $\theta_1$  reduces, both of the lower and upper resonances of  $E_x$  decrease, while the two resonances of  $E_y$  increase. The effect of  $\theta_2$  is just the opposite but weaker than that of  $\theta_1$ . The variation presents a principle that when the coupling to one mode increases, the coupling to the other mode at the same frequency will be reduced. This principle also works in the studies of other parameters.

As can be seen from Figs. 8 (d) and (e), when  $r_{12}$  increases, the magnitude of  $E_x$  increased, while the magnitude of  $E_y$  decreased at the lower frequency and increased at higher frequency. As  $r_{s2}$  increases, the lower resonance of  $E_y$  decreases, but the upper resonance does not increase due to the increase of high input resistance and the worsened matching at the upper resonant frequency.

The effects of some other parameters are not discussed in detail. When  $h_2$  increases, the resonant frequencies decrease and get closer. Keeping the difference of  $r_{11}$  and  $r_{12}$  fixed, the frequencies of the two resonances vary with  $r_1$ . As  $r_{in}$  and  $r_p$  increase, the overall input resistance increases.

### III. SIMULATED AND MEASURED RESULTS

According to the design steps above, the optimized dimensional parameters of the proposed CF-CPSPA are given in Fig. 1. And the magnitude and phase difference of the far-field broadside  $E_x$  and  $E_y$  components of the final antenna element are plotted in Fig. 9. At the frequencies of  $0.946f_0$  and  $1.062f_0$ , the magnitudes of the two orthogonal components are roughly equal and the

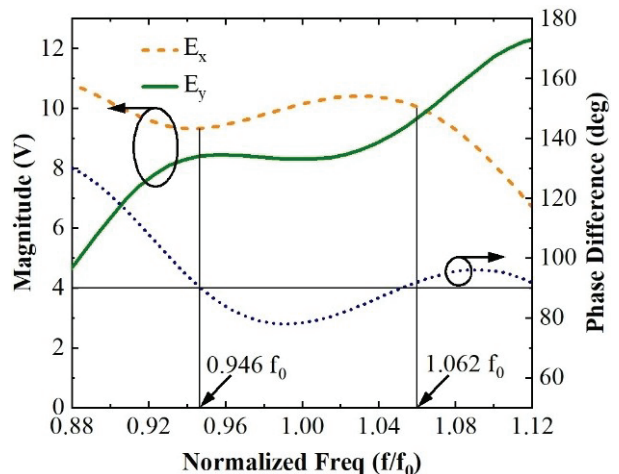


Fig. 9. Phase difference and magnitude of far-field broadside  $E_x$  and  $E_y$  components of the proposed CF-CPSPA.

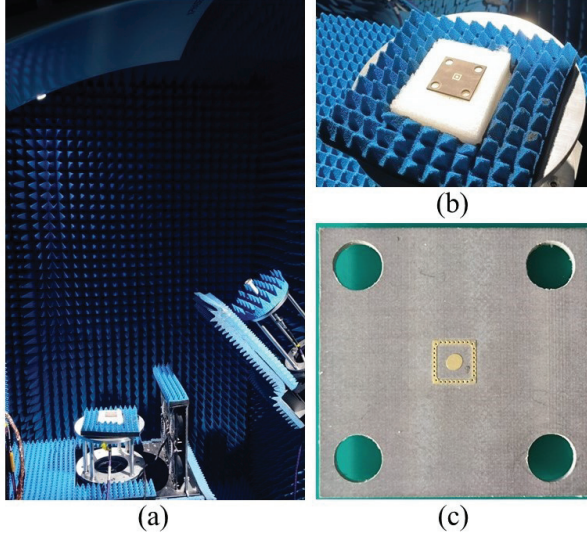


Fig. 10. Photographs of (a) the test environment, (b) the CF-CPSPA on the test bench, and (c) the top view of the CF-CPSPA.

phase difference is close to  $90^\circ$ , indicating two AR minima poles, as shown in Fig. 6. To validate the simulated results, a prototype is fabricated and measured, as shown in Fig. 10, and the size of the substrates and the metal ground are enlarged for easier fixing. The reflection coefficients and AR are measured as shown in Fig. 11.

As shown in Fig. 11 (a), the measured and simulated AR responses are found in good agreement with each other, the simulated and measured 3 dB AR bandwidths are  $0.923f_0 - 1.096f_0$  (17.3%) and  $0.942f_0 - 1.107f_0$  (16.5%), verifying an enhanced wideband performance. The tolerable frequency offset is mainly due to the enlarged metal ground and inevitable measurement errors. Figure 11 (b) exhibits the simulated and measured reflection coefficients and realized broadside LHCP gains. A  $-10$  dB  $|S_{11}|$  bandwidth from  $0.834f_0$  to  $1.138f_0$  GHz (30.4%) is achieved, which is well consistent with the simulated result. Besides, the realized broadside LHCP gain are between 4.9 and 6.0 dBic in the 3 dB AR bandwidth. Figure 12 shows the simulated and measured results of the normalized RHCP and LHCP far-field radiation patterns in  $xoz$  and  $yoZ$  planes, and a large angular beamwidth is observed. Note that, because of the enlarged metal ground, the forward radiation of the element increases, the measured gain is therefore slightly higher than the simulated gain, and the measured beamwidth is narrowed compared with the simulated results.

The measured performances of the proposed CF-CPSPA are tabulated in Table 1 and compared with other reported single-fed CP patch antennas. Compared with traditional CP stacked patch antennas [16, 19], our

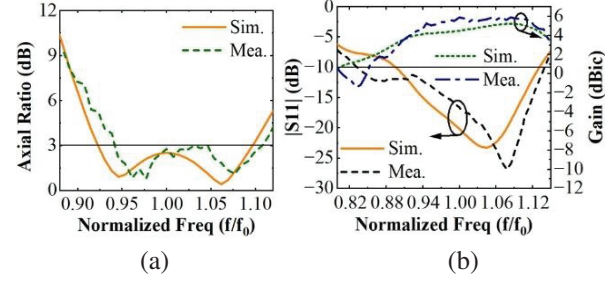


Fig. 11. Simulated and measured results of the proposed CF-CPSPA: (a) Bore-sight AR and (b)  $|S_{11}|$  and realized boresight LHCP gain.

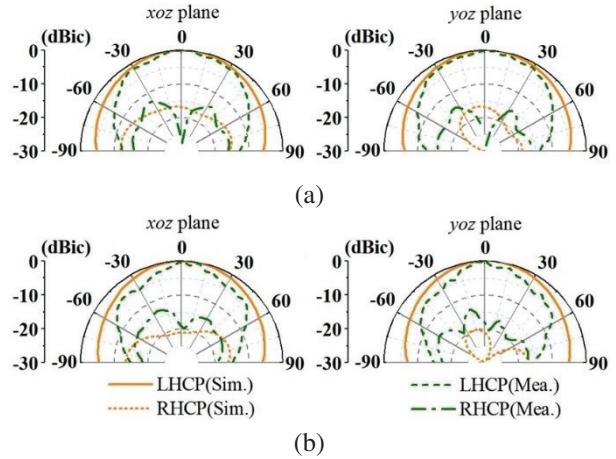


Fig. 12. Simulated and measured normalized radiation patterns of the proposed CF-CPSPA at (a)  $0.962f_0$  and (b)  $1.038f_0$ .

Table 1: Comparisons of different single-fed CP patch antennas

Ref.	Size ( $\lambda_0^3$ )	IMBW (%)	ARBW (%)	CF (Y/N)	Wideband Approaches
[9]	$0.42 * 0.42 * 0.221$	25.3	11.8	N	Thick air substrate
[16]	$0.30 * 0.30 * 0.160$	40	17.3	N	Stack patches, air spacing
[19]	$0.51 * 0.51 * 0.11$	25.8 VSWR < 1.5	13.5	N	Stack patches, meandering strip
[24]	$1.10 * 1.10 * 0.093$	34.7	20.1	N	Stack patches, metasurface
[26]	$0.48 * 0.48 * 0.226$	96.7	52.7	N	Stack patches, pentamode (4AR poles)
[30]	$0.52 * 0.52 * 0.044$		-	Y	-
Our Work	$0.48 * 0.48 * 0.164$	30.4	16.5	Y	Stack patches

$\lambda_0$ : The free-space wavelength at the center operating frequency  $f_0$ . IMBW: Impedance bandwidth, default is  $-10$  dB  $|S_{11}|$  bandwidth. ARBW: 3 dB AR bandwidth. CF: Whether the antenna is center-fed.

proposed CF-CPSPA has similar impedance bandwidth and AR bandwidth. Meanwhile, it has the characteristic of being center-fed. And compared with existing center-fed CP patch antennas [30], our proposed CF-CPSPA has much wider impedance bandwidth and AR bandwidth. Besides, the proposed CF-CPSPA is easy to design (compared with [26]) and meets the spacing requirement of the wide-angle scanning (compared with [24]).

#### IV. CONCLUSION

In this paper, a center-fed CP stacked patch antenna has been proposed to improve the AR bandwidth. By an elliptical patch design, the orthogonal linearly polarized modes are combined together in the proposed antenna. The working mechanism and design process have been illustrated, and the effect of antenna parameters on the far-field broadside  $E_x$  and  $E_y$  components has been investigated. Then, the proposed antenna is fabricated and measured. The simulated and measured results are consistent with each other, showing a -10 dB  $|S_{11}|$  bandwidth of 30.4% and a 3 dB AR bandwidth of 16.5%. The final results indicate that the proposed antennas will be promising candidates for millimeter-wave AiP phased arrays.

#### REFERENCES

- [1] S. Gao, Q. Luo, and F. Zhu, *Circularly Polarized Antennas*, Hoboken, NJ, USA: Wiley, Nov. 2013.
- [2] M. Z. Xiao, H. Liu, and Y. H. Cui, "Broadband circularly polarized antennas with improved gain," *Applied Computational Electromagnetics Society (ACES) Journal*, vol. 34, no. 10, pp. 1514-1519, Oct. 2019.
- [3] R. Ma and Q. Y. Feng, "Broadband CPW-fed circularly polarized square slot antenna for universal UHF RFID handheld reader," *Applied Computational Electromagnetics Society (ACES) Journal*, vol. 36, no. 6, pp. 747-754, Nov. 2021.
- [4] B. S. Qiu, Y. F. Xia, and Y. S. Li, "Gain-enhanced wideband circularly polarized antenna with a non-uniform metamaterial reflector," *Applied Computational Electromagnetics Society (ACES) Journal*, vol. 37, no. 3, pp. 281-286, July 2022.
- [5] S. D. Targonski and D. M. Pozar, "Design of wideband circularly polarized aperture-coupled microstrip antennas," *IEEE Trans. Antennas Propag.*, vol. 41, no. 2, pp. 214-220, Feb. 1993.
- [6] L. Bian, Y.-X. Guo, L. C. Ong, and X.-Q. Shi, "Wideband circularly-polarized patch antenna," *IEEE Trans. Antennas Propag.*, vol. 54, no. 9, pp. 2682-2686, Sep. 2006.
- [7] Y.-X. Guo, L. Bian, and X. Q. Shi, "Broadband circularly polarized annular-ring microstrip antenna," *IEEE Trans. Antennas Propag.*, vol. 57, no. 8, pp. 2474-2477, Aug. 2009.
- [8] C.-F. Liang, Y.-P. Lyu, D. Chen, and C.-H. Cheng, "Wideband circularly polarized stacked patch antenna based on TM<sub>11</sub> and TM<sub>10</sub>," *IEEE Trans. Antennas Propag.*, vol. 70, no. 4, pp. 2459-2467, Apr. 2022.
- [9] S. S. Yang, K.-F. Lee, and A. A. Kishk, "Design and study of wideband single feed circularly polarized microstrip antennas," *Prog. Electromagn. Res.*, vol. 80, pp. 45-61, 2008.
- [10] P. Sullivan and D. Schaubert, "Analysis of an aperture coupled microstrip antenna," *IEEE Trans. Antennas Propag.*, vol. 34, no. 8, pp. 977-984, Aug. 1986.
- [11] J.-S. Row, "Design of aperture-coupled annular-ring microstrip antennas for circular polarization," *IEEE Trans. Antennas Propag.*, vol. 53, no. 5, pp. 1779-1784, May 2005.
- [12] H. Al-Saedi, W. M. Abdel-Wahab, S. Gigoyan, R. Mittra, and S. Safavi-Naeini, "Ka-band antenna with high circular polarization purity and wide AR beamwidth," *IEEE Antennas Wireless Propag. Lett.*, vol. 17, no. 9, pp. 1697-1701, Sep. 2018.
- [13] K. P. Nasimuddin, Esselle, and A. K. Verma, "Wideband circularly polarized stacked microstrip antennas," *IEEE Antennas Wireless Propag. Lett.*, vol. 6, pp. 21-24, 2007.
- [14] Z.-X. Liu, L. Zhu, and X. Zhang, "A low-profile and high-gain CP patch antenna with improved AR bandwidth via perturbed ring resonator," *IEEE Antennas Wireless Propag. Lett.*, vol. 18, no. 2, pp. 397-401, Feb. 2019.
- [15] S. Shekhawat, P. Sekra, D. Bhatnagar, V. K. Saxena, and J. S. Saini, "Stacked arrangement of rectangular microstrip patches for circularly polarized broadband performance," *IEEE Antennas Wireless Propag. Lett.*, vol. 9, pp. 910-913, 2010.
- [16] K. L. Chung and A. S. Mohan, "A systematic design method to obtain broadband characteristics for singly-fed electromagnetically coupled patch antennas for circular polarization," *IEEE Trans. Antennas Propag.*, vol. 51, no. 12, pp. 3239-3248, Dec. 2003.
- [17] N. Yan, K. Ma, and Y. Luo, "An SISL sequentially rotated feeding circularly polarized stacked patch antenna array," *IEEE Trans. Antennas Propag.*, vol. 68, no. 3, pp. 2060-2067, Mar. 2020.
- [18] T.-N. Chang and J.-M. Lin, "Circularly polarized ring-patch antenna," *IEEE Antennas Wireless Propag. Lett.*, vol. 11, pp. 26-29, 2012.

- [19] Z. Wang, S. Fang, S. Fu, and S. Jia, "Single-fed broadband circularly polarized stacked patch antenna with horizontally meandered strip for universal UHF RFID applications," *IEEE Trans. Microw. Theory Tech.*, vol. 59, no. 4, pp. 1066-1073, Apr. 2011.
- [20] Q. W. Lin, H. Wong, X. Y. Zhang, and H. W. Lai, "Printed meandering probe-fed circularly polarized patch antenna with wide bandwidth," *IEEE Antennas Wireless Propag. Lett.*, vol. 13, pp. 654-657, 2014.
- [21] W. Yang, J. Zhou, Z. Yu, and L. Li, "Single-fed low profile broadband circularly polarized stacked patch antenna," *IEEE Trans. Antennas Propag.*, vol. 62, no. 10, pp. 5406-5410, Oct. 2014.
- [22] S. X. Ta and I. Park, "Low-profile broadband circularly polarized patch antenna using metasurface," *IEEE Trans. Antennas Propag.*, vol. 63, no. 12, pp. 5929-5934, Dec. 2015.
- [23] K. E. Kedze, H. Wang, and I. Park, "A metasurface-based wide-bandwidth and high-gain circularly polarized patch antenna," *IEEE Trans. Antennas Propag.*, vol. 70, no. 1, pp. 732-737, Jan. 2022.
- [24] N. Hussain, M.-J. Jeong, A. Abbas, T.-J. Kim, and N. Kim, "A metasurface-based low-profile wide-band circularly polarized patch antenna for 5G millimeter-wave systems," *IEEE Access*, vol. 8, pp. 22127-22135, 2020.
- [25] N.-W. Liu, L. Zhu, Z.-X. Liu, G. Fu, and Y. Liu, "Design approach of a single circularly polarized patch antenna with enhanced AR-bandwidth under triple-mode resonance," *IEEE Trans. Antennas Propag.*, vol. 68, no. 8, pp. 5827-5834, Aug. 2020.
- [26] J. Zeng, Z. Zhang, F. H. Lin, and F. Guan, "Penta-mode ultrawideband circularly polarized stacked patch antennas using characteristic mode analysis," *IEEE Trans. Antennas Propag.*, vol. 70, no. 10, pp. 9051-9060, Oct. 2022.
- [27] J. Huang, "A technique for an array to generate circular polarization with linearly polarized elements," *IEEE Trans. Antennas Propag.*, vol. 34, no. 9, pp. 1113-1124, Sep. 1986.
- [28] A. B. Smolders and H. J. Visser, "Low side-lobe circularly-polarized phased arrays using a random sequential rotation technique," *IEEE Trans. Antennas Propag.*, vol. 62, no. 12, pp. 6476-6481, Dec. 2014.
- [29] J. Wen, Z. H. Huang, Y. L. Yao, Y. Zhang, J. H. Wang, L. P. Hou, and Y. H. Liang, "Cross polarization suppression of sequentially rotated circularly polarized phased array," *Telecommunication Engineering*, vol. 61, no. 8, pp. 956-964, 2021.
- [30] L. L. Xue, W. T. Fang, J. Xu, C. Ji, and F. F. Qu, "Design of a circularly polarized antenna using central feed," *Radio Engineering*, vol. 51, no. 4, pp. 308-312, 2021.
- [31] H. K. Kan and R. B. Waterhouse, "Low cross-polarised patch antenna with single feed," *Electronics Letters*, vol. 43, no. 2007, pp. 9-10, 2007.
- [32] X. Chen, G. Fu, S.-X. Gong, Y.-L. Yan, and W. Zhao, "Circularly polarized stacked annular-ring microstrip antenna with integrated feeding network for UHF RFID readers," *IEEE Antennas Wireless Propag. Lett.*, vol. 9, pp. 542-545, 2010.
- [33] F. Croq and D. M. Pozar, "Millimeter-wave design of wide-band aperture-coupled stacked microstrip antennas," *IEEE Trans. Antennas Propag.*, vol. 39, no. 12, pp. 1770-1776, Dec. 1991.
- [34] M. H. Awida, A. H. Kamel, and A. E. Fathy, "Analysis and design of wide-scan angle wide-band phased arrays of substrate-integrated cavity-backed patches," *IEEE Trans. Antennas Propag.*, vol. 61, no. 6, pp. 3034-3041, June 2013.
- [35] S. E. Valavan, D. Tran, A. G. Yarovoy, and A. G. Roederer, "Planar dual-band wide-scan phased array in x-band," *IEEE Trans. Antennas Propag.*, vol. 62, no. 10, pp. 5370-5375, Oct. 2014.



**Jiaxin Wang** was born in Benxi, Liaoning. He received the B.S. degree in electrical information science and technology from Tsinghua University, Beijing, China, in 2021. He is currently working toward the M.S. degree in electromagnetic field and microwave technology with the School of Electronic, Electrical and Communication Engineering, University of Chinese Academy of Sciences, Beijing, China.

His research interests include antenna theory and design, especially in circularly polarized antennas.



**Xiao Liu** received the M.S. degree from Beijing Institute of Technology, Beijing, China, in 2009 and the Ph.D. degree from the University of Chinese Academy of Sciences, Beijing, China, in 2023. Xiao Liu has been involved in the research and engineering implementation of

active phased array antennas and integrated process technology.



**Pengfei Zhang** received the B.Eng. degree and Ph.D. degree from the University of Electronic Science and Technology of China, Chengdu, China, in 2015 and 2021. Since 2022, he has been a postdoctoral and research assistant in Aerospace Information Research Institute, Chinese Academy of Sciences, Beijing, China. His research interests include planer leaky-wave antennas and active phased array antennas.



**Zheng Xu** received the B.S. degree and M.S. degree from Beijing Institute of Technology, Beijing, China, in 2006 and 2008. He received the Ph.D. degree from University of Chinese Academy of Sciences, Beijing, China. His research interests focus on digital phased array antenna technology, intelligent integrated microsystems, and multi-functional radar systems.



**Anqi Li** was born in Hunan, China, in 1994. He received the M.S. degree from the school of Electronics and Information Engineering, Beihang University, Beijing, China, in 2019. His current research interests include phased arrays design and measurement.



**Zhengtian Chen** received the M.S. degree from University of Electronic Science and Technology of China, Chengdu, China, in 2020. Zhengtian Chen has extensively participated in the research and engineering applications of active phased array antennas and T/R modules.



**Fan Jin** was born in Lichuan, Hubei. He received the Ph.D. degree in communication and information systems from the Graduate School of China Academy of Sciences, Beijing, China, in 2010. At present, he is the senior engineer in Beijing Institute of Control and Electronic Technology of CASIC, mainly engaged in communication system design. His research interests include communication system engineering and antenna array signal processing.

# Miniaturized Wideband Circularly Polarized Triangular Patch Antennas based on Characteristic Mode Analysis

Tian-Long Yang<sup>1</sup>, Xiao Zhang<sup>1\*</sup>, Qiong-Sen Wu<sup>2</sup>, and Tao Yuan<sup>1</sup>

<sup>1</sup>College of Electronics and Information Engineering  
Shenzhen University, Shenzhen, 518060, China  
xiao.zhang@szu.edu.cn

\*Corresponding Author

<sup>2</sup>School of Integrated Circuits  
Guangdong University of Technology, Guangzhou, 510006, China

**Abstract** – A miniaturized, wideband circularly polarized (CP) antenna based on coupled triangular patches is presented. Initially, two identical triangular patches with shorting pins are placed close to each other in a perpendicular orientation. Hence, a pair of orthogonal modes can be produced based on the coupled resonators. Under the characteristic mode analysis (CMA), it can be found that the 90° phase difference is achieved by modulating gap distance and shorting pins numbers. Both the shape of triangle patches and shorting pins contribute to the miniaturization. To further improve the AR bandwidth, a third patch is added to form a new mode. Thanks to the triple modes produced by the three patch elements, two AR minima are constructed to broaden the AR bandwidth. With this compact arrangement and shorting pins, a miniaturized wideband CP patch antenna with a 5.2% AR bandwidth is successfully implemented. The overall size of the antenna is merely  $0.34\lambda_0 \times 0.33\lambda_0 \times 0.046\lambda_0$ .

**Index Terms** – Antenna miniaturization, characteristic mode analysis, circularly polarized patch antennas, triangular patches, wideband patch antennas.

## I. INTRODUCTION

Wideband circularly polarized (CP) patch antennas play an important role in wireless communication and sensing systems. They are also capable of consistent polarized orientation between transmitter and receiver, reduction of Faraday rotation effects, and mitigating multi-path distortion [1]. CP antennas with compact structures and low profiles are highly needed in size-limited devices, such as satellite communications, wireless sensors, and unmanned aerial vehicles.

Traditional CP antennas have a relatively narrow axial-ratio (AR) band because a pair of degenerate modes as orthogonal components are not able to support equal amplitude and stable 90° phase difference in wide-

band. To extend AR bandwidths, three kinds of techniques have been proposed: multi-ports feeding networks [2–7], lower quality factor [8–15], and multi-mode techniques [16–25].

The *first* technique, using dual-ports [2–4] and sequential-phase [5–7] feed networks, can introduce additional AR bandwidth. However, the extraordinarily coupled resonators would inevitably increase the patch antenna's profile [2] and occupy more space [3–4]. Power divider [5] also decreases antennas' total efficiency, and shorting strips [6–7] between antennas make the system not suitable for integration. The *second* technique is to decrease the quality factor of antennas, which can be realized by a thicker substrate [8–15]. To compensate inductance of the probe and realize impedance matching, the capacitive coupling feed [8–9, 13–15] and slot-loaded patch [10–13] are proposed. However, the increased AR bandwidths are still limited, and antennas are relatively thick. The *third* technique, based on the multi-mode technique, can introduce more AR minima and increase AR bandwidths. For instance, metasurface [17], stacked patches [16, 18], and parasitic patches [20–21] are introduced above or around the driven patch as parasitic elements. Fewer numbers of parasitic patch elements can also be realized if a 90° phase difference is introduced between adjacent elements [22–23] or modes [24–25]. In [22], a quantitative design method based on the equivalent circuit model is proposed. With this method, multiple minima in the axial ratio response are produced by employing several adjacent coupled radiators, resulting in wideband CP radiation. In general, half-wavelength resonators or high-order modes are usually utilized to design wideband CP antennas, whereas there is little consideration for miniaturization.

In this paper, miniaturized wideband CP patch antennas using coupled radiators are proposed. To begin with, a narrow band CP antenna is designed based on

a pair of closely spaced triangular patch antennas with shorting fences, as shown in Fig. 1 (a). A 90° phase difference is achieved between two orthogonal patches due to the electromagnetic coupling for fringing fields. It can be flexibly adjusted by different gap dimensions and pin numbers. After that, the third patch is coupled with the former ones to produce triple modes in general. The whole of them can generate two AR minima and extend CP bandwidth, as shown in Fig. 1 (b). Different from traditional wideband CP antennas, the proposed one is based on multi-modes generated by multi-radiators instead of two adjacent elements. Besides, both the quarter-wavelength triangle patches and sequentially close arrangement in a counterclockwise direction contribute to a more compact and miniaturized antenna prototype.

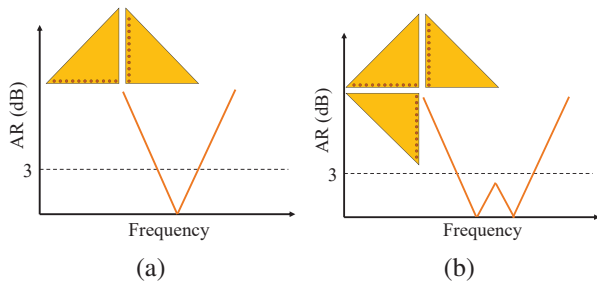


Fig. 1. Process of the evolution of the proposed CP antenna: (a) CP antenna I with single AR minimum and (b) wideband CP antenna II with two AR minima.

**II. NARROW BAND CP PATCH ANTENNA WITH ONE AR MINIMUM**

A miniaturized narrow band CP patch antenna is proposed in this section, as shown in Fig. 2. A pair of triangular patches are printed on the top of the 0.813 mm-thick dielectric substrate Rogers4003 ( $\epsilon_r = 3.55$ ,  $\tan\delta = 0.003$ ). They are arranged orthogonally, and both are closely spaced to be coupled with each other. A row of shorting pins is inserted at the right-angle edge of each patch. Hence the patches can operate at quarter-wavelength modes. The hypotenuse of triangular patches can also contribute to miniaturization. A coaxial probe is soldered on the finite ground to excite two orthogonal modes simultaneously, which will be demonstrated in the following using characteristic mode analysis.

**A. CMA of two coupled triangular patches**

Characteristic mode theory is full of physical meaning, and it is effective in antenna design to reveal the operating modes. Following the theory of characteristic modes (CMs) for PEC objects [26–27], a generalized eigenvalue equation can be written as

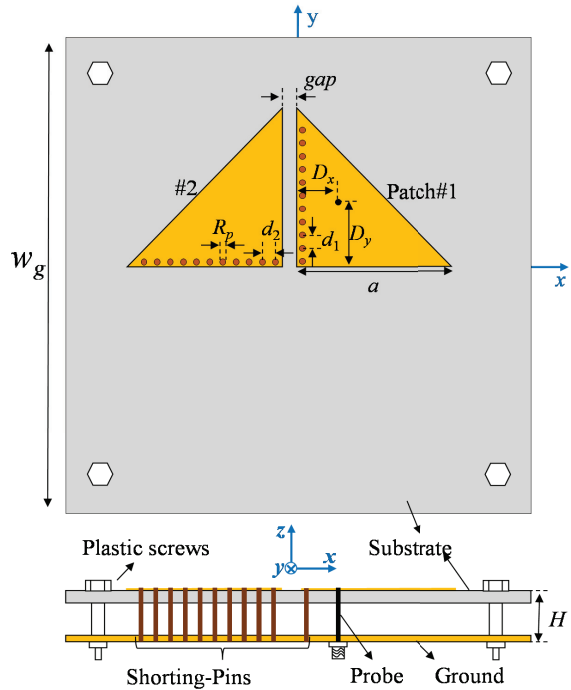


Fig. 2. Geometry of the proposed CP patch antenna I. Dimensions are  $W_g = 120, a = 38.5, \text{gap} = 0.8, D_x = 8, D_y = 16, d_1 = d_2 = 3.65, R_p = 1.2, H = 8.813$  (unit: mm), pin number  $N_{p1} = N_{p2} = 10$ .

$$\mathbf{X}\mathbf{J}_n = \lambda_n \mathbf{R}\mathbf{J}_n, \tag{1}$$

where  $\lambda_n$  is the eigenvalue associated with each characteristic current and  $\mathbf{J}_n$ .  $\mathbf{R}$ , and  $\mathbf{X}$  are the real and imaginary Hermitian parts of the matrix  $\mathbf{Z}$ , respectively. Model significance (MS) and characteristic angle (CA) are other two helpful indicators, and they are defined as

$$\text{MS}_n = \frac{1}{|1 + j\lambda_n|}, \tag{2}$$

$$\text{CA}_n = 180^\circ - \tan^{-1}\lambda_n. \tag{3}$$

The associated modes are resonant modes when  $\lambda_n = 0$ ,  $\text{MS}_n = 1$ , and  $\text{CA}_n = 180^\circ$ . In characteristic mode analysis (CMA), a pair of orthogonal modes with equal amplitude and 90° phase difference can be used to produce CP waves [28]. The difference in the two modes’ characteristic angles is related to the phase difference of their radiated far fields. If the port is placed where the two modes have equal characteristic current amplitude, modal significance can reflect the amplitude of CMs. In this work, the CST Studio Suite 2021 will be used to analyze the CMs of antennas.

To reveal the working principle of the proposed narrow band CP patch antenna I in Fig. 2, CMA is conducted with an infinite substrate and ground plane. Its modal significance and characteristic angle are shown

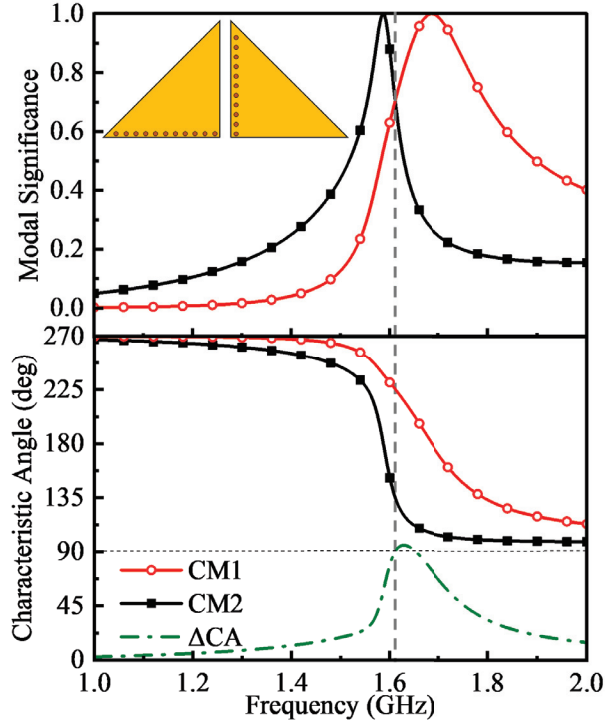


Fig. 3. MS and CA of CP patch antenna I.

in Fig. 3. There are two potential CMs in the operating band of antenna I. CM1 and CM2 are resonant at 1.586 GHz and 1.686 GHz, respectively. Note that the  $90^\circ$  phase difference between the two CMs is achieved because of electromagnetic coupling between two identical antennas [29]. Besides, both share the same magnitude of modal significance (MS) at 1.603 GHz. To excite the two modes with the same amplitude, shown in Fig. 2, the probe is fed the right patch #1 where the current magnitude of the two modes is approximately equal.

Characteristic currents as well as modal patterns are also depicted in Fig. 4. It can be found that the two modes have orthogonal characteristic currents in Figs. 4 (a) and (b). For CM1, the total equivalent currents mainly flow in  $-45^\circ$  direction, while for CM2 the total equivalent currents mainly flow in  $+45^\circ$  direction. Figs. 4 (c) and (d) show the modal radiation patterns of the CMs. It shows that both modes have broadside radiation patterns.

## B. Parametric study

Coupling strength between two adjacent resonators is of great importance in designing bandpass filters. In the same way, it is also the key to designing CP antennas based on coupled resonators. To achieve the required  $90^\circ$  phase difference between the two modes, a parametric study of the proposed antennas is conducted. In brief, both the coupling gap between the two patches and the number of loaded pins are the key parameters to modu-

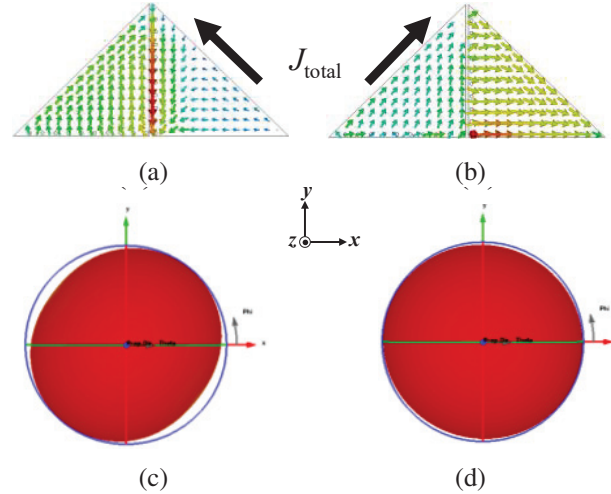


Fig. 4. Characteristic currents and modal radiation patterns of the antenna I: (a) and (c) CM1 at 1.586 GHz, (b) and (d) CM2 at 1.686 GHz.

lating the coupling strength.

Increasing the number of loaded pins in the patch #1 ( $N_{p1}$ ) can dramatically raise CM1's resonant frequency. For example, in Fig. 5 (a), increasing  $N_{p1}$  from 3 to 10 leads to an increase in the resonant frequency of CM1 from 1.53 to 1.68 GHz when  $gap = 2$  mm,  $N_{p2} = 10$ . However, the resonant frequency of CM2 remains approximately constant at 1.703 GHz.

Gap distance can also dramatically affect CM1's resonant frequency. In Fig. 5 (b), by increasing gap distance between patches, the resonant frequency of CM2 is almost unchanged while that of CM1 rises under the condition of fixed pins  $N_{p1}$  and  $N_{p2}$ .

To obtain further insight into how the pin number and gap width impact the CP performance, the full-wave simulation is carried out. The magnitude and phase difference of  $E_\theta$  and  $E_\phi$  at broadside with different pin numbers, and gap dimensions are shown in Figs. 6 and 7,

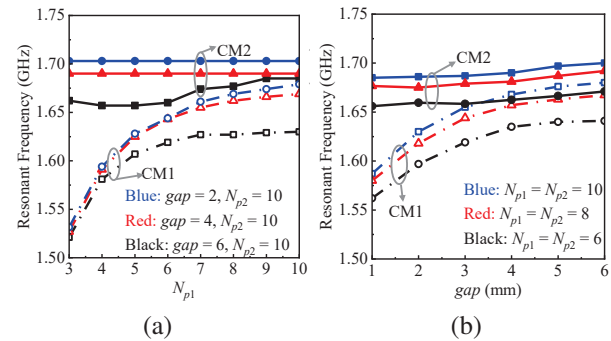


Fig. 5. Modes' resonant frequencies of proposed antenna I as a function of (a) varied  $N_{p1}$  and (b) varied  $gap$ .

respectively. In Fig. 6 (a), although  $N_{p1}$  varies from 4 to 10, the frequency with  $|E_\theta| = |E_\phi|$  is maintained at 1.58 GHz. However, the phase difference has decreased with increased  $N_{p1}$ . In Fig. 6 (b), the AR responses with respect to different values of  $N_{p1}$  show that the AR minimum occurs at 1.58 GHz. The sole AR minimum will degenerate with fewer pins, as a result of phase change.

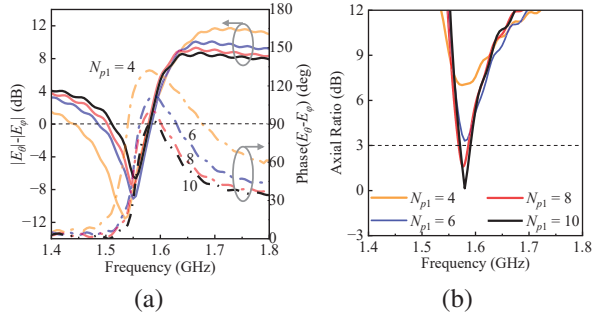


Fig. 6. Simulated results of antenna I with respect to different values of  $N_{p1}$ : (a) magnitude and phase difference of  $E_\theta$  and  $E_\phi$  at broadside and (b) AR responses at broadside.

In Fig. 7 (a), as the *gap* varies from 0.4 to 1.2 mm, the frequency with  $|E_\theta| = |E_\phi|$  rises from 1.465 to 1.645 GHz. The phase difference decreases at the same time. The frequency of the AR minimum also varies from 1.465 to 1.645 GHz. When the *gap* equals 0.8 mm, both the same amplitude and a 90° phase difference are satisfied simultaneously. As a result, the best CP performance with a minimum AR value of 0.15 dB is successfully achieved at 1.58 GHz. The 3dB-AR bandwidth is from 1.57 to 1.59 GHz (1.3%), as shown in the black curve in Fig. 7 (b).

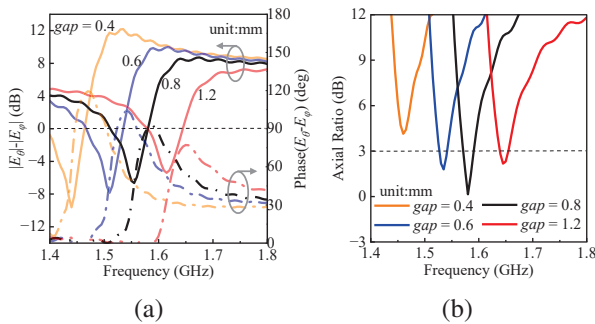


Fig. 7. Simulated results of antenna I with respect to different values of *gap*: (a) Magnitude and phase difference of  $E_\theta$  and  $E_\phi$  at broadside and (b) AR responses at broadside.

### III. WIDEBAND CP PATCH ANTENNA WITH TWO AR MINIMA

To further improve the AR bandwidth, the third patch is coupled with the former two patches to introduce the second AR minimum. The wideband CP triangle patch antenna II with detailed dimensions is proposed as shown in Fig. 8. Each patch element has the same dimension, and they are printed on the 0.813 mm-thick dielectric substrate Rogers4003 ( $\epsilon_r = 3.55$ ,  $\tan\delta = 0.003$ ). Three isosceles right-triangular patches are positioned sequentially along a counter-clockwise path to be orthogonal with each other. All of them are closely placed to be strongly coupled with each element by fringing fields. There is also different gap distance between two adjacent elements. To further miniaturize the overall size, each patch is loaded with a different number of shorting pins. Thanks to the constructed short circuit boundary, this enables the patch to operate in quarter wavelength mode.

#### A. Characteristic mode analysis and design of three coupled triangular patches

Characteristic mode analysis is conducted to reveal the working principle of the proposed wideband CP antenna shown in Fig. 8. The substrate and ground plane

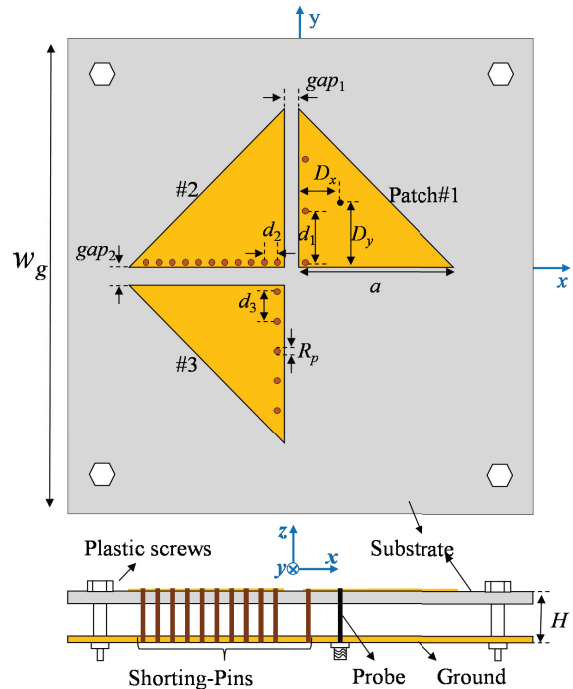


Fig. 8. Geometry of the proposed wideband CP patch antenna II. Dimensions are  $W_g = 120$ ,  $a = 42.5$ ,  $gap_1 = 2.6$ ,  $gap_2 = 3.5$ ,  $D_x = 8$ ,  $D_y = 16$ ,  $d_1 = 13.43$ ,  $d_2 = 4.03$ ,  $d_3 = 3.65$ ,  $R_p = 1.2$ ,  $H = 8.813$  (unit: mm), pin number  $N_{p1} = 3$ ,  $N_{p2} = 10$ ,  $N_{p3} = 5$ .

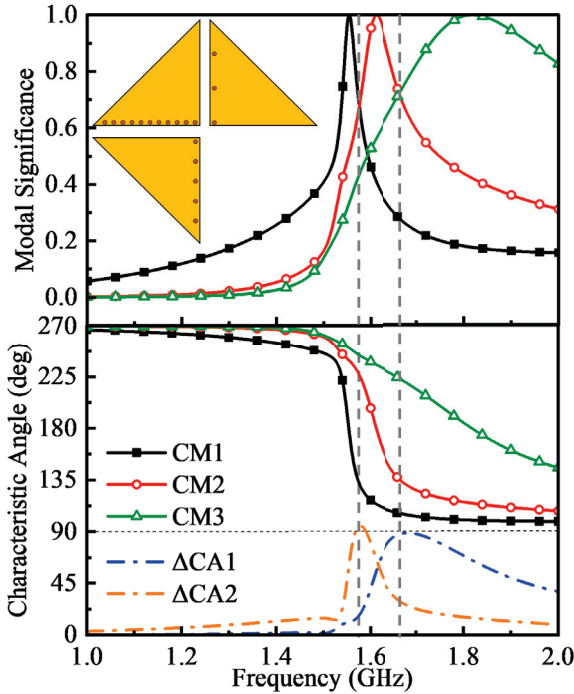


Fig. 9. MS and CA of CP patch antenna II.

are set infinite in the multilayer solver of CST. In Fig. 9, modal significance and characteristic angle show that there are three potential CMs in the working band for antenna II. Three modes respectively resonate at 1.554, 1.612, and 1.82 GHz. Hence, they can be recognized as two pairs of adjacent modes (CM1 and CM2, CM2 and CM3). It can be found that there is a  $90^\circ$  phase difference and equal MS occurring at 1.575 and 1.663 GHz. Meanwhile, the phase of CM1 delays behind CM2, and that of CM2 delays behind CM3. Thanks to the same phase delay between two pairs of adjacent modes, the two pairs of modes can produce the same sense of CP waves to enhance the CP bandwidth.

Figure 10 shows the associated characteristic currents and modal radiation patterns of the CMs at their resonant frequencies. The currents of each two adjacent modes are orthogonal to each other. The total equivalent surface currents of CM1 and CM3 are in opposite directions, and both are orthogonal to that of CM2. Besides, all the CMs can generate broadside radiation patterns. To excite the three CMs, a coaxial probe is placed beneath the patch #1, where the current magnitude of each CMs is almost the same.

In the previous section, the relationship between AR responses and different gap dimensions as well as pin numbers was discussed. It is found that they both can affect the magnitude and the phase difference of the CMs to some extent. Considering that the probe posi-

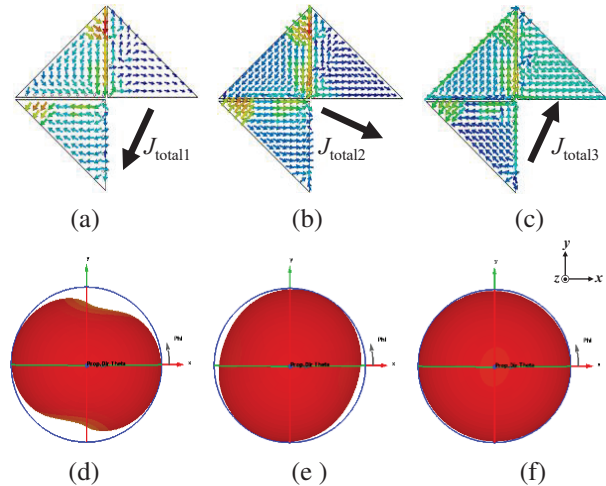


Fig. 10. Characteristic currents and modal radiation patterns of the antenna II. (a) and (d) CM1 at 1.554GHz. (b) and (e) CM2 at 1.612 GHz. (c) and (f) CM3 at 1.8GHz.

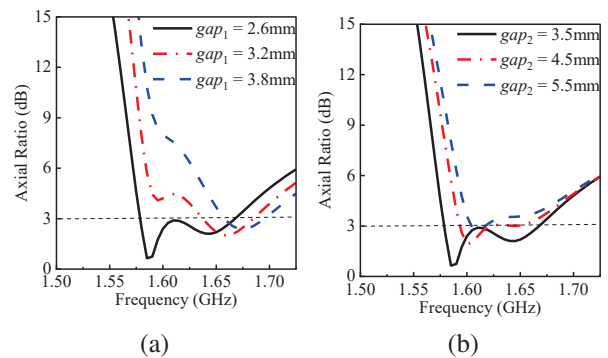


Fig. 11. Simulated AR responses of antenna II with respect to different coupling gap widths of (a)  $gap_1$  and (b)  $gap_2$ .

tion is selected on patch #1, the pin numbers on it ( $N_{p1}$ ) should not be too large because the input impedance will become too low to be matched. Thus, it is suggested to first determine the pin numbers on each patch in the design. After that, the parametric analysis is conducted on the gap distance ( $gap_1$  and  $gap_2$ ).

In this section, a compact and miniaturized wide-band CP antenna is proposed where two AR minima are introduced to broaden AR bandwidth. When  $gap_1$  is equal to 2.6 mm and  $gap_2$  is equal to 3.5 mm, the best CP performance can be realized. On the one hand, the first AR minimum is sensitive to the value of  $gap_1$  as shown in Fig. 11 (a). When  $gap_1$  varies from 2.6 to 3.8 mm, the first AR minimum tends to deteriorate at a high value of 7.9 dB. On the other hand, the second AR minimum point is sensitive to the variations in  $gap_2$ . When  $gap_2$  reaches 5.5 mm, the second AR minimum tends

to reach 3.5 dB. Hence it can also affect the CP performance. The best CP performance will be achieved if the coupling gaps are further optimized.

**B. Simulated and measured results**

To verify the validity of the proposed wideband CP patch antenna, the prototype of the antenna is simulated, fabricated, and tested. The S-parameter and radiation patterns are measured by the R&S ZVA-40 vector network analyzer and the near-field chamber, respectively.

Figure 12 shows the simulated and measured broad-side AR and left-handed circular polarized (LHCP) gain of the proposed antenna. Right-handed CP can also be realized if the probe is soldered at the second patch. The measured AR data matches well with the simulated one. The measured 3 dB-AR bandwidth is from 1.58 to 1.67 GHz (5.5%), and the simulated one is from 1.58 to 1.665 GHz (5.2%). The measured LHCP gain at a higher frequency is slightly lower than the simulated value because the real material loss is higher than the simulated value. The average LHCP gain of the measured and simulated are approximately 5.05 and 5.7 dBic, respectively. The simulated and measured reflection coefficients and efficiencies are also depicted in Fig. 12. The simulated and measured -10 dB matching bandwidths are both from 1.58 to 1.665 GHz (5.2%). The measured efficiency is slightly lower than the simulated one at the higher frequency, which may be because that the  $\tan\delta$  of the fabricated material is higher than the simulated setting one.

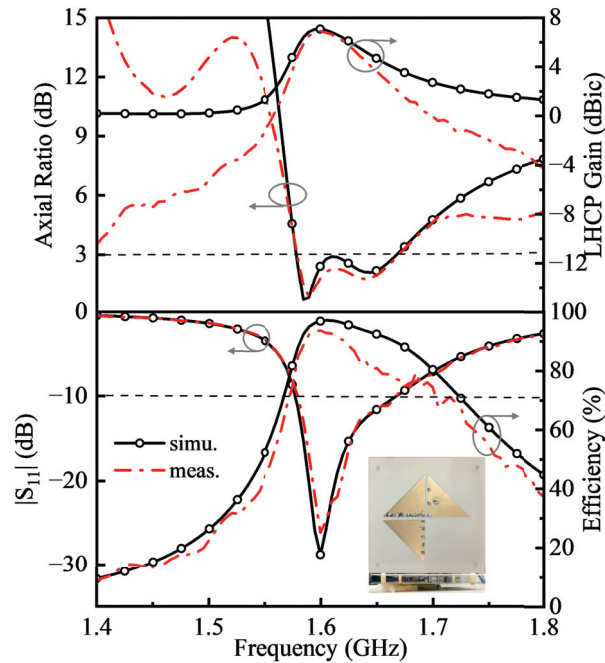


Fig. 12. Measured and simulated ARs, LHCP gains, S-parameters, and efficiency of antenna II.

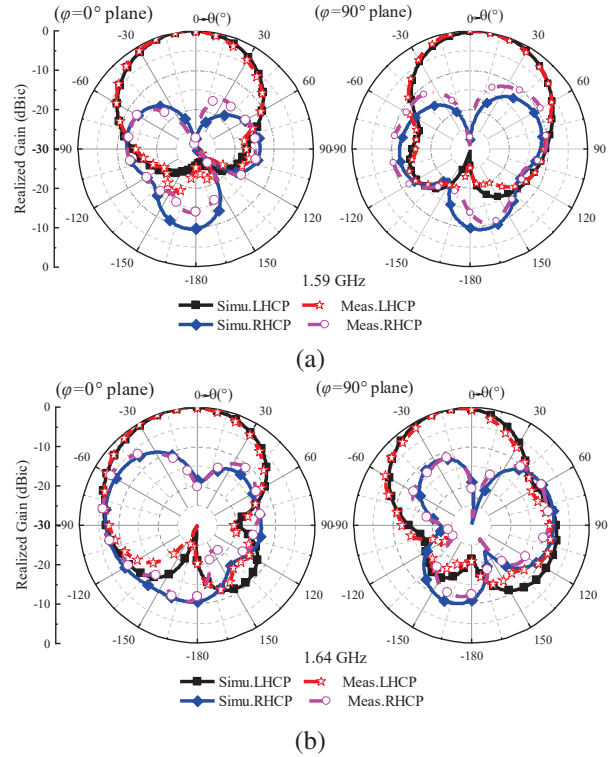


Fig. 13. Measured and simulated radiation patterns of Antenna II: (a) 1.59 GHz and (b) 1.64 GHz.

Figure 13 shows the simulated and measured radiation patterns at two AR minima, 1.59 and 1.64 GHz. At broadside, the LHCP high cross-polarization ratios are achieved, which are up to 27 dB and 18 dB at 1.59 GHz and 1.64 GHz, respectively. The maximum beam direction at higher frequencies is slightly tilted, and the cross-polarization rises with increased theta angle because of the current asymmetry of the three modes.

**IV. CONCLUSION**

In this paper, a miniaturized wideband CP antenna has been proposed based on coupled triangular patch elements. Initially, two perpendicular patch radiators are closely spaced to be coupled with each other. Two rows of shorting pins are inserted, and the patch can operate at quarter-wavelength modes. Hence, the shorting pins and antenna arrangement contribute to antenna miniaturization. By means of CMA, we can find that gap dimension and pins numbers are key parameters for manipulating the phase difference between CMs and generating a minimum AR value. Subsequently, the third patch is introduced, and a widened bandwidth with two AR minima is achieved by allocating its three CMs. The AR bandwidth is enhanced up to 5.2% in a small overall size of  $0.34\lambda_0 \times 0.33\lambda_0 \times 0.046\lambda_0$ . Hence, the proposed CP antenna will be a good candidate in modern wireless

communication systems to meet miniaturized and wide-band requirements.

### ACKNOWLEDGMENT

This work was supported in part by the Guangdong Provincial Department of Science and Technology, China, under Project No. 2020B1212030002, in part by the Shenzhen Science and Technology Innovation Commission, China, under Construction and Operation Project of Guangdong Provincial Key Laboratory and Guangdong-Hong Kong-Macau Joint Laboratory and Projects (No. JCYJ20190808115411853, No. CJGJZD2022051714240411, and No. KQTD20180412181337494), in part by the Postgraduate Education Branch of the China Education Society of Electronics, and in part by the Guangdong Provincial Department of Education, China, under the Innovation Team Project No. 2020KCXTD004.

### REFERENCES

- [1] S. Gao, Q. Luo, and F. Zhu, *Circularly Polarized Antennas*. Hoboken, NJ, USA: Wiley-IEEE Press, Nov. 2013.
- [2] K. L. Wong and T. W. Chiou, "Broad-band single-patch circularly polarized microstrip antenna with dual capacitively coupled feeds," *IEEE Trans. Antennas Propagat.*, vol. 49, no. 1, pp. 41-44, Jan. 2001.
- [3] Q.-S. Wu, X. Zhang, and L. Zhu, "A wideband circularly polarized patch antenna with enhanced axial ratio bandwidth via co-design of feeding network," *IEEE Trans. Antennas Propagat.*, vol. 66, no. 10, pp. 4996-5003, Oct. 2018.
- [4] Q. S. Wu, X. Zhang, and L. Zhu, "A feeding technique for wideband CP patch antenna based on 90 degrees phase difference between tapped line and parallel coupled line," *IEEE Trans. Antennas Propagat.*, vol. 18, no. 7, pp. 1468-1471, July 2019.
- [5] Y. J. Hu, W. P. Ding, and W. Q. Cao, "Broadband circularly polarized microstrip antenna array using sequentially rotated technique," *IEEE Antennas Wireless Propagat. Lett.*, vol. 10, pp. 1358-1361, 2011.
- [6] Y. Li, Z. J. Zhang, and Z. H. Feng, "A sequential-phase feed using a circularly polarized shorted loop structure," *IEEE Trans. Antennas Propagat.*, vol. 61, no. 3, pp. 1443-1447, Mar. 2013.
- [7] C. J. Deng, Y. Li, Z. J. Zhang, and Z. H. Feng, "A wideband sequential-phase fed circularly polarized patch array," *IEEE Trans. Antennas Propagat.*, vol. 62, no. 7, pp. 3890-3893, July 2014.
- [8] B. P. Kumar, D. Guha, and C. Kumar, "Reduction of beam squinting and cross-polarized fields in a wideband CP element," *IEEE Antennas Wireless Propagat. Lett.*, vol. 19, no. 3, pp. 418-422, Mar. 2020.
- [9] J. M. Kovitz and Y. Rahmat-Samii, "Using thick substrates and capacitive probe compensation to enhance the bandwidth of traditional CP patch antennas," *IEEE Trans. Antennas Propagat.*, vol. 62, no. 10, pp. 4970-4979, Oct. 2014.
- [10] A. Khidre, K. F. Lee, F. Yang, and A. Z. Elsherbeni, "Circular polarization reconfigurable wideband E-shaped patch antenna for wireless applications," *IEEE Trans. Antennas Propagat.*, vol. 61, no. 2, pp. 960-964, Feb. 2013.
- [11] J. Yin, Q. Wu, C. Yu, H. Wang, and W. Hong, "Broadband symmetrical E-shaped patch antenna with multimode resonance for 5G millimeter-wave applications," *IEEE Trans. Antennas Propagat.*, vol. 67, no. 7, pp. 4474-4483, July 2019.
- [12] K. Y. Lam, K. M. Luk, K. F. Lee, H. Wong, and K. B. Ng, "Small circularly polarized U-slot wideband patch antenna," *IEEE Antennas Wireless Propagat. Lett.*, vol. 10, pp. 87-90, 2011.
- [13] S. S. Yang, K.-F. Lee, A. A. Kishk, and K.-M. Luk, "Design and study of wideband single feed circularly polarized microstrip antennas," *Prog. Electromagn. Res.*, vol. 80, pp. 45-61, Jan. 2008.
- [14] J. Wu, X. Ren, Z. Wang, and Y. Yin, "Broadband circularly polarized antenna with L-shaped strip feeding and shorting-pin loading," *IEEE Antennas Wireless Propagat. Lett.*, vol. 13, pp. 1733-1736, 2014.
- [15] L.-L. Qiu, L. Zhu, and Y. Xu, "Wideband low-profile circularly polarized patch antenna using 90° modified Schiffman phase shifter and meandering microstrip feed," *IEEE Trans. Antennas Propagat.*, vol. 68, no. 7, pp. 5680-5685, July 2020.
- [16] Q. W. Lin, H. Wong, X. Y. Zhang, and H. W. Lai, "Printed meandering probe-fed circularly polarized patch antenna with wide bandwidth," *IEEE Antennas Wireless Propagat. Lett.*, vol. 13, pp. 654-657, 2014.
- [17] S.-X. Ta and I. Park, "Low-profile broadband circularly polarized patch antenna using metasurface," *IEEE Trans. Antennas Propagat.*, vol. 63, no. 12, pp. 5929-5934, Dec. 2015.
- [18] M.-C. Tang, X. Chen, M. Li, and R. W. Ziolkowski, "A bandwidth-enhanced, compact, single-feed, low-profile, multilayered, circularly polarized patch antenna," *IEEE Antennas Wireless Propagat. Lett.*, vol. 16, pp. 2258-2261, 2017.
- [19] G. Kumar and K. Gupta, "Broad-band microstrip antennas using additional resonators gap-coupled

- to the radiating edges,” *IEEE Trans. Antennas Propagat.*, vol. 32, no. 12, pp. 1375-1379, Dec. 1984.
- [20] K. Ding, C. Gao, D. Qu, and Q. Yin, “Compact broadband circularly polarized antenna with parasitic patches,” *IEEE Trans. Antennas Propagat.*, vol. 65, no. 9, pp. 4854-4857, Sep. 2017.
- [21] J.-F. Lin and Q.-X. Chu, “Enhancing bandwidth of CP microstrip antenna by using parasitic patches in annular sector shapes to control electric field components,” *IEEE Antennas Wireless Propagat. Lett.*, vol. 17, pp. 924-927, 2018.
- [22] Q.-S. Wu, X.-Y. Tang, X. Zhang, L. Zhu, G. Zhang, and C.-B. Guo, “Circularly-polarized patch antennas with enhanced bandwidth based on capacitively coupled orthogonal patch radiators,” *IEEE Open J. Antennas Propagat.*, vol. 4, pp. 472-483, 2023.
- [23] Y.-H. Xu, L. Zhu, N.-W. Liu, and L.-L. Qiu, “An inductively coupled CP slot antenna based on intrinsic 90° phase difference and its flexible application in wideband CP radiation,” *IEEE Trans. Antennas Propagat.*, vol. 71, no. 2, pp. 1204-1215, Feb. 2023.
- [24] N.-W. Liu, L. Zhu, Z.-X. Liu, G. Fu, and Y. Liu, “Design approach of a single circularly polarized patch antenna with enhanced AR-bandwidth under triple-mode resonance,” *IEEE Trans. Antennas Propagat.*, vol. 68, no. 8, pp. 5827-5834, Aug. 2020.
- [25] J. Zeng, X. Liang, L. He, F. Guan, F. H. Lin, and J. Zi, “Single-fed triple-mode wideband circularly polarized microstrip antennas using characteristic mode analysis,” *IEEE Trans. Antennas Propagat.*, vol. 70, no. 2, pp. 846-855, Feb. 2022.
- [26] R. F. Harrington and J. R. Mautz, “Computation of characteristic modes for conducting bodies,” *IEEE Trans. Antennas Propagat.*, vol. AP-19, no. 5, pp. 629-639, Sep. 1971.
- [27] Y. Chen and C.-F. Wang, *Characteristic Modes: Theory and Applications in Antenna Engineering*, 1st ed., pp. 1-142, Hoboken, NJ, USA: Wiley, 2015.
- [28] J.-F. Lin and L. Zhu, “Low-profile high-directivity circularly-polarized differential-fed patch antenna with characteristic modes analysis,” *IEEE Trans. Antennas Propagat.*, vol. 69, no. 2, pp. 723-733, Feb. 2021.
- [29] X. Zhang, Q. Y. Zeng, Z. P. Zhong, Q. S. Wu, L. Zhu, and T. Yuan, “Analysis and design of stable-performance circularly polarized antennas based on

coupled radiators for smart watches,” *IEEE Trans. Antennas Propagat.*, vol. 70, no. 7, pp. 5312-5323, July 2022.



**Tian-Long Yang** was born in Zhanjiang, Guangdong, China. He received the B.Eng. degree in electronic and information engineering from Shenzhen University, Shenzhen, China, in 2021. He is currently pursuing the M.Eng. degree in communication engineering with Shenzhen University, Shenzhen, China.

His current research interests include circularly polarized antennas and terminal antennas.



**Xiao Zhang** (S'15-M'18) was born in Gaozhou, Guangdong, China. He received the B.Eng. degree in information engineering and the M.Eng. degree in communication and information systems from the South China University of Technology, Guangzhou, China, in 2011 and 2014, respectively, and the Ph.D. degree in electrical and computer engineering from University of Macau, Macau, SAR, China, in 2017.

From September 2012 to August 2014, he was a research assistant with Comba Telecom Systems Limited, Guangzhou, China. From January 2018 to March 2018, he was a research fellow with the Antenna and Electromagnetic-Wave Laboratory in University of Macau, Macau, SAR, China. In 2018, he joined the College of Electronics and Information Engineering, Shenzhen University, Shenzhen, China, where he is currently an associate professor. His research interests include high-gain antennas, wideband antennas, circularly-polarized antennas, terminal antennas, filtering antennas, reflectarray, and characteristic mode analysis.

Dr. Zhang was the recipient of the Scientific and Technological R&D Award for Postgraduates of Macau in 2018. He was recognized as the Shenzhen Overseas High Caliber Personnel Level C in 2018. He was recognized as a Top 2% Scientist in 2019 and 2022 by Elsevier. He also serves as a reviewer for several journals, including the *IEEE Transactions on Antennas and Propagation* and the *IEEE Antennas and Wireless Propagation Letters*.



**Qiong-Sen Wu** received the B.Eng. degree in information engineering and the M.Eng. degree in electromagnetism and microwave engineering from South China University of Technology, Guangzhou, China, in 2011 and 2014, respectively, and the Ph.D. degree in electrical and computer engineering from the University of Macau, Macau, SAR, China, in 2018.

He joined the Antenna and Electromagnetic-Wave Laboratory in University of Macau, Macau, SAR, China, as a research fellow in May 2018. He is currently an associate professor with the School of Integrated Circuits, Guangdong University of Technology. His current research interests include microwave circuits and planar antennas with improved functionalities. He also serves as a reviewer for several journals, including the *IEEE Transactions on Antennas and Propagation* and the *IEEE Transactions on Microwave Theory and Techniques*.



**Tao Yuan** (M'19) received the B.E. degree in electronic engineering and the M.E. degree in signal and information processing at Xidian University, Xi'an, Shaanxi, China, in 1999 and 2003, respectively, and the Ph.D. degree in electrical and computer engineering at National University of Singapore, Singapore, in 2009.

He was a visiting scholar at University of Houston (2007-2008). He is now a distinguished professor (2016-till now) with the College of Electronics and Information Engineering at Shenzhen University, Shenzhen, Guangdong, China. He is the director of the Guangdong Provincial Mobile Terminal Microwave and Millimeter-Wave Antenna Engineering Research Center and the deputy director of the Guangdong-Hong Kong Joint Laboratory for Big Data Imaging and Communication. He is a visiting professor (2021-till now) at Chongqing University, China, and an adjunct professor (2021-till now) at Fudan University, China. He is leading a group of over 70 members performing fundamental and application studies in the areas of RF/microwave/millimeter-wave frontend devices, antennas, ICs, and advanced manufacturing techniques for microwaves and microelectronics. He has Pled/co-Pled over 20 governmental and entrepreneurial research projects on 5G MIMO antennas (arrays), transmission lines, and packaged antennas for smart IoT/mobile terminals. His current research interests include design and implementation

of novel RF frontend chips/modules and integrated devices/antennas/circuits for 5G/6G applications. He has advised over 40 graduate students and has authored/co-authored over 150 international journal and conference publications. He holds over 100 licensed CN patents. He has co-authored 2 books: *Antenna Design for 5G Mobile Terminals* (Posts & Telecom Press, 2021) and *Practical Design and Development of FPGA—Based on Xilinx and Verilog HDL* (Publishing House of Electronics Industry, 2023).

Dr. Yuan is a member of the IEEE Antennas and Propagation Society, IEEE Microwave Theory and Techniques Society, and the China Communications Standards Association. He is a senior member of the Chinese Institute of Electronics (CIE) and the China Institute of Communications (CIC). He serves as a reviewer for several international journals and conferences and serves as a guest editor for *Coatings*. He is the organizing committee member of APMC2020, Mar-For (2021, 2022) (TPC Member), and CSRSWTC2021 (General Chair). He serves as a consultant for several research institutions and ICT companies in China. He received numerous teaching, entrepreneurial, and talent awards in China. He is the recipient of the Outstanding Individual Award (2018), the Outstanding Graduate Student Advisor (2021), the Excellent Undergraduate Thesis Instructor (2022), and the Undergraduate Teaching Outstanding Contribution Award (2022) from Shenzhen University and the co-recipient of the CIC Science and Technology Second Place Award (2020) and the Excellent Teaching Management Team of Tencent Team Award (2022). His students and group members have received over 150 scholarships/awards in China and international conferences, including the CSRSWTC2021 Best Paper Award and the IEEE RWW2022 student paper competition finalist.

# A Low-profile Dual-band Dual-polarization Co-aperture Array Antenna with High Isolation

Liang-Xin Xia, Qi lei Zhou, Neng-Wu Liu\*, and Guang Fu

National Key Laboratory of Antennas and Microwave Technology  
Xidian University, Xian, 710075, China

LiangxinXia@stu.xidian.edu.cn, 20021110068@stu.xidian.edu.cn,  
nwliu@xidian.edu.cn, gfu@mail.xidian.edu.cn

**Abstract** – This paper proposes a low-profile high-isolation dual-polarization array antenna operating in the L/S band. The radiating unit of the array antenna adopts U-shaped bending dipoles to realize the staggered arrangement of high- and low-band units, and is connected to the feeding network by a coaxial cable. To achieve the non-influence of high-band and low-band feed networks, multi-layer printing technology is used and grooves are etched on the metal plate. In order to reduce the coupling of the high- and low-band dipoles at low frequency, a bandpass filter is added to the high-band feed network, which greatly improves the isolation at low-frequency. The measured results show that the impedance bandwidth of the array is 4.5% (0.971-1.015 GHz) and 7.5% (1.89-2.04 GHz), with gains of 15 and 19 dBi at 1 GHz and 2 GHz, respectively. And the isolation between the dual-polarized ports more than 50 dB and 35 dB was achieved at 1 GHz and 2 GHz, respectively. The proposed array will have practical value in L/S band full-duplex wireless communication systems.

**Index Terms** – dual-polarization, high-isolation, multi-layer network, U-shaped bending dipoles.

## I. INTRODUCTION

In recent years, a variety of antenna technologies have been developed in the direction of easy integration, multi-band [1–2], multi-polarization [3–4] and low profile to meet the requirements of modern communication technology. Among them, the dual-polarization technology and the dual-band technology can not only increase the capacity of the communication system but also realize various radiation functions, such as transceiver integration [5–6]. The arrangement of multiple antenna units with different polarizations and bands in the same aperture greatly reduces the size of the antenna array.

Some multi-band and multi-polarization co-aperture array antennas have been proposed by researchers. Initially, a single antenna [7–10] or combination antenna

[11–12] with dual-band and dual-polarization characteristics is used as an element to construct the array to improve the channel capacity of the array antenna. This antenna is usually connected to a broadband or dual-band feed network. However, it usually results in low aperture efficiency and low gain in the high-frequency band, and it cannot effectively use the array aperture. To improve the aperture efficiency at high frequency, the researchers have interspersed the high-band units in the low-band array to increase the number of units in the high-frequency arrays [13–16]. The authors in [16] propose a co-aperture antenna with L/S band placed in the same layer. To realize the dual-band co-aperture antenna, the L-band dipole is bent, and the S-band dipole is placed in the same layer in the empty part of the L-band dipole, taking advantage of the small physical size occupied by the bending dipole. Furthermore, different frequency antennas can also be placed on different layers [17–20]. In [20], to realize the dual-band antenna co-aperture placement in different layers, the antenna etches the weak electric field area in the middle of the upper C-band patch to make room for the normal radiation of the lower X-band patch antenna. In addition to modifying the low-frequency antenna to realize the displacement of the horizontal space and the vertical space, the dual-band co-aperture can be obtained by using the antenna with small lateral occupation area. For example, the author in [21] adopted Vivaldi and dipole antennas to realize the co-aperture placement of arrays with different frequencies of S/X, but the profile is higher.

In this paper, a multi-layer feeding network with filter is designed to solve the feeding problem of a dual-frequency dual-polarization array based on reference [16]. It is easy to fabricate by reasonably arranging the HB and LB feed networks, and it achieves high isolation between the two ports. Through simulation and measurement, it is found that the antenna achieves the impedance bandwidths of 4.5% and 7.5% and gains of 15 and 19 dBi at 1 GHz and 2 GHz, respectively. The isolation between the two ports reaches 35 dB.

## II. ANTENNA DESIGN

The overall configuration of the array antenna is shown in Fig. 1. The low-profile dual-band and dual-polarized co-aperture array antenna consists of a staggered arrangement of high-band and low-band dipoles and a multi-layer power divider network. The overall structure of the antenna is divided into antenna radiation layer, coaxial cable, low-band feed network, and high-band feed network from top to bottom.

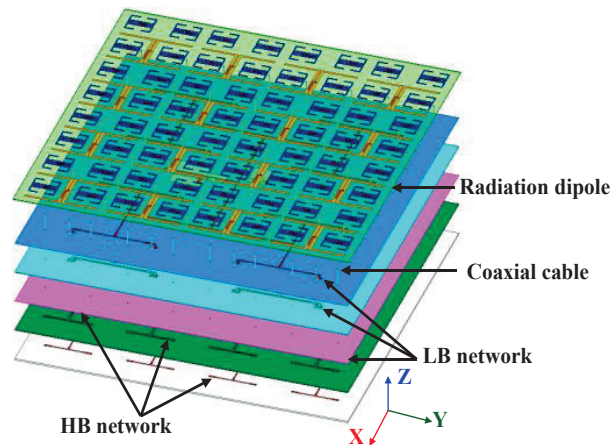


Fig. 1. Configuration of the dual-band and dual-polarization array antenna.

The hierarchical structure of the entire array antenna is shown in Fig. 2. The radiation layer of the antenna is printed on the bottom layer of FR4 with a thickness of 1 mm. The reasonable arrangement of the high- and low-band dipoles is realized by using the gap of the low-band bending dipole and the miniaturization of the high-band bending dipole, and they are connected to the high- and low-band feed network of the ground through the coaxial cable. The feed network is printed on a two-layer dielectric substrate F4B ( $\epsilon_r=2.1$ ) with a thickness of 1 mm by using multi-layer dielectric printing technology. The

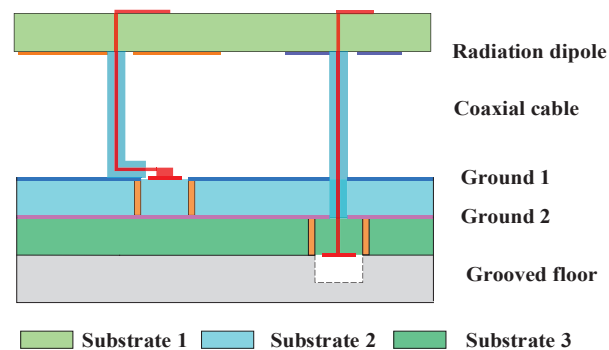


Fig. 2. Schematic diagram of multilayer stacked structure.

low-frequency feed network adopts the transmission line form of CPW to realize a 1:16 power division network. The high-band feed network is located in the lower layer of the low-band feed network, and the stripline power division feed network is realized by etching slots on the metal ground. In addition, the high-band network is also cascaded with a bandpass filter to achieve high isolation between the two ports at low frequency.

### A. Analysis of antenna unit

The array unit uses U-shaped bend dipoles. The feed structure and relative positions of the high- and low-band dipoles are shown in Fig. 3 and Fig. 4. The coupling microstrip line (MPL) is used to achieve a wider operating bandwidth, and the coaxial cable is used to connect the dipole unit to the feed network. To validate the antenna unit design, the dual-band array antenna unit is simulated. The simulated S-parameters and radiation patterns are shown in Figs. 5 and 6. Both work well, but the isolation of the two ports is slightly worse at low frequency.

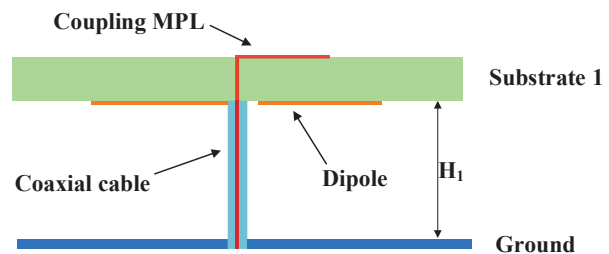


Fig. 3. The configuration of a dual-band coaxial feed dipole (side view).

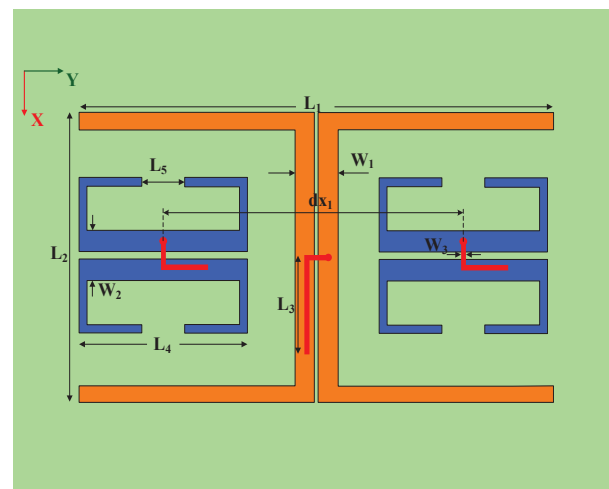


Fig. 4. The configuration of the dual-polarized dipoles (top view).

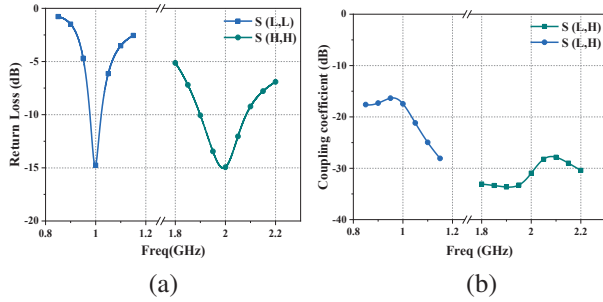


Fig. 5. Simulated S-parameters of the dual-band element: (a) Return loss and (b) coupling coefficient between the dual-polarized ports.

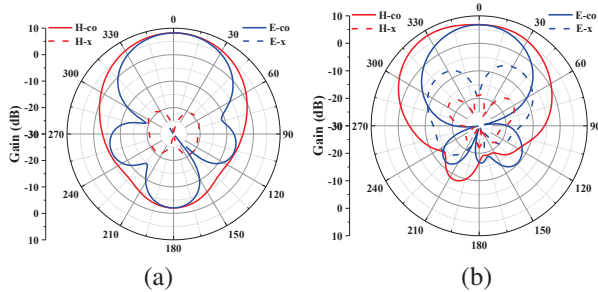


Fig. 6. The radiation patterns of the dual-band element: (a) LB element @ 1 GHz and (b) HB element @ 2 GHz.

**B. Analysis of dual-band network with filter**

The array antenna usually prints the power division feed network on the dielectric substrate, but the high-band and low-band feed networks have the problem of overlapping or crossing transmission lines on the same layer. As shown in Fig. 7, a multi-layer feed network is proposed in this paper. The high-band and low-band feed network is realized by using two layers of dielectric substrates and a metal plate with etched grooves.

To avoid interference between the upper and lower layers, the high-band network is placed in the lower layer and is designed in the form of striplines, and the low-band network is placed on the upper layer using CPW. The two sides of the stripline and CPW realize the potential of the upper and lower ground through metal holes to balance and eliminate resonance, which is represented by a metal wall in Fig. 7. In addition, in order to solve the problem of strong coupling between high-band and low-band dipoles at low frequencies, the bandpass filter and the high-band feed network are cascaded to achieve high isolation between two ports. The low-band network is connected to an open branch at the main port to adjust the impedance of the low-band array to avoid frequency offset problems caused by manufacturing.

Based on the principle of T-type equal-amplitude power divider, a dual-band multi-layer feed network

is designed. The key size parameters of the radiating dipoles and the feed network are shown in Table 1.

Table 1: Value of the parameter in the antenna array

Parameter	Value (mm)	Parameter	Value (mm)
H <sub>1</sub>	28	L3	24
H <sub>2</sub>	1	L4	43
W <sub>1</sub>	11	L5	11
W <sub>2</sub>	12	dx1	75
W <sub>3</sub>	1.25	dx2	68
W <sub>4</sub>	550	dx3	136
W <sub>5</sub>	550	dy1	68
L1	131	dy2	136
L2	72		

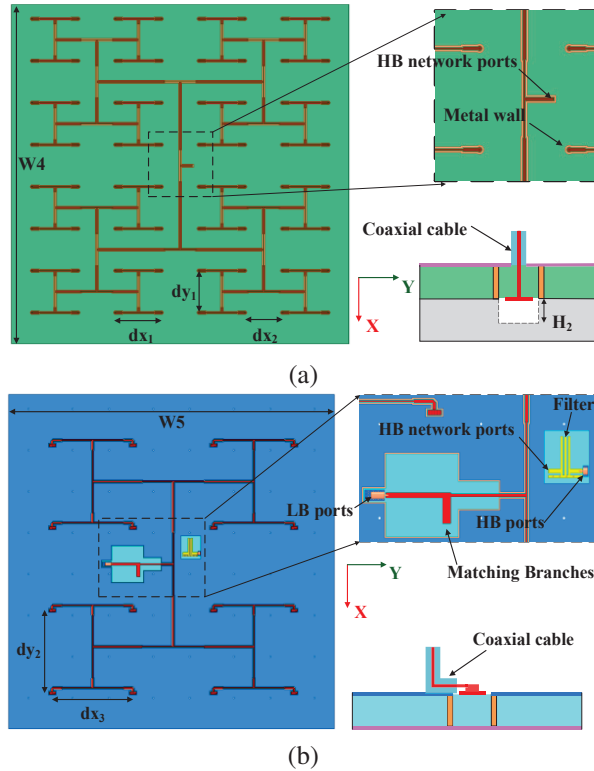


Fig. 7. Schematic diagram of the HB and LB feed network based on T-shape power divider: (a) HB network and (b) LB network.

In order to verify the design of the multi-layer feed network, the high-band and low-band feed networks are simulated and verified. The S-parameters of the network are shown in Fig. 8. According to Fig. 8, the high-band and low-band feed networks achieve good impedance matching in their respective bands, and the bandpass filter also achieves blocking characteristics in the low frequency, finally achieving high isolation between the two ports.

By analyzing the dual-band radiating dipoles and feed network, the low-profile array antenna can achieve higher gain, better impedance matching, and isolation at 1 GHz and 2 GHz.

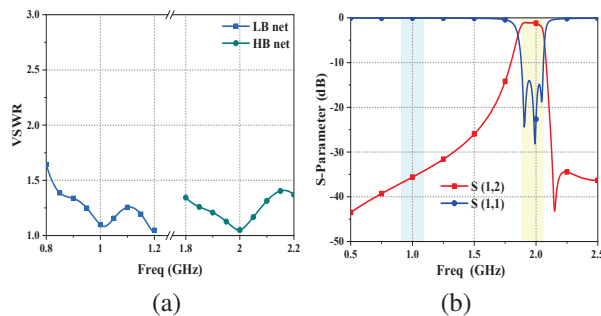


Fig. 8. Simulated results of the feed network and filter: (a) VSWR of the HB and LB feed network and (b) S-parameters of the filter.

### III. RESULTS AND EXPERIMENTAL VALIDATION

In order to verify the above design effectively, the array antenna is simulated and fabricated. The S-parameter of the antenna was measured using a vector network analyzer, and the radiation patterns of the antenna at 1 GHz and 2 GHz are measured in an anechoic chamber.

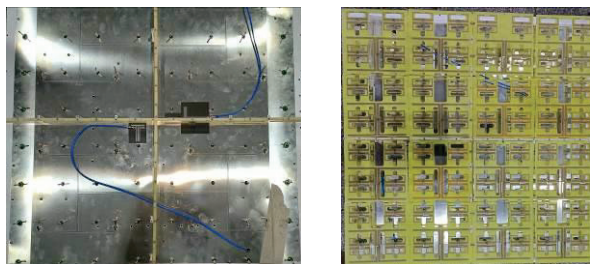


Fig. 9. Photograph of the fabricated network and antenna.

The photographs of the fabricated antenna and the measurement environment are shown in Figs. 9 and 10, respectively.

Firstly, the voltage standing wave ratio (VSWR) of the proposed antenna is measured, and the results are shown in Fig. 11. The simulation results of the two bands are in good agreement with the measured results, but there is a slight deviation in the operating frequency. But the  $VSWR < 2$  can still be satisfied at 1 GHz and 2 GHz. In addition, the results show that the impedance bandwidth of the antenna is 4% (0.971-1.015 GHz) and 7.5% (1.89-2.04 GHz), respectively, which is basically consistent with the simulation.

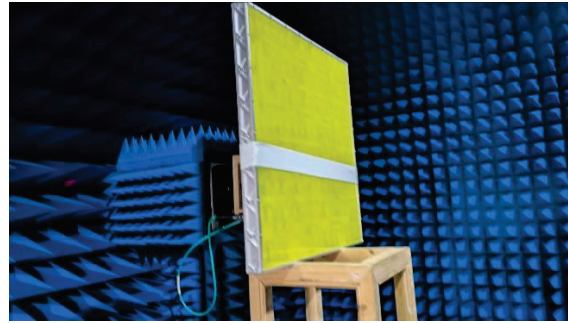


Fig. 10. Photograph of measuring the fabricated antenna.

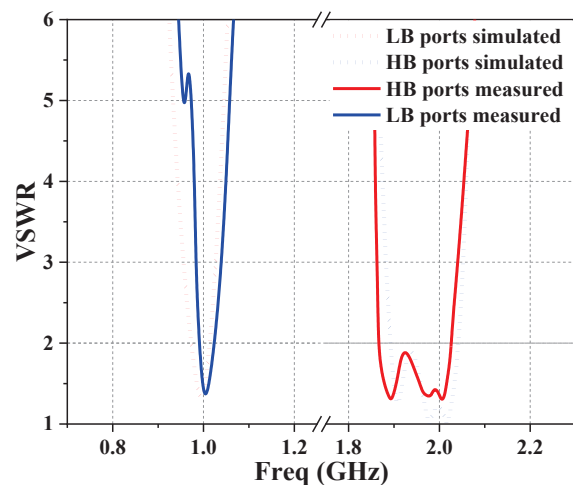


Fig. 11. Simulation and measurement VSWR of the dual-band antenna.

As shown in Fig. 12, the isolation between the dual-polarized ports is more than 50 dB and 35 dB at 1 GHz and 2 GHz, respectively. It shows that the filter has the effect of significantly improving the isolation.

The radiation patterns of the proposed dual-band dual-polarized antenna are shown in Figs. 13 and 14. Among them, they are the radiation patterns of the  $yz$ -plane when the high- and low-band arrays, respectively, are excited. It can be seen that the main beam of the antenna array at low frequency and high frequency is consistent with the simulation, but the measured side lobe level is slightly higher at -11.5 dB, and the measured gain is 15 dB and 19 dB, slightly lower than the simulation 15.5 dB and 19.6 dB. The cross-polarization of the array at high frequency is obviously different from the simulation results. This is mainly because the cross polarization level is high when the antenna unit deviates from the broadside direction, and the installation error causes the dipole plane to tilt slightly, so that the broadside direction of the antenna is not all pointing to  $0^\circ$ , thus increasing the cross polarization level.

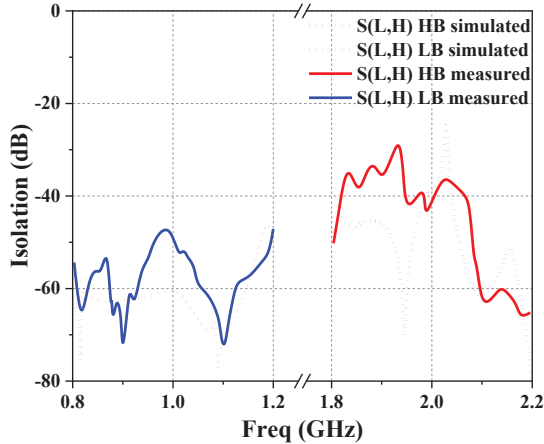


Fig. 12. Simulation and measurement coupling coefficient of the dual-band antenna.

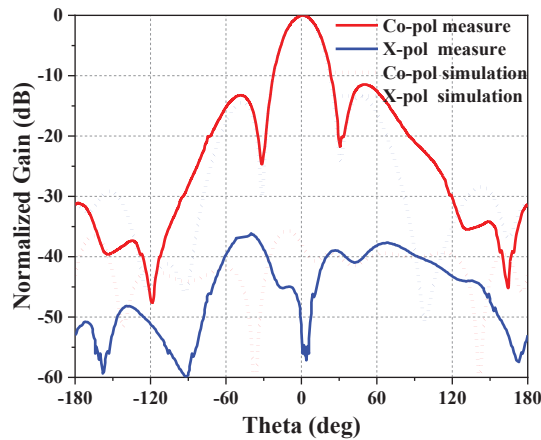


Fig. 13. Simulated and measured pattern of the antenna array @ 1 GHz (yoz).

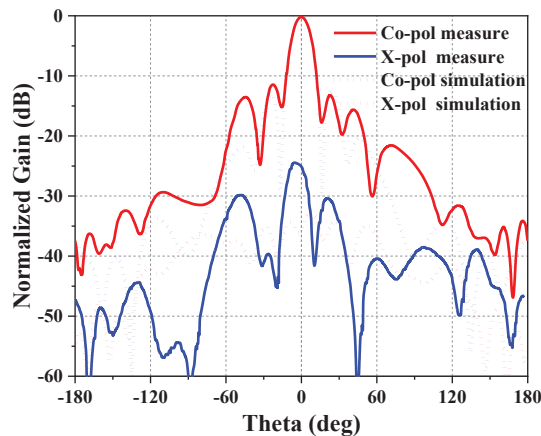


Fig. 14. Simulated and measured pattern of the antenna array @ 2 GHz (yoz).

According to the actual measured gain, it is calculated that the aperture efficiency of the co-aperture array

antenna at low frequency and high frequency is 85% and 54%, respectively. The low aperture efficiency of the high frequency is mainly due to the insertion loss of the filter and power division network.

#### IV. CONCLUSION

In this paper, a low-profile dual-band and dual-polarization co-aperture array antenna with a multi-layer feed network is proposed, in which the antenna elements are printed on the dielectric substrate in a staggered manner, and the feed network is fabricated using multi-layer printing technology to achieve high and low-band network without affecting each other. The array antenna can achieve different polarizations and better isolation at dual frequencies, can also obtain higher gain at the same time, and it has practical value.

#### ACKNOWLEDGMENT

This work is supported by the National Natural Science Foundation of China under General Program (62271364), Key Research and Development Program of Shaanxi (Program No. 2023-GHZD-45) and Fundamental Research Funds for the Central Universities (ZYTS23145). (Corresponding author: Neng-Wu Liu)

#### REFERENCES

- [1] N.-W. Liu, L. Zhu, Z.-X. Liu, and Y. Liu, "Dual-band single-layer microstrip patch antenna with enhanced bandwidth and beamwidth based on reshaped multiresonant modes," *IEEE Trans. Antennas Propag.*, vol. 67, no. 11, pp. 7127-7132, Nov. 2019.
- [2] L. Kong and X. Xu, "A compact dual-band dual-polarized microstrip antenna array for MIMO-SAR applications," *IEEE Trans. Antennas Propag.*, vol. 66, no. 5, pp. 2374-2381, May 2018.
- [3] D. Kim, M. Zhang, J. Hirokawa, and M. Ando, "Design and fabrication of a dual-polarization waveguide slot array antenna with high isolation and high antenna efficiency for the 60 GHz band," *IEEE Trans. Antennas Propag.*, vol. 62, no. 6, pp. 3019-3027, June 2014.
- [4] N.-W. Liu, L. Zhu, X. Zhang, and W.-W. Choi, "A wideband differential-fed dual-polarized microstrip antenna under radiation of dual improved odd-order resonant modes," *IEEE Access*, vol. 5, pp. 23672-23680, 2017.
- [5] J. Hesselbarth, "Dual-linear polarised antenna module with enhanced transmit-receive isolation," *Electronics Letters*, vol. 43, no. 4, pp. 196-198, 2007.
- [6] F. Jia, S. Liao, and Q. Xue, "A dual-band dual-polarized antenna array arrangement and its application for base station antennas," *IEEE Antennas and Wireless Propag. Lett.*, vol. 19, no. 6, pp. 972-976, June 2020.

- [7] M. Ferrando-Rocher, J. I. Herranz-Herruzo, A. Valero-Nogueira, and M. Baquero-Escudero, "Dual-band single-layer slot array antenna fed by K/Ka-band dual-mode resonators in gap waveguide technology," *IEEE Antennas and Wireless Propag.*, vol. 20, no. 3, pp. 416-420, Mar. 2021.
- [8] Z. Wang, G.-X. Zhang, Y. Yin, and J. Wu, "Design of a dual-band high-gain antenna array for WLAN and WiMAX base station," *IEEE Antennas and Wireless Propag.*, vol. 13, pp. 1721-1724, 2014.
- [9] H. Lee, D. Ren, and J. H. Choi, "Dual-band and polarization-flexible CRLH substrate-integrated waveguide resonant antenna," *IEEE Antennas and Wireless Propag.*, vol. 17, no. 8, pp. 1469-1472, Aug. 2018.
- [10] J.-D. Zhang, L. Zhu, N.-W. Liu, and W. Wu, "Dual-band and dual-circularly polarized single-Layer microstrip array based on multiresonant modes," *IEEE Trans. Antennas Propag.*, vol. 65, no. 3, pp. 1428-1433, Mar. 2017.
- [11] J.-D. Zhang, W. Wu, and D.-G. Fang, "Dual-band and dual-circularly polarized shared-aperture array antennas with single-layer substrate," *IEEE Trans. Antennas Propag.*, vol. 64, no. 1, pp. 109-116, Jan. 2016.
- [12] Z. Yang and K. F. Warnick, "Multiband dual-polarization high-efficiency array feed for Ku/reverse-band satellite communications," *IEEE Antennas and Wireless Propag.*, vol. 13, pp. 1325-1328, 2014.
- [13] W. C. Zheng, L. Zhang, Q. X. Li, and Y. Leng, "Dual-band dual-polarized compact bowtie antenna array for anti-interference MIMO WLAN," *IEEE Trans. Antennas Propag.*, vol. 62, no. 1, pp. 237-246, Jan. 2014.
- [14] R. Xiao, M.-C. Tang, Y. Shi, Z.-F. Ding, M. Li, and X. Wei, "Dual-polarized, dual-band, and aperture-shared synthesis method for phased array applications," *IEEE Trans. Antennas Propag.*, vol. 70, no. 6, pp. 4896-4901, June 2022.
- [15] A. I. Sandhu, E. Arnieri, G. Amendola, L. Boccia, E. Meniconi, and V. Ziegler, "Radiating elements for shared aperture Tx/Rx phased arrays at K/Ka band," *IEEE Trans. Antennas Propag.*, vol. 64, no. 6, pp. 2270-2282, June 2016.
- [16] K. Naishadham, R. Li, L. Yang, T. Wu, W. Hunsicker, and M. Tentzeris, "A shared-aperture dual-band planar array with self-similar printed folded dipoles," *IEEE Trans. Antennas Propag.*, vol. 61, no. 2, pp. 606-613, Feb. 2013.
- [17] C. Zhu, G. Xu, A. Ren, W. Wang, Z. Huang, and X. Wu, "A compact dual-band dual-circularly polarized SIW cavity-backed antenna array for millimeter-wave applications," *IEEE Antennas and Wireless Propag. Lett.*, vol. 21, no. 8, pp. 1572-1576, Aug. 2022.
- [18] Z. Chen, T. Xu, J.-F. Li, L. H. Ye, and D.-L. Wu, "Dual-broadband dual-polarized base station antenna array with stable radiation pattern," *IEEE Antennas and Wireless Propag. Lett.*, vol. 22, no. 2, pp. 303-307, Feb. 2023.
- [19] Y. F. Cao, X. Y. Zhang, and Q. Xue, "Compact shared-aperture dual-band dual-polarized array using filtering slot antenna and dual-function metasurface," *IEEE Trans. Antennas Propag.*, vol. 70, no. 2, pp. 1120-1131, Feb. 2022.
- [20] C.-X. Mao, S. Gao, Y. Wang, Q. Luo, and Q.-X. Chu, "A shared-aperture dual-band dual-polarized filtering-antenna-array with improved frequency response," *IEEE Trans. Antennas Propag.*, vol. 65, no. 4, pp. 1836-1844, Apr. 2017.
- [21] G. Kwon, J. Park, D. Kim, and K. C. Hwang, "Optimization of a shared-aperture dual-band transmitting/receiving array antenna for radar applications," *IEEE Trans. Antennas Propag.*, vol. 65, no. 12, pp. 7038-7051, Dec. 2017.



**Liang-Xin Xia** was born in Anhui, China, in February 1997. He received the B.S. degree in electronic information technology from Xidian University, Xi'an, China, in 2019, where he is currently pursuing the Ph.D. degree. His current research interests include

Fabry-Perot cavity antennas, wide-beam antennas, and beam-shaped array antennas.



**Qi lei Zhou** was born in Shaanxi, China, in September 1997. He received the B.S. degree in electronic information technology from Xidian University, Xi'an, China, in 2019, where he is currently pursuing the Ph.D. degree. His current research interests include broadband

miniaturized circularly polarized antennas and millimeter wave phased arrays.



**Neng-Wu Liu** was born in Changde, China. Since 2018, he has been an associate professor with Xidian University. His current research interests include the designs of antenna theory, low-profile antennas, multimode antennas, wideband antennas, patch antennas, filtering antennas, and phased arrays.



**Guang Fu** received the B.S. and M.S. degrees in electromagnetic field and microwave technology from Xidian University, Xi'an, China, in 1984 and 1991, respectively. He became a professor with Xidian University, in 2001. His current research interests include theory and engineering of antennas and antenna arrays.

# A 4-Element UWB MIMO Antenna System with High Isolation Performance

Tongyu Ding<sup>1</sup>, Haobin Yang<sup>1</sup>, Zhiwei Chen<sup>1</sup>, Zhen Lin<sup>2</sup>, Bin He<sup>2</sup>, and Chong-Zhi Han<sup>1\*</sup>

<sup>1</sup>School of Ocean Information Engineering  
Jimei University, Xiamen, 361021, China  
tyding@jmu.edu.cn, h.yang@jmu.edu.cn, chongzhi\_han@jmu.edu.cn

<sup>2</sup>China Mobile Group Device Co., Ltd  
Shenzhen, 518067, China

**Abstract** – This paper proposes a 4-element multiple-input multiple-output (MIMO) antenna system, which is intended for ultra-wideband (UWB) applications. The antenna has a dimension of  $92 \times 70 \times 1.6 \text{ mm}^3$ . It achieves element isolation via the defected ground structure (DGS) and symmetric E-shaped branch structures design. The realized operating bandwidth is from 3 GHz to 18 GHz, with 15 dB isolation within the whole wide band. The envelope correlation coefficient (ECC) is less than 0.01 with diversity gain (DG) greater than 9.95. The prototype is fabricated and measured to verify its potential applications for UWB MIMO communication.

**Index Terms** – DG, ECC, isolation, MIMO, UWB.

## I. INTRODUCTION

The ultra-wideband (UWB) technology has been highly committed for decades due to low power consumption and high-speed data transmission [1–3], making it continuously promising technology in versatile future fields including indoor positioning [4], radar detection [5], and wireless communications [6–8]. As the demand for UWB applications increases, research and developments of UWB technologies and devices have attracted considerable attention.

More recently, multiple input multiple output (MIMO) technology has become one key technology of future mobile and wireless communication systems. It is worth noting that MIMO significantly improves the spectral efficiency of the UWB system. As a result, combining MIMO technologies in UWB design has become the main trend in UWB studies [9–10]. In this sense, research on UWB MIMO antennas has emerged as a hotspot in wireless communication system research. The combined use of UWB and MIMO technologies is anticipated to bring about new opportunities and challenges for UWB antennas [11].

The main challenge of UWB MIMO antennas in mobile terminals is achieving high isolation between

antenna elements [12]. In [13, 14], neutralization line structures are used between antenna elements to reduce mutual coupling, while in [15–19], polarization diversity technology is used to achieve natural isolation. In [20–24], mutual coupling is reduced by using defected ground structures (DGS). For instance, [23] etches two novel bent slits into the ground plane and achieves -10 dB  $S_{11}$  and -18 dB  $S_{21}$  from 2.4 to 6.55 GHz. In addition, antenna elements isolation can also be improved by loading parasitic elements [25–28]. For instance, a parasitic T-shaped strip is used as a decoupling structure between the radiating elements in [28], enabling the antenna to operate from 3.08 to 11.8 GHz with 15 dB isolation. Electromagnetic band gap (EBG) structures are also considered [29–31]. The proposed EBG structures employ two closely coupled arrays, one comprising linear conducting patches and the other comprising apertures (slits) in the ground plane, to reduce the  $S_{12}$  to values lower than -20 dB from 3.44 to 6.13 GHz [31]. All these techniques have proven useful for constructing different resonant structures corresponding to different frequencies. Since DGS is preferably used for improving decoupling while parasitic structures are more often used to broaden the bandwidth, this work combines these two techniques to design a MIMO antenna system meeting both requirements.

In this paper, a 4-element UWB MIMO antenna is designed and fabricated. For the element design, the proposed tapered fed hexagon-shaped patch microstrip is simulated and verified to achieve a wide operating band from 3 GHz to 10.6 GHz. A dual-element MIMO antenna is then constructed, and 15 dB isolation performance is achieved through DGS and parasitic branch structure. Furthermore, a 4-element MIMO antenna is realized where decoupling of the compact MIMO antenna is achieved through the design of two E-shaped branch structures. Simulation results show that the overall operating bandwidth of the system is further broadened up to 18 GHz. The isolation of

each two elements is greater than 15 dB. Section II describes the methodology of this work; it illustrates the design process from a single element to the 4-element array, as well as theoretical analysis and simulation verification. Section III shows the measured results as well as discussion, and Section IV concludes the paper.

## II. METHODOLOGY

### A. Design of the single-element UWB antenna

The configuration of the proposed UWB antenna element is presented in Fig. 1. It uses 1.6 mm thick FR4 ( $\epsilon_r = 4.4$ ) as the substrate. On top of the substrate, a hexagon-shaped radiated patch and a tapered feedline form a hexagon-shape monopole. On the bottom of the substrate, the ground plane is half cut off to form a DGS, which effectively improves the impedance matching bandwidth of the antenna. Detailed dimensions of the single-element antenna are given in Table 1.

In the process of impedance matching design, the evolution of the proposed UWB antenna is exhibited in Fig. 2. Simulated results of each step (shape of element patch transferred from sample *a* to *d*) are illustrated in Fig. 3. The hexagon-shaped patch microstrip has better broadband characteristics (3 to 10.6 GHz) compared with other common microstrip patch shapes, such as rectangular, triangular, and circular shapes, because the hexagonal radiating patch owns more uniform electric field distribution at the edges of the antenna, which reduces edge effects and impedance changes.

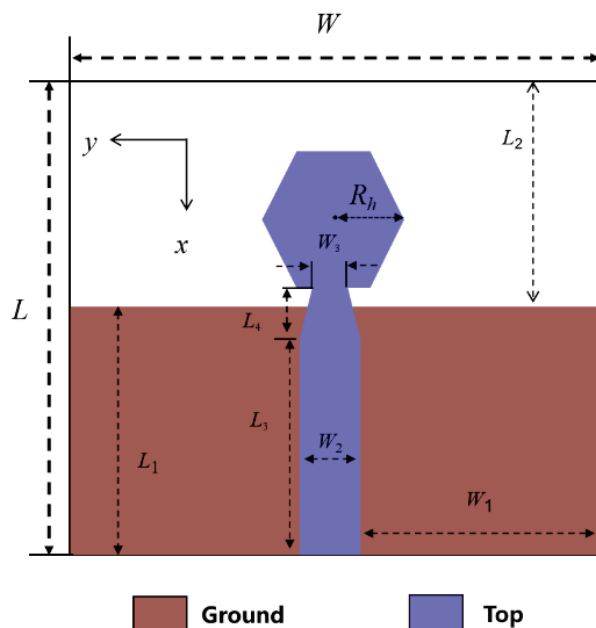


Fig. 1. Structure of the proposed antenna element.

Table 1: Dimensions of the single-element antenna

Par.	Value (mm)	Par.	Value (mm)
$L$	17.5	$L_4$	5.77
$W$	46	$W_1$	10
$L_1$	18.1	$W_2$	3.01
$L_2$	16.9	$W_3$	2.01
$L_3$	13.26	$R_h$	7

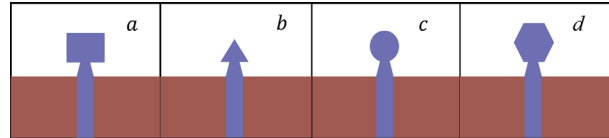


Fig. 2. Evolution of a UWB antenna element.

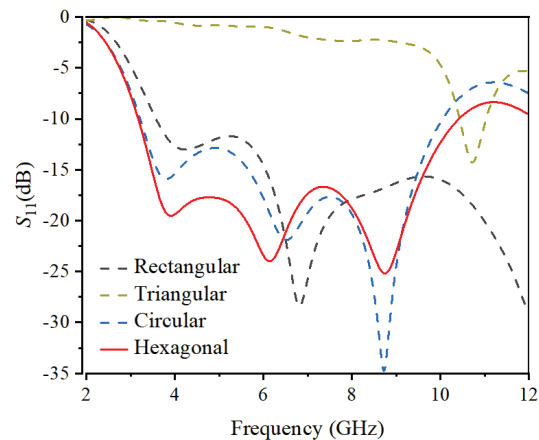


Fig. 3. Simulated  $S$ -parameters of the four types of antenna element in Fig. 2.

### B. Design of dual-element UWB MIMO antenna

Since the single-element antenna has achieved satisfying bandwidth, we make one step further to develop a dual-element MIMO system. The configuration of the dual-element UWB MIMO antenna element is presented in Fig. 4. It uses 1.6 mm thick FR4 ( $\epsilon_r = 4.4$ ) as the substrate. On top of the substrate, two tapered feeds and two hexagonal radiating patches are arranged in parallel. On the bottom of the substrate, the ground plane uses etched rectangular slots to improve the mutual decoupling. It is found that the effect between the two elements changes the surface current and the electromagnetic field distribution near the feeding point, and therefore changes the impedance bandwidth. This dual-element antenna operates within a wide frequency range of 3-18 GHz. The dimensions of the dual-element antenna are given in Table 2.

In [32], the mentioned antenna system achieves 15 dB isolation (3.1-11.8 GHz) using parasitic branch

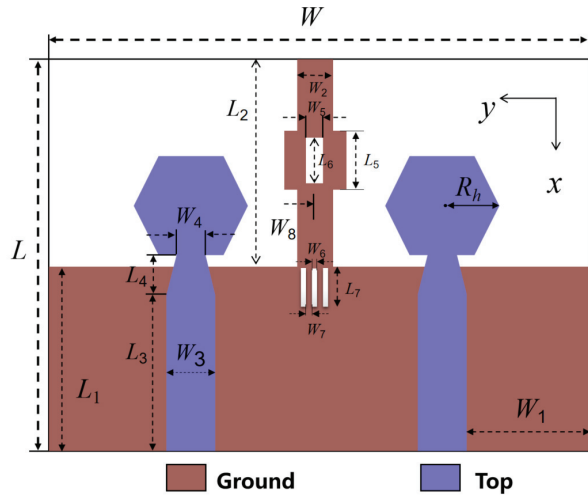


Fig. 4. Dual-element UWB MIMO antenna.

Table 2: Dimensions of the dual-element antenna

Par.	Value (mm)	Par.	Value (mm)	Par.	Value (mm)
$L$	35	$L_5$	6	$W_4$	2.01
$W$	46	$L_6$	5	$W_5$	3
$L_1$	18.1	$L_7$	4	$W_6$	0.5
$L_2$	16.9	$W_1$	10	$W_7$	0.5
$L_3$	13.26	$W_2$	3.5	$W_8$	1.5
$L_4$	5.77	$W_3$	3.01	$R_h$	7

structures. This method provides good isolation over a wider bandwidth. On the other hand, in [36], the described antenna system achieves 19 dB isolation (2.4–6.55 GHz) using DGS. This method offers better isolation compared to the method in [32], but over a narrower bandwidth. The proposed dual-element UWB MIMO antenna system in this paper utilizes both DGS and parasitic branch structures.

This design proposes a series of solutions to address the issue of mutual interference among multiple antennas in MIMO systems. Figure 5 illustrates the design process (from model *a* to *d*) and evolution of  $S$ -parameters of the dual-element UWB antenna. The operating frequency range of all these setups are 3–18 GHz. From model *a* to *d*, a loop structure was realized by etching a rectangular groove in the metal strip to guide the surface current into the ground plane. Further improvement was achieved by etching three rectangular slots into the ground of *b*, resulting in the isolation ( $S_{12}$ ) of the antenna elements greater than 15 dB at high frequencies (14–18 GHz). To ensure the isolation of the elements depicted in *c* remained greater than 15 dB in the 7–10 GHz range, two rectangular metal stubs were added to the edge of the

Table 3: The performance comparison of the 2-element antenna

Ref	Size (mm)	Isolation (dB)
[32]	$38 \times 38 \times 1.6$	$>15$ (3.1~11.8 GHz)
[33]	$90 \times 40 \times 0.79$	$>17$ (2.4~4.2 GHz)
[34]	$50 \times 40 \times 1.6$	$>15$ (2.5~12 GHz)
[35]	$48 \times 48 \times 0.8$	$>18$ (2.5~12 GHz)
[36]	$78 \times 40 \times 1.6$	$>19$ (2.4~6.55 GHz)
Proposed	$46 \times 35 \times 1.6$	$>15$ (3~18 GHz)

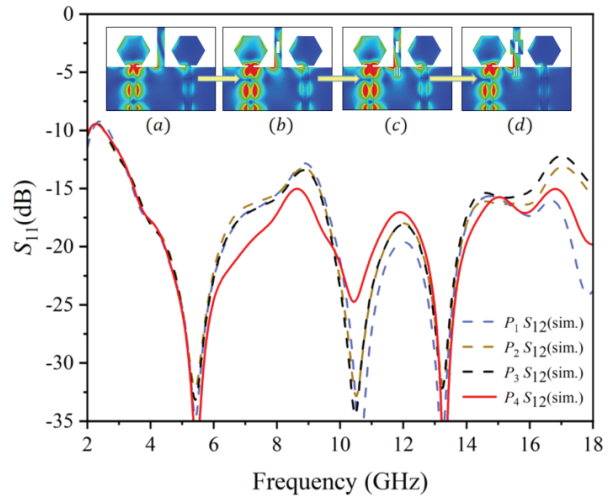


Fig. 5. The evolution of structure and surface current in the dual-element MIMO antenna.

*c* metal strip. The final dual-element design is referred to as in *d*.

The  $S$ -parameters for the dual-element UWB MIMO antenna are shown in Fig. 6. The operating frequency

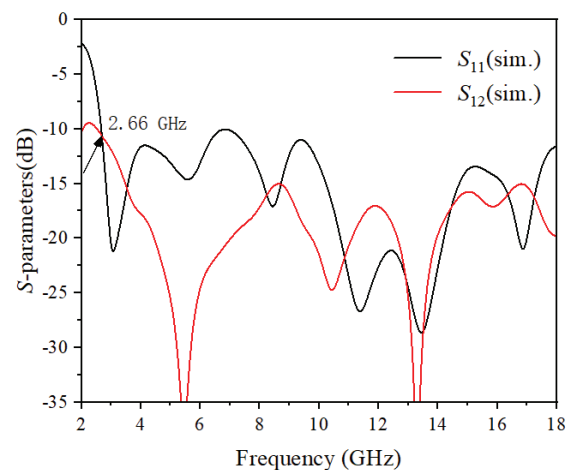


Fig. 6. The  $S$ -parameters of the dual-element MIMO antenna.

range of the antenna meets the requirement of being less than -10 dB from 3 GHz to 18 GHz. The  $S_{12}$  of the antenna remains less than -15 dB across the UWB frequency range, meeting the requirement of antenna isolation for MIMO systems.

### C. Design of 4-element UWB MIMO antenna

Based on the dual-element MIMO antenna, the final pattern of the proposed 4-element UWB MIMO system is realized and presented in Fig. 7. It has an overall size of  $92 \times 70 \times 1.6\text{mm}^3$ . On top of the FR4 substrate, the dual-element antenna pairs are placed symmetrically, while on the bottom, two E-shaped branch structures are designed to further improve the mutual decoupling. The operating bandwidth of the MIMO system is also 3-18 GHz, sufficiently meeting the wideband requirement. The dimensions of the quad-element antenna are given in Table 4.

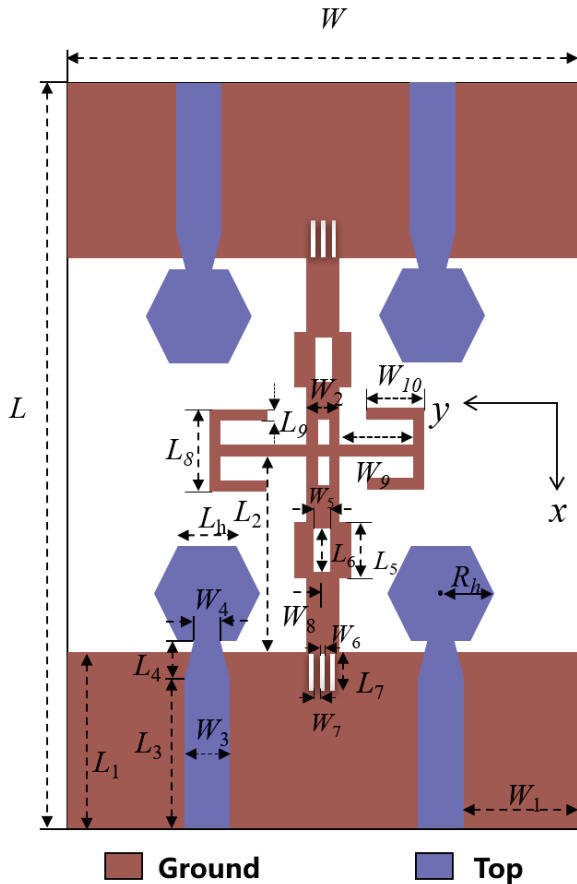


Fig. 7. Configuration of the 4-element MIMO antenna.

Through simulation of the proposed 4-element UWB MIMO antenna, the  $S$ -parameters in Fig. 8 are obtained and discussed. It is clear that  $S_{11}$  is less than -10 dB from 3 GHz to 18 GHz. On the whole operating

Table 4: Dimensions of the 4-element antenna

Par.	Value (mm)	Par.	Value (mm)	Par.	Value (mm)
$L$	35	$L_7$	4	$W_6$	0.5
$W$	46	$L_8$	5	$W_7$	0.5
$L_1$	18.1	$L_9$	0.5	$W_8$	1.5
$L_2$	16.9	$W_1$	10	$W_9$	5
$L_3$	13.26	$W_2$	3.5	$W_{10}$	4
$L_4$	5.77	$W_3$	3.01	$R_h$	7
$L_5$	6	$W_4$	2.01		
$L_6$	5	$W_5$	3		

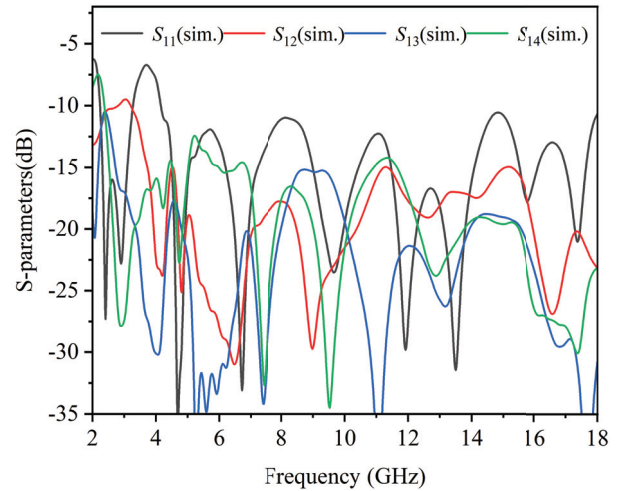


Fig. 8. The selected simulated  $S$ -parameters for the quad-element UWB MIMO antenna.

band, the isolation degree of arbitrary two elements reach more than 15 dB, indicating that the mutual coupling between the four elements is effectively suppressed. One of the key advantages of this system is its ability to achieve a 15 dB isolation range of operating (3-18 GHz) frequency.

When one port is excited and the other three ports are terminated, the surface current distribution is simulated at 5 GHz, 10 GHz, and 15 GHz, respectively, as shown in Fig. 9. The design of E-shaped branches between the two dual-element MIMO antenna pairs forms current loops, and the current generated by the radiation patch flows into the ground plane through the rectangular metal strip. This effectively reduces the coupling between the four antenna elements, resulting in good independence between the antenna elements and achieving the expected isolation.

The total efficiency of the 4-element UWB MIMO antenna is shown in Fig. 10; the simulated efficiency value within the whole operating band testifies to the functionality and applicability of the proposed system.

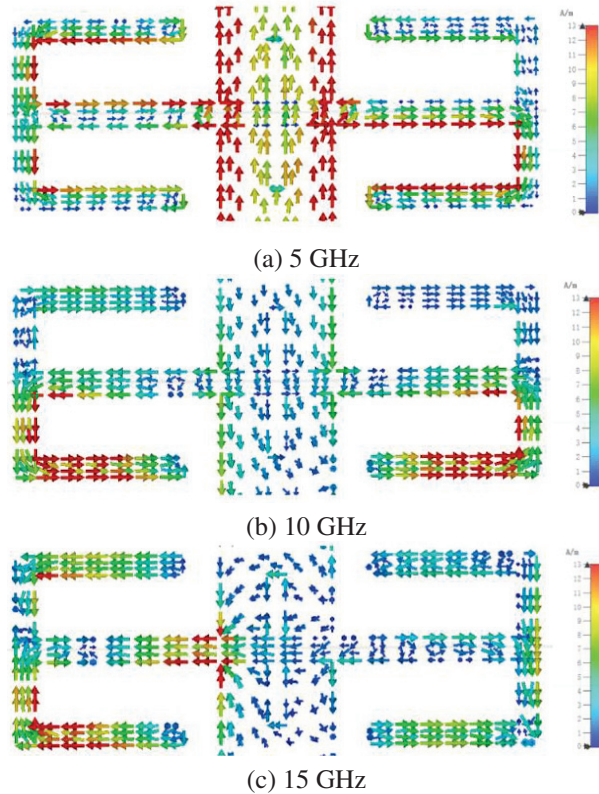


Fig. 9. Surface current distribution of the 4-element UWB MIMO antenna at (a) 5 GHz, (b) 10 GHz, and (c) 15 GHz.

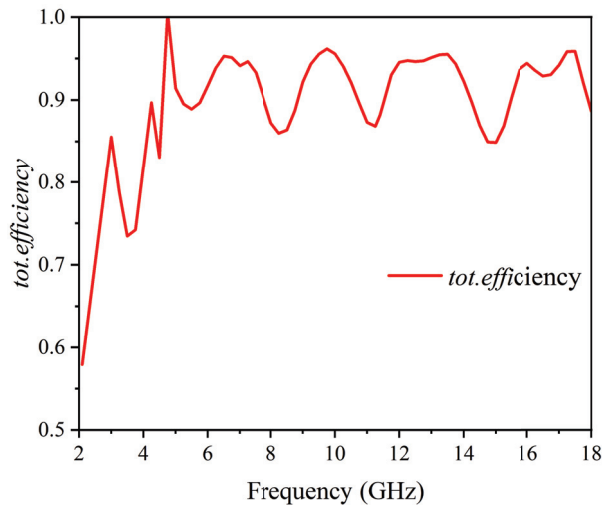


Fig. 10. The total efficiency of the 4-element UWB MIMO antenna.

The four-element MIMO antenna system can enhance the capacity and data rates of wireless communication systems. It enables improved signal quality, increased spectral efficiency, and enhanced cover-

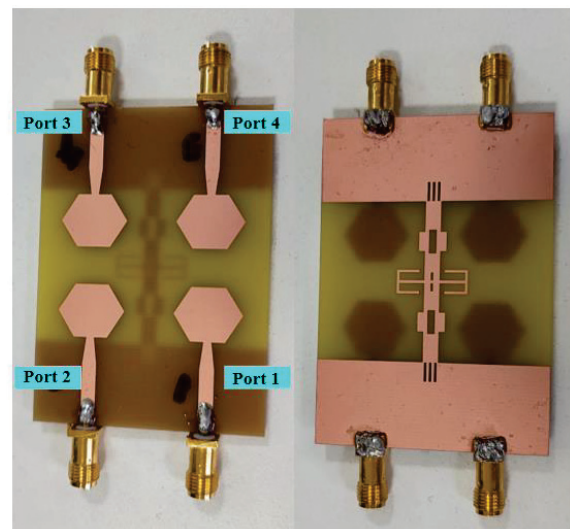
age, making it suitable for applications such as 5G and beyond.

### III. MEASUREMENT AND DISCUSSION

Figure 11 shows a snapshot of the fabricated model of the proposed UWB MIMO antenna, with Fig. 11 (a) representing the front side view of the antenna and Fig. 11 (b) representing the back side view of the antenna. Through measurements of the fabricated prototype, Fig. 12 shows the comparison between simulated and measured data of the MIMO antenna's  $S$ -parameters. The measurements demonstrate that the bandwidth and isolation of the proposed antenna closely match the simulations. The operating bandwidth is from 3 GHz to 18 GHz with a 15 dB isolation performance, indicating that the design of the MIMO system does not affect the radiation characteristics of the UWB antenna.

The envelope correlation coefficient (ECC) quantifies the correlation between signals transmitted from different wireless communication channels and received by antennas, reflecting the degree of coupling in MIMO antennas. A lower ECC value indicates less coupling between ports, which is desirable for achieving high diversity performance. ECC values below 0.5 are typically preferred. ECC can be calculated using the scattering  $S$ -parameter, with the formula

$$ECC = \frac{\left| S_{ii}^* S_{ij} + S_{ji}^* S_{jj} \right|^2}{\left[ \left( 1 - |S_{ii}|^2 - |S_{ji}|^2 \right) \cdot \left( 1 - |S_{jj}|^2 - |S_{ij}|^2 \right) \right]} \quad (1)$$



(a) Front side (b) Back side

Fig. 11. Snapshot of fabricated prototype of the 4-element UWB MIMO antenna: (a) Front view and (b) back view.

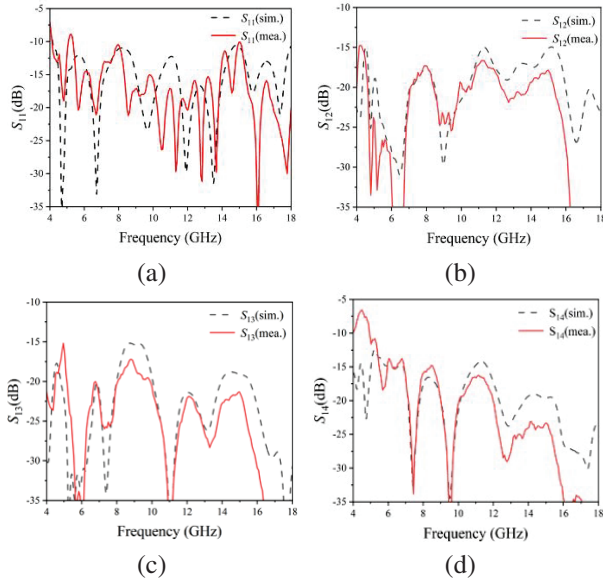


Fig. 12. Measurement and simulation results of the  $S$ -parameter for this 4-element MIMO antenna: (a)  $S_{11}$ , (b)  $S_{12}$ , (c)  $S_{13}$ , and (d)  $S_{14}$ .

Diversity gain (DG) is a key metric for evaluating diversity performance. A higher diversity gain is achieved when there is less correlation among the antenna elements. The relationship between DG and ECC is illustrated in equation (2):

$$DG = 10 \times \sqrt{1 - |ECC|}. \quad (2)$$

These two parameters are calculated in this work according to (1) and (2), as shown in Fig. 13, where the ECC performance is less than 0.01 and DG is greater than 9.95.

The overall data comparison shows excellent agreement between the measured results and the simulation results, indicating good isolation and high gain characteristics of the antenna. Furthermore, the ingenious and

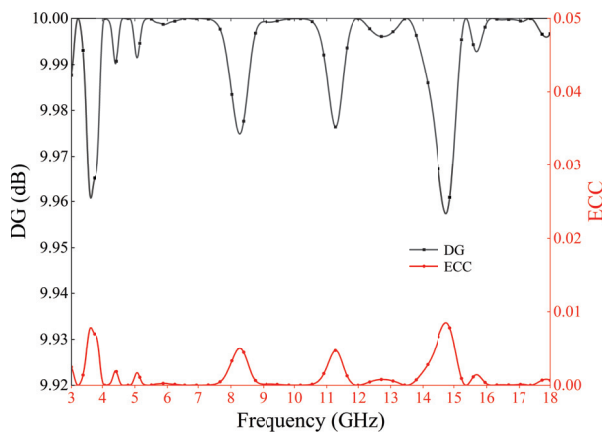


Fig. 13. ECC and DG results of the MIMO antenna.

novel structure confirms the proposed antenna as a desirable candidate for UWB-MIMO applications.

#### IV. CONCLUSION

In this paper, a four element UWB-MIMO antenna with DGS and parasitic decoupling structures is proposed and analyzed. The antenna is operable from 3 GHz to 18 GHz, which is a superior wide operating band. Design of decoupling structures such as multiple slots, stubs, and E-shaped symmetric strips achieves a 15 dB high isolation within the ultrawide operating band. Simulated total efficiency is greater than 0.8 and the ECC is less 0.01, whereas DG is greater than 9.95 across the frequency range. Simulations and measurements agree well and show that the proposed antenna is a good candidate for the UWB-MIMO applications.

#### ACKNOWLEDGMENT

This work was supported by the Natural Science Foundation of Xiamen, China (3502Z20227053), the Natural Science Foundation of Fujian Province (2022J01342), and the China Mobile Group Devices Co., Ltd (Grant No. CMDC-2022-94164-GY772).

#### REFERENCES

- [1] M. NejatiJahromi, M. N. Jahromi and M. Rahman, "A new compact planar antenna for switching between UWB, narrow band and UWB with tunable-notch behaviors for UWB and WLAN applications," *Appl. Comput. Electromagn. Soc.*, vol. 33, pp. 400-406, 2021.
- [2] S. Park and K. Y. Jung, "Novel compact UWB planar monopole antenna using a ribbon-shaped slot," *IEEE Access*, vol. 10, pp. 61951-61959, 2022.
- [3] Y. Yang, Z. Zhao, X. Ding, Z. Nie, and Q.-H. Liu, "Compact UWB slot antenna utilizing traveling-wave mode based on slotline transitions," *IEEE Trans. Antennas Propagat.*, vol. 67, no. 1, pp. 140-150, 2019.
- [4] S. Sung, H. Kim, and J.-I. Jung, "Accurate indoor positioning for UWB-based personal devices using deep learning," *IEEE Access*, vol. 11, pp. 20095-20113, 2023.
- [5] Y. K. Wang, L. Li, X. Y. Zhou, and T. J. Cui, "Supervised Automatic Detection of UWB ground-penetrating radar targets using the regression SSIM measure," *IEEE Geoscience Remote Sens. Letters*, vol. 13, no. 5, pp. 621-625, 2016.
- [6] T. Mavridis, J. Sarrazin, L. Petrillo, P. De Doncker, and A. Benlarbi-Delai, "Information spatial focusing scheme for UWB wireless communications in smart environments," *IEEE Antennas Wirel. Propagat. Lett.*, vol. 14, pp. 20-23, 2015.
- [7] K. Bahadori and Y. Rahmat-Samii, "A miniaturized elliptic-card UWB antenna with WLAN band rejection for wireless communications," *IEEE*

- Transactions Antennas Propagat.*, vol. 55, no. 11, pp. 3326-3332, 2007.
- [8] B. Zhou, F. Chen, W. Rhee, and Z. Wang, "A reconfigurable FM-UWB transceiver for short-range wireless communications," *IEEE Microwave Wirel. Comput. Lett.*, vol. 23, no. 7, pp. 371-373, July 2013.
- [9] G. Srivastava and A. Mohan, "Compact MIMO slot antenna for UWB applications," *IEEE Antennas Wirel. Propagat. Lett.*, vol. 15, pp. 1057-1060, 2016.
- [10] M. Naser-Moghadasi, H. Roustaa, and B. S. Virdee, "Compact UWB planar monopole antenna," *IEEE Antennas Wirel. Propagat. Lett.*, vol. 8, pp. 1382-1385, 2009.
- [11] W. K. Toh, X. Qing, and Z. N. Chen, "A planar UWB patch-dipole antenna," *IEEE Trans. Antennas Propagat.*, vol. 59, no. 9, pp. 3441-3444, Sep. 2011.
- [12] L. Y. Nie, X. Q. Lin, Z. Q. Yang, J. Zhang, and B. Wang, "Structure-shared planar UWB MIMO antenna with high isolation for mobile platform," *IEEE Trans. Antennas Propagat.*, vol. 67, no. 4, pp. 2735-2738, 2019.
- [13] A. Mohanty and B. R. Behera, "Investigation of 2-port UWB MIMO diversity antenna design using characteristics mode analysis," *AEU – I. J. Electron Commun.*, vol. 124, p. 153361, 2020.
- [14] A. Kayabasi, A. Toktas, E. Yigit, and K. Sabanci, "Triangular quad-port multi-polarized UWB MIMO antenna with enhanced isolation using neutralization ring," *AEU – I. J. Electron Commun.*, vol. 85, pp. 47-53, 2018.
- [15] A. S. Eltrass and N. A. Elborae, "New design of UWB-MIMO antenna with enhanced isolation and dual-band rejection for WiMAX and WLAN systems," *IET Microwaves Antennas*, vol. 13, pp. 683-691, 2019.
- [16] M. M. Hassan, M. Rasool, M. U. Asghar, Z. Zahid, A. A. Khan, I. Rashid, A. Rauf, and F. A. Bhatti, "A novel UWB MIMO antenna array with band notch characteristics using parasitic decoupler," *J. Electromagn. Waves Appl.*, vol. 34, no. 9, pp. 1225-1238, 2020.
- [17] Y. I. Nechayev, C. C. Constantinou, X. Wu, and P. S. Hall, "De-polarization of on-body channels and polarization diversity at 60 GHz," *IEEE Trans. Antennas Propagat.*, vol. 62, no. 12, pp. 6519-6523, 2014.
- [18] K. Wei, B. Zhu, and M. Tao, "The circular polarization diversity antennas achieved by a fractal defected ground structure," *IEEE Access*, vol. 7, pp. 92030-92036, 2019.
- [19] S. Hiraoka, Y. Nakashima, T. Yamazato, S. Arai, Y. Tadokoro, and H. Tanaka, "Interference-aided detection of subthreshold signal using beam control in polarization diversity reception," *IEEE Commun. Lett.*, vol. 22, no. 9, pp. 1926-1929, 2018.
- [20] P. Kumar, S. Pathan, S. Vincent, O. P. Kumar, N. Washwanth, P. Kumar, P. R. Shetty, and T. Ali, "A compact quad-port UWB MIMO antenna with improved isolation using a novel mesh-like decoupling structure and unique DGS," *IEEE Transactions on Circuits and Systems II: Express Briefs*, vol. 70, no. 3, pp. 949-953, 2023.
- [21] R. Gómez-Villanueva and H. Jardón-Aguilar, "Compact UWB uniplanar four-port MIMO antenna array with rejecting band," *IEEE Antennas Wirel. Propagat. Lett.*, vol. 18, no. 12, pp. 2543-2547, 2019.
- [22] P. Kumar, S. Pathan, S. Vincent, O. P. Kumar, N. Washwanth, P. Kumar, P. R. Shetty, and T. Ali, "Design of a six-port compact UWB MIMO antenna with a distinctive DGS for improved isolation," *IEEE Access*, vol. 10, pp. 112964-112974, 2022.
- [23] J.-F. Li, Q.-X. Chu, and T.-G. Huang, "A compact wideband MIMO antenna with two novel bent slits," *IEEE Trans. Antennas Propagat.*, vol. 60, no. 2, pp. 482-489, 2012.
- [24] T. Shabbir, R. Saleem, A. Akram, and F. Shafique, "UWB-MIMO quadruple with FSS-inspired decoupling structures and defected grounds," *Applied Computational Electromagnetics Society (ACES) Journal*, vol. 30, pp. 84-190, 2021.
- [25] K. Phaebua, C. Phongcharoenpanich, D. Torrungrueng, N. Surittikul, and W. Villarroel, "An eight-branch folded strip antenna with a circular parasitic patch on circular ground plane for SDARS application," *2009 IEEE Antennas Propagat. Soc. Inter. Sym.*, pp. 1-4, 2009.
- [26] P.-H. Deng, M.-W. Li, W.-T. Chen, C.-H. Lin, C.-H. Lu, R.-T. Tsai, and K.-H. Chen, "Designs of branch-line couplers by considering the parasitic effects of P-I-N diodes," *IEEE Access*, vol. 8, pp. 223089-223100, 2020.
- [27] P. Jha, A. Kumar, A. De, and R. K. Jain, "Super ultra-wideband planar antenna with parasitic notch and frequency selective surface for gain enhancement," *Applied Computational Electromagnetics Society (ACES) Journal*, vol. 37, pp. 757-764, 2022.
- [28] L. Kang, H. Li, X. Wang, and X. Shi, "Compact offset microstrip-fed MIMO antenna for band-notched UWB applications," *IEEE Antennas Wirel. Propagat. Lett.*, vol. 14, pp. 1754-1757, 2015.
- [29] S. Barth and A. K. Iyer, "The MTM-EBG as a rigorous multiconductor model of the UC-EBG and approaches for miniaturization," *IEEE Trans. Antennas Propagat.*, vol. 70, no. 4, pp. 2822-2831, 2022.

- [30] M. Kashani, L. Shafai, and D. Isleifson, "Truncated and suspended microstrip patch antennas over an EBG ground plane," *IEEE 19th International Symposium Antenna Technology Applied Electromagnetics*, Winnipeg, MB, Canada, pp. 1-2, 2021.
- [31] Q. Li, A. P. Feresidis, M. Mavridou, and P. S. Hall, "Miniaturized double-layer EBG structures for broadband mutual coupling reduction between UWB monopoles," *IEEE Trans. Antennas and Propagat.*, vol. 63, no. 3, pp. 1168-1171, 2015.
- [32] L. Kang, H. Li, X. Wang, and X. Shi, "Compact offset microstrip-fed MIMO antenna for band-notched UWB applications," *IEEE Antennas and Wireless Propagation Letters*, vol. 14, pp. 1754-1757, 2015.
- [33] C. H. See, R. A. Abd-Alhameed, and Z. Z. Abidin, "Wideband printed MIMO/diversity monopole antenna for Wi Fi/Wi MAX applications," *IEEE Transactions on Antennas and Propagation*, pp. 2028-2035, 2012.
- [34] G. Lin, C. Sung, J. Chen, and M. Hung, "Isolation improvement in UWB MIMO antenna system using carbon black film," *IEEE Antennas and Wireless Propagation Letters*, pp. 222-225, 2017.
- [35] P. Gao, S. He, X. Wei, and Z. Xu, "Compact printed UWB diversity slot antenna with 5.5-GHz band-notched characteristics," *IEEE Antennas and Wireless Propagation Letters*, pp. 376-379, 2014.
- [36] J. Li, Q. Chu, and T. Huang, "A compact wideband MIMO antenna with two novel bent slits," *IEEE Transactions on Antennas and Propagation*, vol. 60, no. 2, pp. 482-489, 2012.



**Tongyu Ding** was born in Heilongjiang, China in 1987. He received the M.S. degree from Harbin Institute of Technology, China and the Ph.D. degree in electronics and communication engineering from the Politecnico di Torino, Italy, in 2011 and in 2015, respectively. Currently he is an associate professor with the School of Ocean Information Engineering, Jimei University. His recent research interests include antennas, RIS, and numerical techniques for 5G wireless communications.



**Haobin Yang** was born in Sichuan, China. He obtained his bachelor's degree from Jimei University, Xiamen, China, in 2023. Currently, he is pursuing a master's degree at Jimei University. His main research focus is on reconfigurable intelligent surfaces.



**Zhiwei Chen** was born in Fujian, China. He enrolled in Jimei University in 2021 and is currently working toward the bachelor's degree at the School of Ocean Information Engineering. His recent research interest is UWB MIMO antennas.



**Zhen Lin** graduated from the Department of Electronic and Communication Engineering, South China University of Technology, in 2000. He joined China Mobile in 2004. In 2019, he received his doctor's degree in administration from Huazhong University of Science and Technology. Currently, he is the general manager of R&D Center of China Mobile Communications Group Terminal Co., LTD., mainly engaged in the R&D management of terminal software and hardware in the field of smart home.



**Bin He** graduated from the Institute of Computing Technology, Chinese Academy of Sciences in 2005 with a master's degree. He is currently the deputy general manager of the R&D Center of China Mobile Communications Group Terminal Co., LTD., engaged in the research and development of intelligent terminal products hardware and software and related platforms.



**Chong-Zhi Han** received the B.E. degree and the M.Eng. degree in electronic information engineering from Harbin Institute of Technology, Harbin, China. In 2020, he received the Ph.D. degree in Shenzhen University, Shenzhen, China. Currently he is an associate professor with the School of Ocean Information Engineering, Jimei University. His current research interests include the development and application of MIMO antennas and millimeter wave antennas.

# Rigorous Analysis and Design of Resistor-Loaded Patch Antennas with Flexible Gain for Indoor Radar Sensors

Shu-Wei Yu<sup>1</sup>, Xiao Zhang<sup>1,\*</sup>, Qiong-Sen Wu<sup>2</sup>, Lei Zhu<sup>3</sup>, Tao Yuan<sup>1</sup>, and Xian-Qin Hu<sup>4</sup>

<sup>1</sup>College of Information Engineering  
Shenzhen University, Shenzhen, 518060, China  
xiao.zhang@szu.edu.cn  
\*Corresponding Author

<sup>2</sup>School of Integrated Circuits  
Guangdong University of Technology, Guangzhou, 510006, China

<sup>3</sup>Faculty of Science and Technology  
University of Macau, Macao, 999078, China

<sup>4</sup>Avary Holding (Shenzhen) Co., Ltd  
Shenzhen, 518060, China

**Abstract** – A high-precision cavity model of resistor-loaded patch antenna (RLPA) with adjustable gain is proposed and rigorously studied in this article. In our analysis, the loaded resistors are perceived as controlled current sources, thus the RLPA can be solved as a modified cavity model. Accurate expressions of field distribution, input impedance, and radiation patterns are derived in this way, and a gratifying agreement has been achieved between the calculated and simulated results. Based on this approach, RLPAs for indoor motion radar are designed and analyzed. Comprehensive analysis is conducted to reveal the loading effect on radiation gain, radiation efficiency, and quality factor of RLPAs under various circumstances. Through altering the value of the loaded resistance, its radiation gain and coverage range can be flexibly adjusted. Besides, enhanced operating bandwidth and improved performance stability are also achieved due to the loaded resistors. Last but not least, several indoor motion radars based on the proposed patches are carried out and measured, which demonstrates the validity of the proposed method and design.

**Index Terms** – Cavity model, flexible gain, indoor motion radar, resistor-loaded patch antennas.

## I. INTRODUCTION

As the applications of smart home services are experiencing an appreciable growth in recent years, the microwave motion sensor system used for human body sensing has become an attractive solution for the realization of indoor intelligent services [1]. A microwave sensor is able to detect humans in a certain range [2], thus

providing necessary data for the control strategy of smart home services.

Microstrip patch antennas are widely applied in these sensors, and they satisfy most requirements except the capacity of recognition scope adjustment, which is in high demand. The working scenario sample is illustrated in Fig. 1. Due to the penetrability of microwaves [3], humans in the occupied room are potentially detectable by the radar in the empty room. Consequently, the lights and air conditioner in the empty room will be falsely triggered. In the need of resolving this problem, a gain adjustable antenna is required for the purpose of flexible radiation coverage.

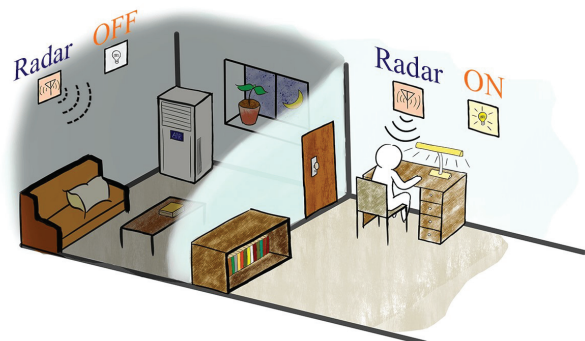


Fig. 1. A scenario of the indoor motion sensor application. The 5.8 GHz radar in the occupied room detects the existence of humans and automatically turns the light on, while the radar in the empty room detects no living creature and turns the domestic appliances off.

Altering the transmitting power of the chip might be the most direct solution. However, most low-price chips cannot afford additional power-control circuits [4]. A relatively simple solution is to load a chip capacitor to the feeding circuit, which changes the reflection and thus adjusts realized gain.

To achieve a similar effect, lumped impedance can be loaded to the patches as well. Through loading capacitors or inductors to the patches, miniaturization [5–9], frequency/polarization tuning [10–17], or gain enhancement [18] can be achieved. However, the aforementioned antennas suffer from narrow bandwidth and are sensitive to manufacture deviation.

Compared with the sufficient studies above, relatively little research has concentrated on the topic of resistor-loaded patch antennas (RLPAs). In reported works, the resistor loading technique is primarily adopted for impedance matching [20], frequency tuning [21], and bandwidth widening [22–25]. These works have already noticed the non-negligible impact brought by resistors on the total efficiency. However, few of them propose precise models or analytical methods for RLPAs.

As is well known, the cavity model theory is an effective and high-accuracy method to analyze regular patch antennas [26–27]. However, to the best of our knowledge, no one used to apply the cavity model to the analysis of RLPAs.

In this article, a reformative cavity model for the rectangular patch antenna loaded with resistors is presented, which offers an alternative perspective on the analysis of this kind of patch antenna. This model perceives the loaded resistors as multiple controlled current sources, thus transferring the RLPA model into a multi-excitation cavity model. For validation, the calculation results with the proposed method are compared with the simulation results of the commercial ANSYS HFSS simulator, and satisfactory agreement is achieved.

Last but not least, an indoor radar module equipped with the proposed RLPA is designed and measured. By changing the loaded resistance, different coverage ranges are achieved. Additionally, the enhanced bandwidth can alleviate the risk of performance deviation of final products, which validates the promising practicality of RLPA.

**II. ANALYSIS OF CAVITY MODEL**

In this section, an improved cavity model is developed for the rectangular RLPA, which aims to provide a rigorous and accurate solution for the antenna design. The configuration of the antenna is shown in Fig. 2 (a). The patch is placed on the  $x$ - $y$  plane, and four resistors are symmetrically loaded to the four corners of the patch for load-balance. The patch is fed by a probe along the central line.

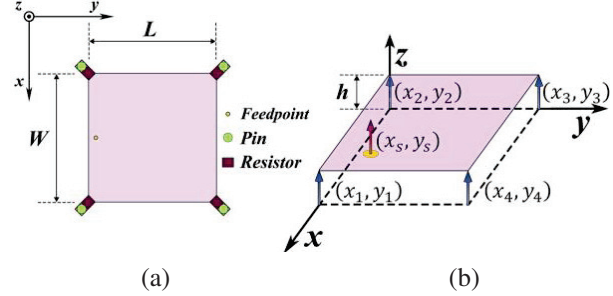


Fig. 2. The proposed resistor-loaded patch antenna and its cavity model: (a) Configuration and (b) equivalent cavity model.

Table 1: Parameters of the resistor-loaded patch

Param.	Val. (mm)	Param.	Val. (mm)
$W$	11.8	$(x_1, y_1)$	(11.8, 0)
$L$	11.8	$(x_2, y_2)$	(0, 0)
$h$	0.8	$(x_3, y_3)$	(0, 11.8)
$(x_s, y_s)$	(5.9, 0.5)	$(x_4, y_4)$	(11.8, 11.8)

**A. Electric field distribution**

The electric field expression is critical for predicting the impedance and radiation patterns of the patch antenna, and so it is derived first. According to the classical cavity model [28], the rectangular patch antenna is perceived as a lossy cavity in which the electric field distribution is bounded by two parallel electric walls (at the top and bottom) and four magnetic walls surrounding the periphery of patch, as shown in Fig. 2 (b). Its interior field wave equation is written as

$$(\nabla^2 + k^2) E_z = j\omega\mu_0 J_z, \tag{1}$$

where  $k$  is the wave number in the dielectric and  $J_z$  is the total excitation source inside the cavity.

In the cavity model, the excitation is frequently equivalent to a current sheet which has width  $d_s$  and is located at  $(x_s, y_s)$  with a joint current of  $I_s$ . In order to solve the resistor loading problem, a resistor  $Z_i$  loaded to the patch is regarded as an  $E_z$ -controlled current source, which is equivalent to a current sheet with width  $d_i$  and located at  $(x_i, y_i)$  with a joint current of  $E_z(x_i, y_i)h/Z_i$ , as shown in Fig. 2 (b). Therefore, the total excitation  $J_z$  is expressed as

$$J_z = \begin{cases} \frac{I_s}{d_s} & x_s - \frac{d_s}{2} < x < x_s + \frac{d_s}{2}, y = y_s \\ \frac{E_z(x_i, y_i)h}{Z_i d_i} & x_i - \frac{d_i}{2} < x < x_i + \frac{d_i}{2}, y = y_i, i = 1, 2, 3, \dots \\ 0 & \text{others} \end{cases} \tag{2}$$

where the variable  $i$  represents the number of resistors loaded on the patch and the total amount of loaded resistors is set as  $q$ .

On the basis of this assumption, the loaded resistors do not change the eigen wave equation of this cavity.

Utilizing the eigenmode expansion method, the solution of (1) can be expressed as the superposition of various eigenmodes of the cavity.

$$E_z(x, y) = \sum_{m, n} A_{mn} \Psi_{mn}(x, y), \quad (3)$$

$$\Psi_{mn} = C_{mn} \cos(k_m x) \cos(k_n y). \quad (4)$$

As shown above, the eigenfunctions are completely determined by the boundary condition of the cavity, and they are independent of the loaded resistors themselves.

Separately, the mode weighting coefficients  $A_{mn}$  are determined by the total excitation  $J_z$  in the cavity.

$$A_{mn} = \frac{j\omega\mu_0}{k^2 - k_{mn}^2} \frac{\int_S J_z \Psi_{mn}^* ds}{\int_S \Psi_{mn} \Psi_{mn}^* ds}. \quad (5)$$

The numerator and denominator of (5) are calculated by

$$\int_S J_z \Psi_{mn}^* ds = C_{mn} \left( \cos(k_n y_s) \int_{x_s - \frac{d_s}{2}}^{x_s + \frac{d_s}{2}} \frac{J_z}{d_s} \cos(k_m x) dx + \sum_{i=1}^q \cos(k_n y_i) \int_{x_i - \frac{d_i}{2}}^{x_i + \frac{d_i}{2}} \frac{E_z(x_i, y_i) h}{Z_i d_i} \cos(k_m x) dx \right), \quad (6-a)$$

$$\int_S \Psi_{mn} \Psi_{mn}^* ds = C_{mn}^2 \int_0^W \cos^2(k_m x) dx \int_0^L \cos^2(k_n y) dy, \quad (6-b)$$

$$= C_{mn}^2 \frac{WL}{\delta_{om} \delta_{on}},$$

where

$$\delta_{op} = \begin{cases} 2, & p \neq 0 \\ 1, & p = 0 \end{cases}. \quad (7)$$

Substituting (4), (5), (6-a), and (6-b) into (3) gives

$$E_z(x, y) = \text{sinc}\left(\frac{m\pi d_s}{2W}\right) a_0(x, y) + \sum_{i=1}^q \text{sinc}\left(\frac{m\pi d_i}{2W}\right) E_z(x_i, y_i) a_i(x, y), \quad (8)$$

in which

$$a_i(x, y) = \begin{cases} \frac{jk_0 \eta_0}{ab} I_s \sum_{m, n} \frac{\delta_{om} \delta_{on}}{k^2 - k_{mn}^2} \cdot \cos(k_m x_s) \cos(k_n y_s) \cos(k_m x) \cos(k_n y), & i = 0 \\ \frac{jk_0 \eta_0}{ab} \frac{h}{Z_i} \sum_{m, n} \frac{\delta_{om} \delta_{on}}{k^2 - k_{mn}^2} \cdot \cos(k_m x_i) \cos(k_n y_i) \cos(k_m x) \cos(k_n y), & i \neq 0 \end{cases}. \quad (9)$$

Since the dimensions of the excitations in this cavity model satisfy  $d_s \ll W$  and  $d_i \ll W$  ( $i = 1, 2, 3, \dots$ ), the expression of (8) is simplified as

$$E_z(x, y) = a_0(x, y) + \sum_{i=1}^q E_z(x_i, y_i) a_i(x, y). \quad (10)$$

It is worth mentioning that both the general solution and the specific solutions of  $E_z$  in (10) still remain unknown at this stage, so it is necessary to construct a set of homogeneous equations to solve  $E_z$ .

By substituting  $(x_1, y_1)$ ,  $(x_2, y_2)$ ,  $\dots$ ,  $(x_q, y_q)$  into (10), respectively, a set of equations are thus established as

$$\begin{cases} a_0(x_1, y_1) + [a_1(x_1, y_1) - 1]E_z(x_1, y_1) \\ + a_2(x_1, y_1)E_z(x_2, y_2) + \dots + a_q(x_1, y_1)E_z(x_q, y_q) = 0 \\ a_0(x_2, y_2) + a_1(x_2, y_2)E_z(x_1, y_1) \\ + [a_2(x_2, y_2) - 1]E_z(x_2, y_2) + \dots + a_q(x_2, y_2)E_z(x_q, y_q) = 0 \\ \vdots \\ a_0(x_q, y_q) + a_1(x_q, y_q)E_z(x_1, y_1) \\ + a_2(x_q, y_q)E_z(x_2, y_2) + \dots + [a_q(x_q, y_q) - 1]E_z(x_q, y_q) = 0 \end{cases} \quad (11)$$

which is able to be written more concisely as a matrix equation below.

$$Ab = c, \quad (12-a)$$

$$A = \begin{bmatrix} a_1(x_1, y_1) - 1 & a_2(x_1, y_1) & \dots & a_q(x_1, y_1) \\ a_1(x_2, y_2) & a_2(x_2, y_2) - 1 & \dots & a_q(x_2, y_2) \\ \vdots & \vdots & \ddots & \vdots \\ a_1(x_q, y_q) & a_2(x_q, y_q) & \dots & a_q(x_q, y_q) - 1 \end{bmatrix}, \quad (12-b)$$

$$b = \begin{bmatrix} E_z(x_1, y_1) \\ E_z(x_2, y_2) \\ \vdots \\ E_z(x_q, y_q) \end{bmatrix}, \quad c = - \begin{bmatrix} a_0(x_1, y_1) \\ a_0(x_2, y_2) \\ \vdots \\ a_0(x_q, y_q) \end{bmatrix}. \quad (12-c)$$

As shown in (9),  $a_i(x, y)$  is expressed as the sum of infinite series, and the orders  $m$  and  $n$  in the series represent the operating modes excited in the cavity. Since the computational script solely supports the summation of finite series, the maximum order of calculated modes should be limited. Considering the fact that the modes excited within a rectangular patch are generally dominated by a single dominant mode (such as the  $\text{TM}_{01}$  mode), the influence of higher-order modes is quite limited, which merely contributes to a small quantity of the imaginary part of the input impedance. Consequently, a finite-order model with  $m \leq 5$  and  $n \leq 5$  is adopted in this work, which is sufficient to provide satisfactory accuracy. Thus, every element of matrixes  $A$  and  $c$  can be calculated.

On condition that the  $q \times q$  matrix  $A$  is full rank, the field distribution vector  $b$  can be solved in a breeze. As a result, the  $E_z$ -field value at arbitrary points within the cavity is obtained from expression (10).

In addition, it is also worth mentioning that the  $W$  and  $L$  sizes are slightly larger than the physical sizes  $W'$  and  $L'$  of the patch because of the fringing-field effect [28].

$$W = W' + 2\Delta l(L'), \quad L = L' + 2\Delta l(W'). \quad (13)$$

## B. Input impedance and radiation parameters

To obtain accurate input impedance and radiation efficiency of the patch antenna, its radiation and other loss should be included in the cavity model. Therefore, a wave number  $k_{eff}$  in the dielectric is introduced.

$$k_{eff} = k_0 \sqrt{\epsilon_r (1 - j \tan \delta_{eff})}. \quad (14)$$

The equivalent loss tangent  $\delta_{eff}$  derives from the radiation power, the conduction loss, the dielectric loss, and the surface-wave loss, which can be calculated by referring to the formulations in [28]. Because the resistor loss has already been included in the cavity functions, there is no need to calculate it separately.

Replacing each wave number  $k$  in the abovementioned equations with  $k_{eff}$ , the matrix equation (12-a) needs to be solved once more, since the  $E$ -field distribution gets changed. Then the input impedance at the feed point is acquired by

$$Z_{in} = -\frac{E_z(x_s, y_s)h}{I_s}. \tag{15}$$

Since the  $E$ -field distribution at the periphery has been acquired, the far fields are able to be calculated by the magnetic current model, in which the edges of the cavity are perceived as equivalent magnetic current sources [28].

### III. CALCULATION AND SIMULATION

#### A. $E$ -field distribution and input impedance

For reasons of observing the influence of resistor loading on input impedance, chip resistors of 200, 510, and 2000  $\Omega$  are respectively loaded. The  $E$ -field distribution of RLPA is calculated through the proposed cavity model. The calculated and simulated  $E$ -fields are depicted in Fig. 3, and they are coincident with the cosine distribution of  $TM_{01}$  mode. In particular, by reducing the loaded resistance, the overall magnitude is attenuated. This indicates that smaller resistance will result in more consumed power at load.

With the derived  $E$ -field distribution, the input impedance can be calculated. Figure 4 illustrates the

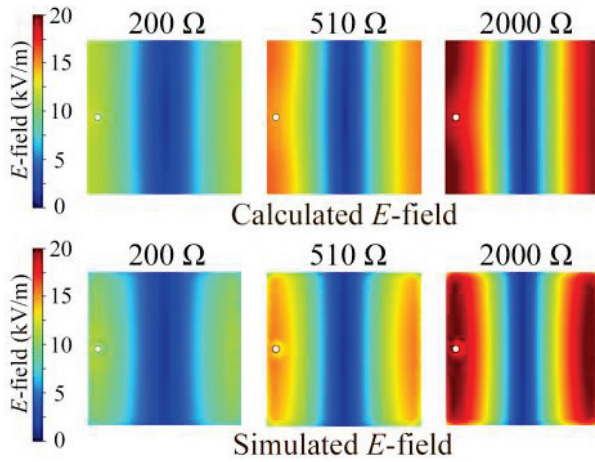


Fig. 3. Calculated and simulated  $E$ -field magnitude distributions of resistor-loaded patch antenna loaded with 200  $\Omega$ , 510  $\Omega$ , and 2000  $\Omega$  resistors. The feeding powers are fixed to 1 W.

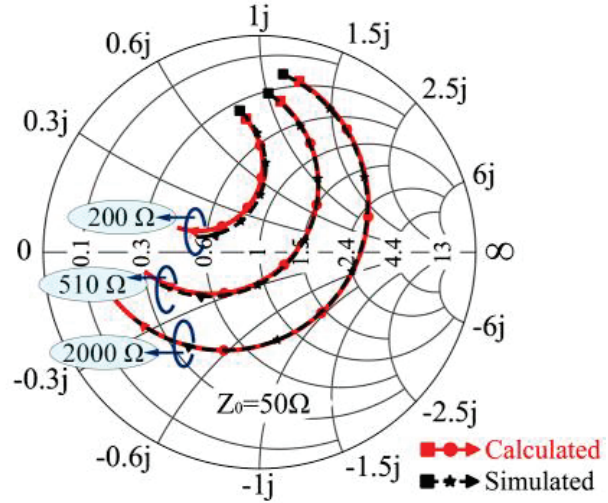


Fig. 4. Calculated and simulated input impedances in the Smith Chart under different loaded resistance within frequency range of 5.3 to 6.3 GHz.

comparison results, which show excellent agreement with each other.

Inexpensive commercial substrates, such as FR4, usually suffer from unstable permittivity, which may be harmful to the homogeneity of products in mass production. Fortunately, the enhanced bandwidth brought by resistor loading can well address this issue. Supposing the relative permittivity  $\epsilon_r$  of FR4 has a deviation of  $\Delta = 0.4$ , the reflection coefficients  $|S_{11}|$  with and without resistor loading are carried out with calculation and simulation, and they are compared in Fig. 5. It can be seen in Fig. 5 (a) that the  $\epsilon_r$  fluctuation has largely shifted the resonant frequency, and maximum  $|S_{11}|$  without resistors consequently increases to -1.8 dB in the band, which is almost total reflection. In contrast, as shown in Fig. 5 (b),

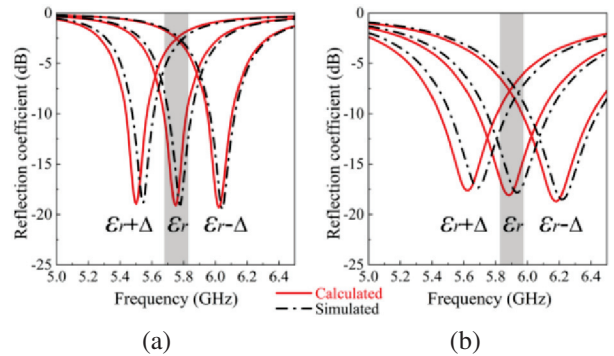


Fig. 5. Calculated and simulated reflection coefficients of the resistor-loaded patch antenna under different relative dielectric permittivity ( $\epsilon_r = 4.4$ ,  $\Delta = 0.4$ ): (a) Patch antenna without resistors and (b) patch antenna with 510  $\Omega$  resistors loaded.

the  $|S_{11}|$  of RLPA remains comparatively steady, and the maximum value is kept below -6 dB, which will not cause significant gain variation. As a result, even if a cheap substrate with unstable  $\epsilon_r$  is employed, RLPA can still maintain steady performance.

### B. Radiation gain and efficiency

The absorption of resistors will also affect the radiation gain and radiation efficiency of RLPA. The gain patterns under 200, 510, and 2000  $\Omega$  resistance loadings are calculated and simulated in Fig. 6. The maximum gain of RLPA gradually diminishes from 0.75 to -4.6 dB<sub>i</sub>, when the resistance reduces from 2000 to 200  $\Omega$ . The half-power beamwidth (HPBW) is kept constant. This is well coincident with the field distribution in Fig. 3. The power dissipation from radiating edges to loaded resistors primarily contributes to this phenomenon. Besides, the calculated gains are slightly lower than the simulated ones. This phenomenon derives from the delicate difference between calculated and simulated  $E$ -field distribution. As is shown in Fig. 3, the  $E$ -field magnitude at the corner in the simulation is slightly lower than the one in the calculation result, which results in reduction of power consumption caused by loaded resistors.

Further,  $R$ -Efficiency curves under different permittivity  $\epsilon_r$  are calculated and plotted in Fig. 7 (a). There is an overall tendency that the radiation efficiency decreases as the loaded  $R$  declines. The efficiency curve alters drastically when loaded  $R$  is small, whereas it becomes more insensitive when loaded  $R$  gets larger. Additionally, as  $\epsilon_r$  varies from 2.2 to 6.6, the overall radiation efficiency decreases, which evidently demonstrates that the increased substrate  $\epsilon_r$  is adverse for antenna radiation.

The curves of derived quality factor  $Q$  and bandwidth (BW) are concentrated as well in Fig. 7 (b). The  $Q$  factor remains relatively low when 200  $\Omega$  resistors are loaded, while it significantly rises as larger resistance is adopted. As a result of this increment, BW is narrowed down, which validates the inverse relationship between  $Q$  and BW. Further, when  $\epsilon_r$  increases from 2.2 to 6.6, the  $Q$  factor gradually gets higher, while BW gets even narrower in the meantime. These results will serve as a

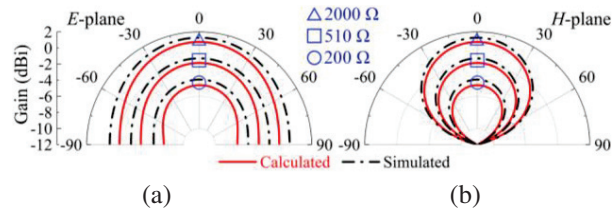


Fig. 6. Calculated and simulated gain patterns at 5.8 GHz of the infinite-ground model under different loaded resistance: (a) E-plane patterns and (b) H-plane patterns.

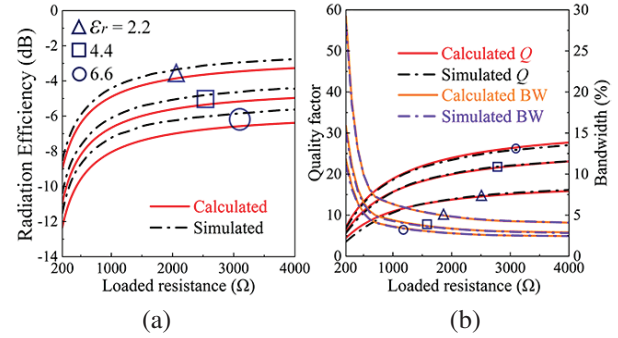


Fig. 7. Calculated and simulated results of (a) radiation efficiency and (b) quality factor and bandwidth for 10-dB return loss. The substrate thickness is 0.8 mm.

constructive guideline for the design of RLPAs according to the requirements.

From the calculated and simulated results above, it is known that the radiation efficiency becomes relatively lower when smaller resistors are loaded to the patch. But in the case of indoor motion radar applications, the superiority of the resistor-loading technique far outweighs its drawback. In practical situations, the recognition scope varies from 0.1 m to 10 m, thus a high agility of efficiency adjustment is required. The resistor-loading technique brings noteworthy design flexibility and extra bandwidth, which contribute to a better adaptability to the diverse application requirements.

## IV. MEASUREMENTS AND APPLICATIONS

The prototypes of the proposed RLPA with varied resistance are fabricated and measured. The photograph is shown in Fig. 8 (b). The measurements are conducted with Rohde & Schwarz ZVA vector network analyzer and a SY-16M near-field chamber.

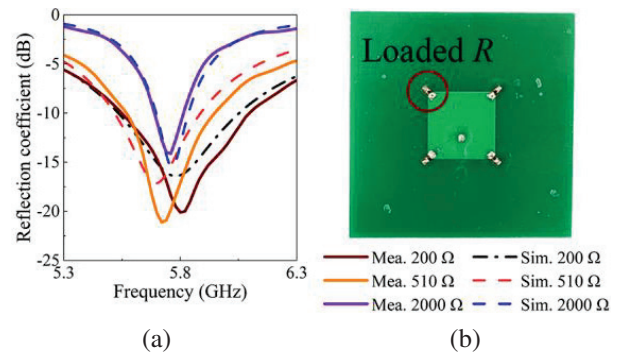


Fig. 8. (a) Simulated and measured reflection coefficient of the fabricated patch antennas; (b) photograph of the fabricated prototype.

Figure 8 (a) illustrates the measured and simulated reflection coefficients of RLPAs loaded with resistors of 200, 510, and 2000  $\Omega$ , while Fig. 9 illustrates the measured peak gain from 5.3 to 6.3 GHz. The simulated and measured results agree with each other. It is evident that both the impedance bandwidth and gain bandwidth are effectively enhanced. Figure 10 depicts the realized gain patterns of the prototypes in the *E*- and *H*-planes. The measured peak gains account for 2000, 510, and 200  $\Omega$  resistance are 1.39, -1.73 and -3.78 dBi, respectively, and the HPBW are kept unchanged.

An indoor motion radar module based on the proposed RLPA with flexible coverage area is developed, manufactured, and tested. The photograph of the radar module and the test facility is presented in Fig. 11. The transmitter and receiver are connected to two orthogonal feeds of the patch, which corresponds to two orthogonal polarizations. The radar module is horizontally installed with the wave beam directed at the dummy. The working principle is based on the Doppler effect of microwaves, and the detection distance is chiefly determined by the antenna gain, which is affected by loaded resistance.

The measured coverage range is also displayed. The recognition scopes of different radar modules range from 4.42 to 7.60 m, which could cover most of the domestic application demands of indoor motion radar. Our industrial partner has already put a series of microwave radar

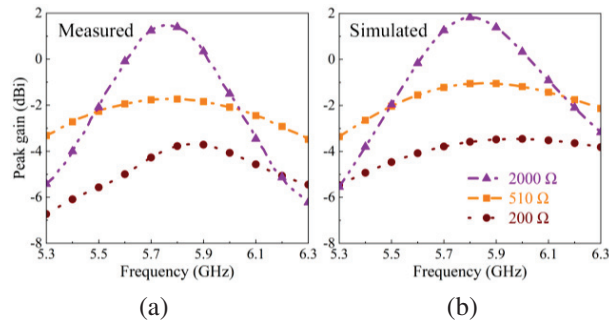


Fig. 9. Peak gain of the antenna prototypes in the frequency range of 5.3 to 6.3 GHz: (a) Measured results and (b) simulated results.

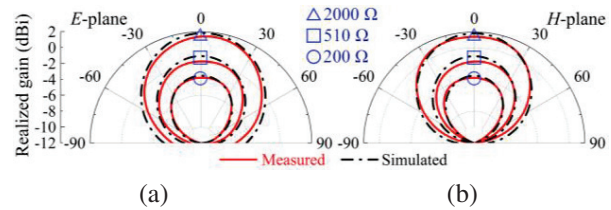


Fig. 10. The radiation patterns of the antenna prototypes at 5.8 GHz: (a) *E*-plane and (b) *H*-plane.

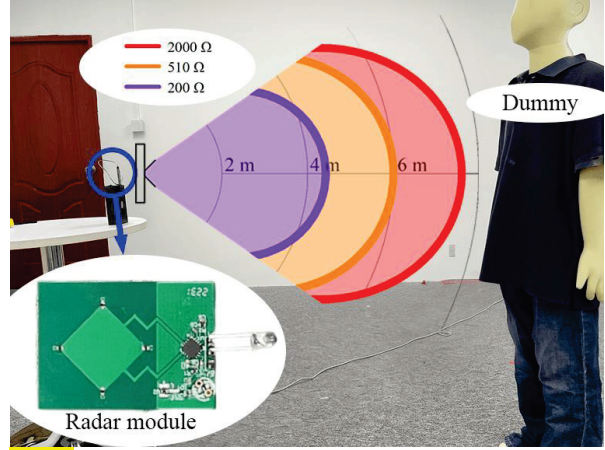


Fig. 11. Photograph of the test site and the fabricated radar module. The measured recognition scopes of indoor motion radar modules loaded with 200- $\Omega$ , 510- $\Omega$ , and 2000- $\Omega$  resistors are also illustrated. (The installation height is 0.9 m).

products with the proposed RLPA to the market, and a few gratifying application effects have been obtained from consumers.

**V. CONCLUSION**

In this article, a reformative cavity model of resistor-loaded patch antenna is proposed and comprehensively analyzed. The loaded resistors give rise to the reduction of *Q* factor, hence widen the bandwidth. The enhanced bandwidth provides better impedance-matching stability, which makes it possible that inexpensive material with unstable permittivity can be employed. The calculated results of the cavity model and the simulated results also present excellent agreement, which validates the precision of the proposed method. Further, in theory, the proposed cavity model is also applicable to other types of impedance loadings.

What is more, prototypes of RLPA with different gain levels are fabricated and measured, whose measured results solidly confirm the gain adjustment capacity. Besides, indoor motion radar modules employing the RLPA are manufactured and tested as well, and flexible coverage scope is achieved.

**ACKNOWLEDGMENT**

This work was supported in part by the Guangdong Provincial Department of Science and Technology, China, under Project No. 2020B1212030002, in part by the Shenzhen Science and Technology Innovation Commission, China, under Construction and Operation Project of Guangdong Provincial Key Laboratory and Guangdong-Hong Kong-Macau Joint Laboratory and Projects (No. JCYJ20190808115411853,

No. CJGJZD-2022051714240411, and No. KQTD2018-0412181337-494), in part by the Postgraduate Education Branch of the China Education Society of Electronics, and in part by the Guangdong Provincial Department of Education, China, under the Innovation Team Project No. 2020KCXTD004.

## REFERENCES

- [1] D. Deiana, E. M. Suijker, R. J. Bolt, A. P. M. Maas, W. J. Vlothuizen, and A. S. Kossen, "Real time indoor presence detection with a novel radar on a chip," *Proc. Int. Radar Conf.*, Lille, France, pp. 1-4, Oct. 2014.
- [2] B. Liu, M. Jian, Z. Lu, and R. Chen, "Indoor monitoring human movements using dual-receiver radar," *Proc. IEEE Radar Conf.*, pp. 0520-0523, May 2017.
- [3] E. Nyfors, "Industrial microwave sensors—A review," *Subsurface Sens. Technol. Appl.*, vol. 1, no. 1, pp. 23-43, Jan. 2000.
- [4] L. Jin, R. Cao, D. Li, and D. Wang, "Design of a new low-cost miniaturized 5.8 GHz microwave motion sensor," *Proc. IEEE Radar Conf.*, pp. 1-5, May 2021.
- [5] H.-T. Chen, "Compact circular microstrip antenna with embedded chip resistor and capacitor," *Proc. IEEE Antennas Propag. Soc. Int. Symp., Dig.*, pp. 1356-1359, June 1998.
- [6] P. Ferrari, N. Corrao, and D. Raully, "Miniaturized circular patch antenna with capacitors loading," *Proc. IEEE MTT-S Int. Microw. and Optoelectron. Conf.*, pp. 86-89, Oct. 2007.
- [7] G. Binoy, C. Aanandan, P. Mohanan, and K. Vasudevan, "Square microstrip slot antenna with chip capacitor loading for dual frequency operation," *Proc. IEEE Antennas Propag. Soc. Int. Symp., Dig.*, pp. 90-93, July 2001.
- [8] K. M. Luk, R. Chair, and K. F. Lee, "Small rectangular patch antenna," *Electron. Lett.*, vol. 34, no. 25, pp. 2366-2367, Dec. 1998.
- [9] M. Yang, Z. N. Chen, P. Y. Lau, X. Qing, and X. Yin, "Miniaturized patch antenna with grounded strips," *IEEE Trans. Antennas Propag.*, vol. 63, no. 2, pp. 843-848, Feb. 2015.
- [10] M. C. Liang, Y. L. Kuo, Y. M. Yen, and W. C. Lai, "Capacitor-loaded frequency control scheme for circular patch antenna," *Electron. Lett.*, vol. 36, no. 21, pp. 1757-1758, Oct. 2002.
- [11] M. Nishamol, V. Sarin, D. Tony, C. Aanandan, P. Mohanan, and K. Vasudevan, "Frequency and polarization tuning of a cross patch antenna using capacitive loading," *Proc. Int. Conf. Commun. Signal Process.*, pp. 92-96, Feb. 2011.
- [12] M. C. Laing, W. C. Lai, Y. M. Yen, and Y. L. Kuo, "A capacitor-loaded broadband circular patch antenna," *Proc. IEEE Antennas Propag. Soc. Int. Symp., Dig.*, pp. 302-304, July 2001.
- [13] I. Rouissi, J. M. Floc'H, H. Rmili, H. Trabelsi, and A. Sharaiha, "Study of reconfigurable square patch antenna using capacitive loading," *Proc. Loughb. Antennas Propag. Conf.*, pp. 263-266, Nov. 2014.
- [14] J. Li, B. He, L. Li, A. Zhang, J. Liu, and Q. H. Liu, "Capacitor-loaded circularly polarized annular-ring slotted microstrip patch antenna," *Proc. Int. Symp. Antennas, Propag. EM Theory*, pp. 13-15, Oct. 2016.
- [15] D. Schaubert, F. Farrar, A. Sindoris, and S. Hayes, "Microstrip antennas with frequency agility and polarization diversity," *IEEE Trans. Antennas Propag.*, vol. 29, no. 1, pp. 118-123, Jan. 1981.
- [16] D. L. Sengupta, "Resonant frequency of a tunable rectangular patch antenna," *Electron. Lett.*, vol. 20, no. 15, pp. 614-615, 1984.
- [17] S. S. Zhong and Y. T. Lo, "Single-element rectangular microstrip antenna for dual-frequency operation," *Electron. Lett.*, vol. 19, no. 8, pp. 298-300, Apr. 1983.
- [18] X. Zhang and L. Zhu, "Gain-enhanced patch antennas with loading of shorting pins," *IEEE Trans. Antennas Propag.*, vol. 64, no. 8, pp. 3310-3318, May 2016.
- [19] X. Zhang and L. Zhu, "Patch antennas with loading of a pair of shorting pins toward flexible impedance matching and low cross polarization," *IEEE Trans. Antennas Propag.*, vol. 64, no. 4, pp. 1226-1233, Apr. 2016.
- [20] K.-L. Wong and Y.-F. Lin, "Microstrip-line-fed compact microstrip antenna with broadband operation," *Proc. IEEE Antennas Propag. Soc. Int. Symp., Dig.*, pp. 1120-1123, June 1998.
- [21] A. Aoad, Z. Aydin, and E. Korkmaz, "Design of a tri band 5-fingers shaped microstrip patch antenna with an adjustable resistor," *Proc. IEEE Conf. Antenna Meas. Appl.*, pp. 1-4, Nov. 2014.
- [22] J.-H. Lu and K.-P. Yang, "Slot-coupled compact triangular microstrip antenna with lumped load," *Proc. IEEE Antennas Propag. Soc. Int. Symp., Dig.*, pp. 916-919, June 1998.
- [23] K.-L. Wong and Y.-F. Lin, "Small broadband rectangular microstrip antenna with chip-resistor loading," *Electron. Lett.*, vol. 33, no. 19, pp. 1593-1594, Sep. 1997.
- [24] S. V. Hum, J. Chu, R. H. Johnston, and M. Okoniewski, "Improving the bandwidth of microstrip patch antennas using resistive loading," *Proc. IEEE Antennas Propag. Soc. Int. Symp., Dig.*, pp. 276-279, June 2003.

- [25] J.-H. Lu, C.-L. Tang, and K.-L. Wong, "Slot-coupled compact broadband circular microstrip antenna with chip-resistor and chip-capacitor loadings," *Microwave Opt. Technol. Lett.*, vol. 18, no. 5, pp. 345-349, Dec. 1998.
- [26] Y. Lo, D. Solomon, and W. Richards, "Theory and experiment on microstrip antennas," *IEEE Trans. Antennas Propag.*, vol. 27, no. 2, pp. 137-145, Mar. 1979.
- [27] W. Richards, Yuen Lo, and D. Harrison, "An improved theory for microstrip antennas and applications," *IEEE Trans. Antennas Propag.*, vol. 29, no. 1, pp. 38-46, Jan. 1981.
- [28] R. Garg, P. Bhartia, I. Bahl, and A. Ittipiboon, *Microstrip Antenna Design Handbook*, pp. 267-268, Norwood, MA, USA: Artech House, 2001.



**Shu-Wei Yu** was born in Hangzhou, Zhejiang, China. He received the B.Eng. degree in electronic information engineering from Zhejiang University in 2016. Currently, he is pursuing the M.Eng. degree in communication engineering in Shenzhen University. His research mainly focuses on impedance loaded patch antennas and circularly-polarized antennas.



**Xiao Zhang** was born in Gaozhou, Guangdong, China. He received the B.Eng. degree in information engineering and the M.Eng. degree in communication and information systems from the South China University of Technology, Guangzhou, China, in 2011 and 2014, respectively, and the Ph.D. degree in electrical and computer engineering from University of Macau, Macau, SAR, China, in 2017.

From September 2012 to August 2014, he was a research assistant with Comba Telecom Systems Limited, Guangzhou, China. From January 2018 to March 2018, he was a research fellow with the Antenna and Electromagnetic-Wave Laboratory in University of Macau, Macau, SAR, China. In 2018, he joined the College of Electronics and Information Engineering, Shenzhen University, Shenzhen, China, where he is currently an associate professor. His research interests include high-gain antennas, wideband antennas, circularly-polarized antennas, terminal antennas, filtering antennas, reflectarray, and characteristic mode analysis.



**Qiong-Sen Wu** received the B.Eng. degree in information engineering and the M.Eng. degree in electromagnetism and microwave engineering from South China University of Technology, Guangzhou, China, in 2011 and 2014, respectively, and the Ph.D. degree in electrical and computer engineering from the University of Macau, Macau, SAR, China, in 2018.

He joined the Antenna and Electromagnetic-Wave Laboratory in University of Macau, Macau, SAR, China, as a research fellow in May 2018. He is currently an associate professor with the School of Integrated Circuits, Guangdong University of Technology. His current research interests include microwave circuits and planar antennas with improved functionalities. He also serves as a reviewer for several journals, including the *IEEE Transactions on Antennas and Propagation* and the *IEEE Transactions on Microwave Theory and Techniques*.



**Lei Zhu** (Fellow, IEEE) received the B.Eng. and M.Eng. Degrees in radio engineering from the Nanjing Institute of Technology (now Southeast University), Nanjing, China, in 1985 and 1988, respectively, and the Ph.D. Degree in electronic engineering from the University of Electro-Communications, Tokyo, Japan, in 1993.

From 1993 to 1996, he was a Research Engineer with Matsushita-Kotobuki Electronics Industries Ltd., Tokyo, Japan. From 1996 to 2000, he was a Research Fellow with the École Polytechnique de Montréal, Montréal, QC, Canada. From 2000 to 2013, he was an Associate Professor with the School of Electrical and Electronic Engineering, Nanyang Technological University, Singapore. He joined the Faculty of Science and Technology, University of Macau, Macau, China, as a Full Professor in August 2013, was promoted as a Distinguished Professor in December 2016, and then as a Chair Professor in October 2023. From August 2014 to August 2017, he served as the Head of Department of Electrical and Computer Engineering, University of Macau.

So far, he has authored or coauthored more than 810 papers in international journals and conference proceedings. His papers have been cited more than 16,600 times with the H-index of 63 (source: Scopus). His research interests include microwave circuits, antennas, periodic structures, transmitting/reflecting surfaces and computational electromagnetics.

Dr. Zhu was the Associate Editors for the IEEE TRANSACTIONS ON MICROWAVE THEORY AND TECHNIQUES (2010-2013) and IEEE MICROWAVE AND WIRELESS COMPONENTS LETTERS (2006-2012). He served as a General Chair of the 2008 IEEE MTT-S International Microwave Workshop Series on the Art of Miniaturizing RF and Microwave Passive Components, Chengdu, China, and a Technical Program Committee Co-Chair of the 2009 Asia-Pacific Microwave Conference, Singapore. He served as the member of IEEE MTT-S Fellow Evaluation Committee (2013-2015), and as the member of IEEE AP-S Fellows Committee (2015-2017). He was the recipient of the 1997 Asia-Pacific Microwave Prize Award, the 1996 Silver Award of Excellent Invention from Matsushita-Kotobuki Electronics Industries Ltd., the 1993 Achievement Award in Science and Technology (first prize) from the National Education Committee of China, the 2020 FST Research Excellence Award from the University of Macau, the 2020 and 2022 Macao Natural Science Awards (Second Prize) from the Science and Technology Development Fund (FDCT), Macau, and the 2024 IEEE MTT-S Microwave Application Award. He was elevated to the IEEE Fellow in November, 2011.



**Tao Yuan** received the B.E. degree in electronic engineering and the M.E. degree in signal and information processing at Xidian University, Xi'an, Shaanxi, China, in 1999 and 2003, respectively, and the Ph.D. degree in electrical and computer engineering at National University of Singapore, Singapore, in 2009.

He was a visiting scholar at University of Houston (2007-2008). He is now a distinguished professor (2016-till now) with the College of Electronics and Information Engineering at Shenzhen University, Shenzhen, Guangdong, China. He is the director of the Guangdong Provincial Mobile Terminal Microwave and Millimeter-Wave Antenna Engineering Research Center and the deputy director of the Guangdong-Hong Kong Joint Labora-

tory for Big Data Imaging and Communication. He is a visiting professor (2021-till now) at Chongqing University, China, and an adjunct professor (2021-till now) at Fudan University, China. He is leading a group of over 70 members performing fundamental and application studies in the areas of RF/microwave/millimeter-wave frontend devices, antennas, ICs, and advanced manufacturing techniques for microwaves and microelectronics. He has Pled/co-Pled over 20 governmental and entrepreneurial research projects on 5G MIMO antennas (arrays), transmission lines, and packaged antennas for smart IoT/mobile terminals. His current research interests include design and implementation of novel RF frontend chips/modules and integrated devices/antennas/circuits for 5G/6G applications. He has advised over 40 graduate students and has authored/co-authored over 150 international journal and conference publications. He is holding over 100 licensed CN patents. He has co-authored 2 books: *Antenna Design for 5G Mobile Terminals* (Posts & Telecom Press, 2021) and *Practical Design and Development of FPGA—Based on Xilinx and Verilog HDL* (Publishing House of Electronics Industry, 2023).

Dr. Yuan is a member of the IEEE Antennas and Propagation Society, IEEE Microwave Theory and Techniques Society, and the China Communications Standards Association. He is a senior member of the Chinese Institute of Electronics (CIE) and the China Institute of Communications (CIC). He serves as a reviewer for several international journals and conferences and serves as a Guest Editor for *Coatings*. He is the organizing committee member of APMC2020, Mar-For (2021, 2022) (TPC member), and CSRSWTC2021 (general chair). He serves as a consultant for several research institutions and ICT companies in China. He received numerous teaching, entrepreneurial, and talent awards in China. He is the recipient of the Outstanding Individual Award (2018), the Outstanding Graduate Student Advisor (2021), the Excellent Undergraduate Thesis Instructor (2022), and the Undergraduate Teaching Outstanding Contribution Award (2022) from Shenzhen University and the co-recipient of the CIC Science and Technology Second Place Award (2020) and the Excellent Teaching Management Team of Tencent Team Award (2022). His students and group members have received over 150 scholarships/awards in China and international conferences, including the CSRSWTC2021 Best Paper Award and the IEEE RWW2022 student paper competition finalist.



**Xian-Qin Hu** received the B.E. degree in chemical engineering and technology from Anhui University of Science and Technology in 2006. He has been engaging in the research and development of new technologies, new materials, new products, and new processes for printed circuit

boards at Avary Holding (Shenzhen) Co., Ltd.

He is currently the research and development manager of the Avary Holding R&D Center (Shenzhen), and director of the Guangdong Flexible Printed Electronics Engineering Technology Research Center.

# Four-way SIW Filtering Power Divider with In- and Out-of-phase Characteristics and Large Power Division Ratio

Minghan Shu<sup>1</sup>, Nengcai Huang<sup>1</sup>, Qiyue Gao<sup>1</sup>, Chenxin Ma<sup>1</sup>, and Xin Zhou<sup>1,2,\*</sup>

<sup>1</sup>School of Electrical and Automation Engineering  
Nanjing Normal University, Nanjing, China

<sup>2</sup>Faculty of Science and Technology  
University of Macau, Macau, China

\*Correspondence: zhouxin5537@163.com

**Abstract** – A novel four-way substrate integrated waveguide (SIW) filtering power divider (FPD) with in-phase and out-of-phase characteristics and a large power division ratio (PDR) is presented in this work. The frequency selection and power division functions are effectively realized by employing SIW resonators at the bottom layer and at microstrip sections at the top layer, respectively. Four microstrip lines coupled with SIW cavity through a slotline realize in-phase and two out-of-phase output characteristics and a large PDR of 7:1. To verify the design method, a four-way prototype with PDR of 7:7:1:1 is designed, fabricated, and measured. Results exhibit good filtering performance, large power division ratio, and in-phase and out-of-phase characteristics.

**Index Terms** – Four-way, filtering power divider (FPD), in-phase - out-of-phase, power division ratio (PDR), substrate integrated waveguide (SIW).

## I. INTRODUCTION

In modern wireless system, as two key passive components in wireless communication system, power dividers and filters are usually used in a cascaded way. This undoubtedly increases the circuit size and loss. In recent years, a high-integration design method, namely filtering power divider (FPD), has been widely developed. It can not only achieve the frequency selection function of the filter but also realize the power division of the power divider. According to its response type, it can be divided into in-phase FPD [1–4] and out-of-phase FPD [5–8]. In addition, unequal FPDs also become particularly important because their specific unequal power division ratio (PDR) can enable the array to obtain better directional performance in beamforming systems [9].

On the other hand, as an important part of substrate integrated circuits (SICs), substrate integrated waveguide (SIW) has attracted extensive attention from scholars due to its low cost, low loss, high integration, high power capacity, and so on [10]. A series of SIW-based FPDs

is proposed, such as dual-band FPD on SIW triangular cavities [11], wideband four-way design based on SIW loaded square patch resonator [12], three-way FPD with adjustable PDR [13], and so on. Nevertheless, very few designs can realize in-phase and out-of-phase output at the same time and with a large PDR.

In this work, a novel four-way SIW FPD with large PDR of 7:7:1:1 is presented. Specifically, two ways are in-phase output while other two ways are out-of-phase output, with a 7:1 PDR of in-phase and out-of-phase output. The frequency selection and power division functions are effectively realized by employing SIW resonators and microstrip sections, respectively. Four microstrip lines coupled with SIW cavity through a slotline realize two in-phase and two out-of-phase output characteristics and a large PDR of 7:1. To verify the method, a prototype is designed, fabricated, and measured. The results show good filtering performance, large power division ratio, and in-phase and out-of-phase characteristics.

## II. DESIGN AND ANALYSIS

The physical structure of proposed four-way SIW FPD is shown in Fig. 1. It consists of two coupled SIW resonators at the bottom layer, a slotline at the middle layer, and four microstrip lines at the top layer. Specifically, the two SIW cavities resonate at  $TE_{101}$  mode and are coupled through a coupling window to realize second-order filtering performance. Then, the energy is transmitted to the top layer through the slotline and output through four microstrip lines. The slotline is set at the strong magnetic field of the SIW cavity to realize the transmission from the bottom layer to the top layer. Figure 2 shows the coupling diagram of proposed four-way SIW FPD.

According to the above design concept, a four-way SIW FPD operating at 13 GHz with PDR of 7:7:1:1 is designed. Firstly, the size of the SIW cavity can be

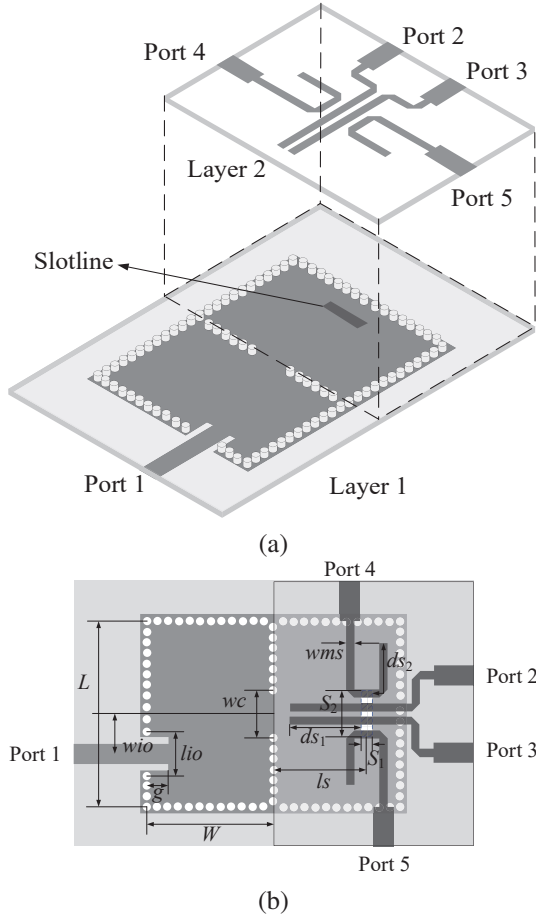


Fig. 1. Structures of proposed four-way SIW FPD: (a) Three-dimension view and (b) planar layout.

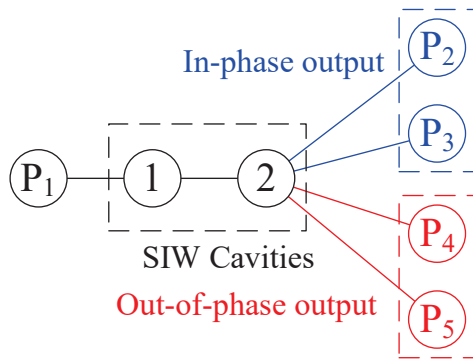


Fig. 2. Coupling diagram of proposed four-way SIW FPD.

calculated according to the formulas

$$f_{TE_{m0q}} = \frac{c}{2\sqrt{\epsilon_r \mu_r}} \sqrt{\left(\frac{m}{w_{\text{eff}}}\right)^2 + \left(\frac{q}{l_{\text{eff}}}\right)^2}, \quad (1)$$

$$w_{\text{eff}} = w_1 - \frac{d^2}{0.95p}, \quad l_{\text{eff}} = l_1 - \frac{d^2}{0.95p}, \quad (2)$$

where  $w_1$  and  $l_1$  represent the design width and length of the SIW cavity and  $w_{\text{eff}}$  and  $l_{\text{eff}}$  represent the effective width and length, respectively.  $d$  is the diameter of the vias,  $p$  is the distance between the adjacent vias,  $c$  is the speed of light in vacuum, and  $\epsilon_r$  is the relative permittivity of substrate.

The external quality factor of the input port and the coupling coefficient between the SIW resonators can be calculated according to the formulas

$$Q_{es} = \pi f_i \cdot \tau_{S_{11}}(f_i)/2, \quad (3)$$

$$K = \frac{f_1^2 - f_2^2}{f_1^2 + f_2^2}, \quad (4)$$

where  $\tau_{S_{11}}(f_i)$  is the group delay of  $|S_{11}|$  at resonance  $f_i$ , and  $f_1$  and  $f_2$  denote the higher and lower resonant frequencies of two coupled, respectively. Figure 3 shows the graphs of the external quality factor  $Q_{es}$  and the coupling coefficient  $K$  as a function of different parameters.

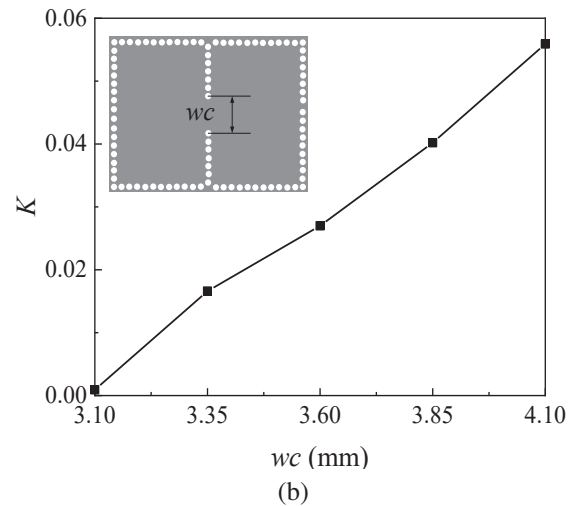
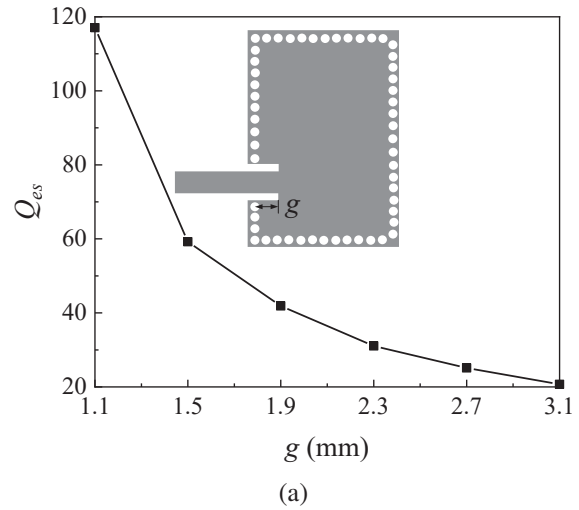


Fig. 3. Extracted external quality factor: (a)  $Q_{es}$  and coupling coefficient and (b)  $K$ .

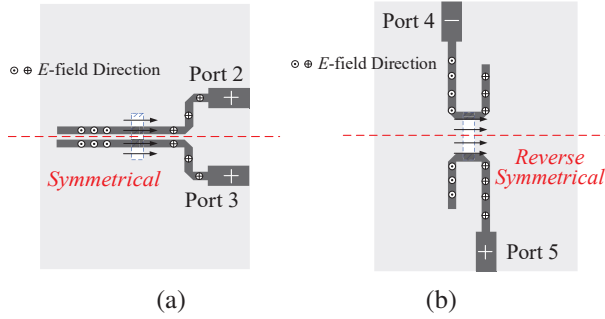


Fig. 4. Analysis of phase characteristic of output ports: (a) In-phase output and (b) out-of-phase output.

The phase characteristics of the output ports can be analyzed as follows. As shown in Fig. 4 (a), microstrip lines connected to output ports 2 and 3 are symmetrical about the slotline, so the in-phase characteristic can be obtained at output ports 2 and 3, while microstrip lines connected to output ports 4 and 5 are reverse symmetrical about the slotline, shown in Fig. 4 (b), so the out-of-phase characteristic can be obtained at output ports 4 and 5 [14]. It is worth noting that by adjusting  $Q_{eL}$ , that is, the parameter  $ds_1$  and  $ds_2$ , the PDR of in-phase output and out-of-phase output can be controlled. The  $Q_{eL}$  of each output port can be obtained as [15]

$$Q_{eLi} = \frac{\alpha_1 + \alpha_2 + \dots + \alpha_N}{\alpha_i} Q_s, \quad (5)$$

where  $N = 4$ , and  $\alpha_1, \alpha_2, \alpha_3$ , and  $\alpha_4$  represent the dissipated power of each output port. The division ratio can be adjusted by tuning the  $Q_{eL}$  ratio of the four output ports. In order to more clearly demonstrate the adjustment process of the PDR, Fig. 5 depicts the PDR changes under different  $Q_{eL}$ , that is, different parameters  $ds_1$ , of output ports.

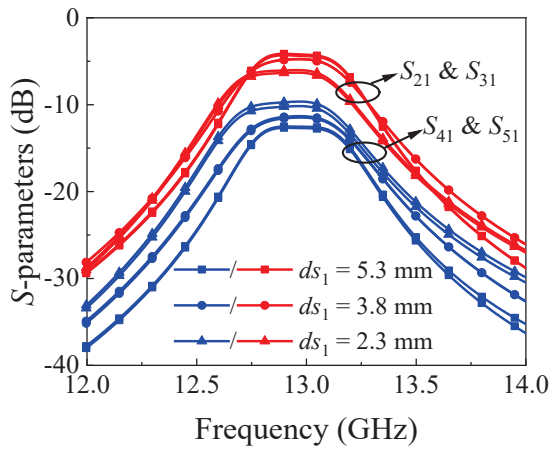


Fig. 5. The PDR changes under different parameters  $ds_1$ .

### III. SIMULATED AND MEASURED RESULTS

To verify the design method, a prototype operating at 12.96 GHz with PDR of 7:7:1:1 is fabricated on Rogers 5880 substrate with the relative dielectric constant of 2.2 and thickness  $h = 0.508$  mm. The final dimension of the proposed four-way SIW FPD is determined as follows:  $L = 14$ ,  $W = 9.5$ ,  $wio = 3$ ,  $lio = 2.55$ ,  $g = 1.6$ ,  $wc = 3.6$ ,  $wms = 0.6$ ,  $ls = 7$ ,  $S_1 = 0.8$ ,  $S_2 = 3.3$ ,  $ds_1 = 5.3$ ,  $ds_2 = 5.05$  (all units: mm). The whole area of fabricated FPD is around  $1.2 \lambda_g \times 0.9 \lambda_g$ , where  $\lambda_g$  is the guided wavelength at 13 GHz.

According to the PDR of 7:7:1:1,  $S_{21}$ ,  $S_{31}$ ,  $S_{41}$ , and  $S_{51}$  are -3.6 dB, -3.6 dB, -12.04 dB, and -12.04 dB. As shown in Fig. 6 (a), we can see that in the machining model the input port is off center, this is mainly to achieve impedance matching of the input port, so as to adjust the return loss of  $S_{11}$ . And the measured return loss (RL) is better than 16.6 dB, and the minimum insertion loss (IL) is 0.8 dB (not including 7:7:1:1 power

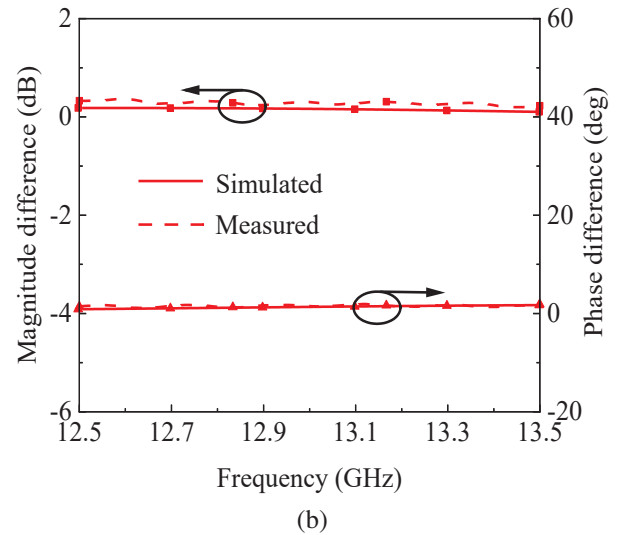
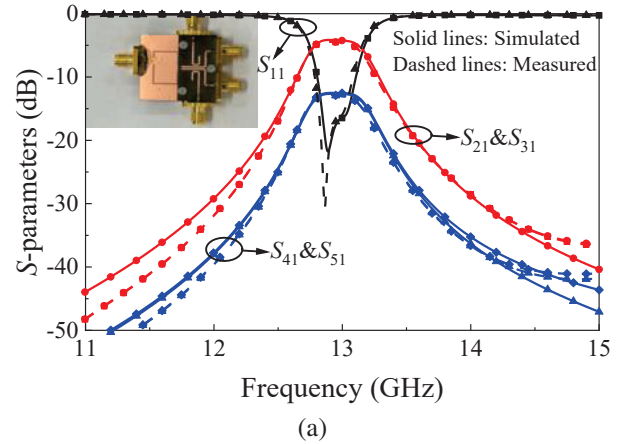


Fig. 6. Continued

Table 1: Comparisons with other reported works

Refs.	CF (GHz)	3-dB FBW (%)	Size ( $\lambda g^2$ )	IL (dB)	Order	Number of Ways	Power Division Ratio	Phase
[4]	4.82	11.6	0.469	2.0	2	2	1:1	In-phase
[11]	8.3	9.6	1.91	1.5	2	2	1:1	In-phase
[12]	3.55	21.3	1.3	2.0	2	4	1:1:1:1	In-phase
[13]	11.8	5.9	1.28	1.0	2	3	1:1:1.5	In-phase
This work	12.96	3.96	1.08	0.8	2	4	7:7:1:1	In-phase & Out-of-phase

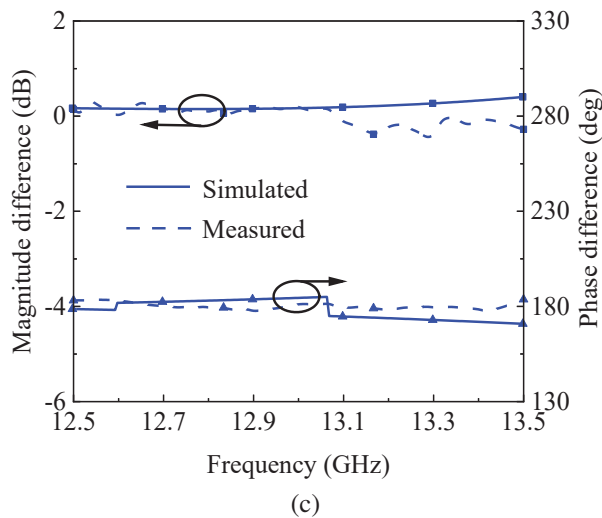


Fig. 6. Simulated and measured results of proposed four-way SIW FPD: (a)  $S$ -parameters, (b) magnitude difference and phase difference of in-phase case, and (c) magnitude difference and phase difference of out-of-phase case.

division loss). The measured center frequency (CF) is 12.96 GHz, and the 3 dB fractional bandwidth (FBW) is 3.96%. As shown in Figs. 6 (b) and (c), the magnitude difference between in-phase output ports is 0.3 dB, while between out-of-phase output ports is 0.45 dB. The phase difference between in-phase output ports is 1.8 degrees, while between out-of-phase output ports is 4.9 degrees. The simulated results show most consistency with the measured results, but there are some differences between the measured and simulated results in our article, mainly because there are certain errors in the processing process, and the SMA plug has a certain degree of wear during testing, both of which lead to the difference.

In addition, in order to highlight the advantages of our design, Table 1 lists the comparisons between this work and other reported works. It is clear that the proposals in this work achieves a larger PDR and both in-phase and out-of-phase response.

#### IV. CONCLUSION

In this work, a four-way SIW FPD with in-phase and out-of-phase characteristics and large PDR is presented. A prototype with PDR of 7:7:1:1 is designed, fabricated, and measured. The results show good filtering performance, phase characteristic, and large PDR. It is believed that the proposal has a good prospect in beamforming systems.

#### ACKNOWLEDGMENT

This work was supported in part by Practice Innovation Program of Jiangsu Province under Grant SJCX23.0590. (Corresponding author: Xin Zhou)

#### REFERENCES

- [1] A. Khan and M. K. Mandal, "Miniaturized substrate integrated waveguide (SIW) power dividers," *IEEE Microw. Wireless Compon. Lett.*, vol. 26, no. 11, pp. 888-890, Nov. 2016.
- [2] H. Zhu, A. M. Abbosh, and L. Guo, "Wideband four-way filtering power divider with sharp selectivity and wide stopband using looped coupled line structures," *IEEE Microw. Wireless Compon. Lett.*, vol. 26, no. 6, pp. 413-415, June 2016.
- [3] C. Zhu, J. Xu, and W. Wu, "Microstrip four-way reconfigurable single/dual/wideband filtering power divider with tunable frequency, bandwidth, and PDR," *IEEE Trans. Ind. Electron.*, vol. 65, no. 11, pp. 8840-8850, Nov. 2018.
- [4] X. Wang, X.-W. Zhu, L. Tian, P. Liu, W. Hong, and A. Zhu, "Design and experiment of filtering power divider based on shielded HMSIW/QMSIW technology for 5G wireless applications," *IEEE Access*, vol. 7, pp. 72411-72419, 2019.
- [5] X. Wang, X.-W. Zhu, C. Yu, P.-F. Liu, and X.-S. Shi, "Design of the quarter-mode substrate integrated waveguide in-phase and out-of-phase filtering power divider," *2018 IEEE MTT-S International Wireless Symposium (IWS)*, Chengdu, China, pp. 1-3, 2018.
- [6] X. Y. Zhang, X. F. Liu, Y. C. Li, W. L. Zhan, Q. Y. Lu, and J. X. Chen, "LTCC out-of-phase filtering power divider based on multiple broadside coupled

lines," *IEEE Trans. Compon., Packag. Manuf. Technol.*, vol. 7, no. 5, pp. 777-785, May 2017.

- [7] X. Wang, W. W. Choi, J. Wang, and W. Wu, "Wideband out-of-phase filtering power divider with high selectivity," *2018 Asia-Pacific Microwave Conference (APMC)*, Kyoto, Japan, pp. 417-419, 2018.
- [8] X. Wang, W.-W. Choi, J. Wang, L. Zhu, and W. Wu, "Wideband out-of-phase filtering power divider with ultra-wide isolation band," *2019 IEEE MTT-S International Wireless Symposium (IWS)*, Guangzhou, China, pp. 1-3, 2019.
- [9] S. Mukherjee and A. Biswas, "Implementation of broadband unequal power divider using substrate integrated waveguide (SIW) technology," *IEEE MTT-S Int. Microwave RF Conf. (IMaRC)*, pp. 177-179, 2015.
- [10] X. Zhou, J. Zheng, W. Tang, and J. Yang, "SIW filter with adjustable number of passbands using assembled multimode resonant PCBs," *IEEE Trans. Circuits and Syst. II, Exp. Briefs*, vol. 69, no. 8, pp. 3386-3389, Aug. 2022.
- [11] Y. Wang, C. Zhou, K. Zhou, and W. Wu, "Compact dual-band filtering power divider based on SIW triangular cavities," *Electron. Lett.*, vol. 54, no. 18, pp. 1072-1074, Sep. 2018.
- [12] M. Yang, J. Wang, X. Wang, and W. Wu, "Design of wideband four-way filtering power divider based on SIW loaded square patch resonator," *Electron. Lett.*, vol. 59, no. 7, pp. 389-391, Apr. 2019.
- [13] G. Zhang, Y. Liu, E. Wang, and J. Yang, "Multilayer packaging SIW three-way filtering power divider with adjustable power division," *IEEE Trans. Circuits and Syst. II, Exp. Briefs*, vol. 67, no. 12, pp. 3003-3007, Dec. 2020.
- [14] N. Seman and M. Bialkowski, "Microstrip-slot transition and its applications in multilayer microwave circuits," *Passive Microwave Components and Antennas*, ed. V. Zhurbenko, pp. 247-266, Apr. 2010.
- [15] W. Yu and J.-X. Chen, "Multiport in-phase/antiphase power dividing network with bandpass response based on dielectric resonator," *IEEE Trans. Microw. Theory Techn.*, vol. 66, no. 11, pp. 4773-4782, 2018.



**Minghan Shu** was born in Sichuan, China, in 1996. He is currently working toward the M.Sc. degree in Nanjing Normal University (NNU), Nanjing, China. His current research interests include microwave/millimeter-wave circuits and matrix algorithms.



**Nengcai Huang** was born in Jiangxi, China, in 1999. He is currently working toward the M.Sc. degree in Nanjing Normal University (NNU), Nanjing, China. His research interest is RF circuit synthesis and design.



**Qiyue Gao** was born in Jiangsu, China, in 2003. She is currently pursuing the B.E. degree in electrical engineering and automation at Nanjing Normal University (NNU), Nanjing, China. Her current research interests include multifunctional microwave passive circuits

and antennas.



**Chenxin Ma** was born in Changzhou, China, in 2000. He is currently pursuing the M.S. degree in Nanjing Normal University (NNU), Nanjing, China. His current research interests include microwave/millimeter-wave circuits and antennas.



**Xin Zhou** was born in Henan, China, in 1998. He received the M.S. degree from the Nanjing Normal University (NNU), Nanjing, China, in 2023. He is currently pursuing the Ph.D. degree in electrical and computer engineering at the University of Macau (UM), Macao SAR, China. His current research interests include microwave/millimeter-wave circuits and antennas.

# A Low-power, High-gain and Excellent Noise Figure GaN-on-SiC LNA Monolithic Microwave Integrated Circuit (MMIC) operating at *Ka*-band for 5G/6G Application

Zhou Dai<sup>1,2</sup>, Chunyu Li<sup>1</sup>, Junda Yan<sup>2</sup>, Tiancheng Zhang<sup>1</sup>, and Huaguang Bao<sup>1</sup>

<sup>1</sup>School of Microelectronics (School of Integrated Circuits)  
Nanjing University of Science and Technology, Nanjing, China

<sup>2</sup>Nanjing Electronic Devices Institute  
Nanjing, China  
\*daizhou1986@163.com

**Abstract** – A 25-40 GHz monolithic low-noise amplifier (LNA) is designed and fabricated with the 100 nm gallium nitride on silicon carbide (GaN-on-SiC) technology. This four-stage-cascade monolithic LNA performs a low DC power consumption of 150 mW and noise figure of 1.6-2.2 dB. Moreover, the gain of 34-37 dB with the continuous wave of more than 2 W over 24 hours can be achieved covering the operating bandwidth. Hence, this state-of-art LNA possesses a great potential to be directly integrated with GaN power amplifiers and other microwave components to realize the high-integration, high-reliability, and high-power RF front-end.

**Index Terms** – Gallium nitride on silicon carbide (GaN-on-SiC), high gain, low-noise amplifier (LNA), low DC power consumption, optimal noise figure.

## I. INTRODUCTION

To deal with the serious loss and high packaging cost of the transmitter and receiver millimeter-wave (mm-Wave) front-end, monolithic microwave integrated circuit (MMIC) technique is extended to the mm-Wave frequency range and is fabricated the components on the same chip [1]. GaN material has the advantages of wide band gap and high electron mobility [2], such that a GaN low-noise amplifier (LNA) can achieve more superior breakdown resistance and higher frequency characteristics than GaAs devices. Recently, several GaN LNAs operating at *Ka*-band have been recorded [1, 3–6]. Depending on the substrate material, GaN LNAs are mainly classified into two types, one with GaN-on-Si process [1, 3, 4] and the other with GaN-on-SiC process [5–7]. The study of discrete components on Si substrate has been mature, leading to the conclusion that the GaN LNA with SiC substrate is not completely superior in terms of performance compared to the GaN LNA with Si

substrate. The SiC substrate with high thermal conductivity allows for efficient dissipative power density, and no leakage problem as with Si substrate, which further guarantees the robustness of GaN LNA [6–7]. Moreover, with the requirement of high speed, high power, and high detection accuracy for RF front-ends, it is imperative to develop GaN LNA with wider bandwidth, lower noise, and lower power consumption.

In this work, a self-developed 0.1  $\mu\text{m}$  T-Gate high electron mobility transistor with ultra-thin barrier is adopted to fabricate a 25-40 GHz wideband GaN-on-SiC LNA. The GaN LNA demonstrates a high gain of 34-37 dB, an excellent DC power consumption of 150 mW, and low noise figure (NF) of 1.6-2.2 dB, simultaneously, which enables unparalleled performances in *Ka*-band.

## II. LNA DESIGN

In this section, the process of GaN HEMT and the design of the GaN LNA MMIC is described in detail.

### A. GaN HEMT

The GaN high-electron-mobility transistors (HEMTs) are prepared with a self-developed ultra-thin barrier. The AlN/GaN/AlGaIn double heterojunction epitaxy structure is grown on SiC substrate by metalorganic chemical vapor deposition (MOCVD) [8]. Due to the strong polarization effect of AlN, the energy band difference of AlN/GaN is large, so a high concentration of two-dimensional electron gas (2-DEG) can be formed at the interface of the two materials [9–12]. The negative polarization charge on the back of AlN increases the energy band of the AlGaIn barrier, so that the probability of 2-DEG entering AlGaIn is greatly reduced. In this way, the disorder scattering in the alloy is reduced, the mobility of the 2-DEG is increased, and the device noise is improved. The Hall test shows that the heterojunction material has a 2-DEG concentration of  $1.1 \times 10^{13} \text{ cm}^{-2}$

and mobility of up to  $1550 \text{ cm}^2/(\text{V} \cdot \text{s})$ . A 100 nm T-gate with low parasitic impedance is fabricated using ion beam direct writing in combination with ultrathin gate dielectric passivation. Schottky contacts play a decisive role in device reliability and performance. In order to improve the Schottky barrier, reduce the gate leakage current, and improve the noise properties of the device, a high-barrier Ni-gate structure is used. The stability of the Schottky contact is improved by a high-temperature thermal treatment.

## B. LNA

LNA is designed with four-stage-cascade amplifiers and self-biased negative feedback structure. The total NF of LNA can be written as [13]

$$F = F_1 + \frac{F_2 - 1}{G_1} + \frac{F_3 - 1}{G_1 G_2} + \frac{F_4 - 1}{G_1 G_2 G_3}, \quad (1)$$

where  $F_1, F_2, F_3, F_4$ , and  $G_1, G_2, G_3$  are NF of level 1 to level 4 and the gain of level 1 to level 3, respectively. It is obviously that the NF of the first-stage amplifier has the largest effect on the overall noise. Hence, the input impedance is matched to the optimal noise source impedance so that the NF can be effectively controlled. However, this operation may result in the risk of the impedance point deviating from the maximum gain matching position. Therefore, for compromise,  $M$ -factor is introduced as [14]

$$M = \frac{F_1 - 1}{1 - 1/G_1}. \quad (2)$$

The compromise between the NF and the gain point is chosen when the  $M$ -factor reaches its minimum. Based on the above principles, a four-stage-cascaded LNA MMIC with the GaN HEMT in each stage is designed as exhibited in Fig. 1.

To further improve the gain flatness and robustness of the LNA, a negative feedback structure is used in the circuit design, which reduces the sensitivity of the process and increases the operating bandwidth. The resistance on the feed network is to suppress low-frequency oscillations and ensure the stability of the RF signal. The DC feed circuit at each stage is grounded through

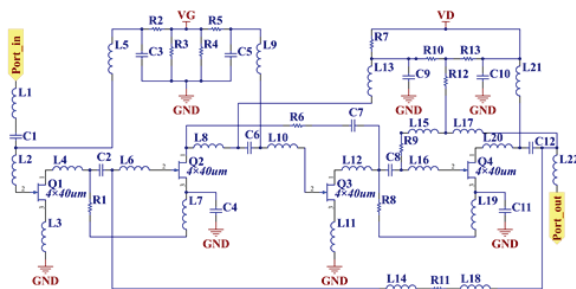


Fig. 1. Schematic of the proposed LNA.

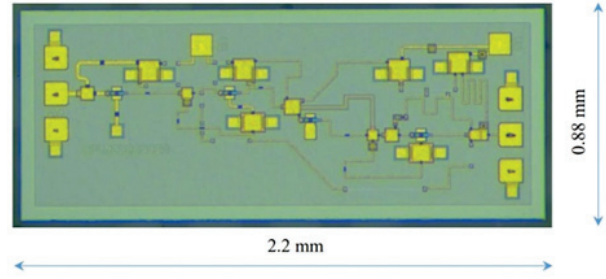


Fig. 2. SEM picture of the fabricated LNA.

the metal-insulator-metal capacitor. To prevent AC signal leakage, a choke inductor is added between the power and HEMT and can be determined by

$$L \geq 10 \times |Z_{load}| / 2\pi f_{cen}, \quad (3)$$

where  $f_{cen}$  is the central frequency and  $Z_{load}$  is the impedance. The DC power consumption is reduced by the multiplexing current. In this way, the leakage voltage of the tube core will be significantly decreased. Thus, the layout design is completed according to the schematic diagram with the chip size of  $2.2 \times 0.88 \times 0.05 \text{ mm}^3$ . The scanning electron microscopy (SEM) graph of LNA is exhibited in Fig. 2.

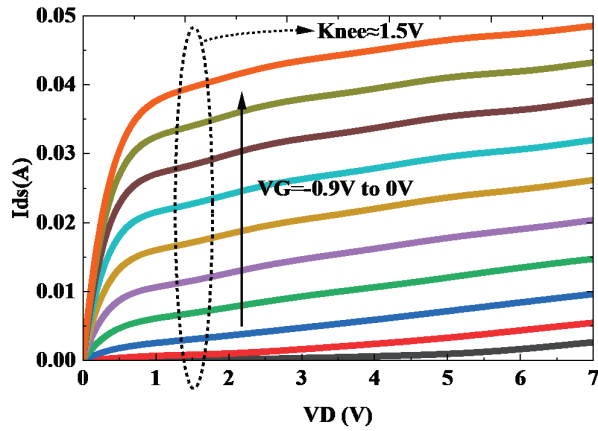
## III. MEASUREMENTS AND DISCUSSION

### A. Performances of GaN HEMT

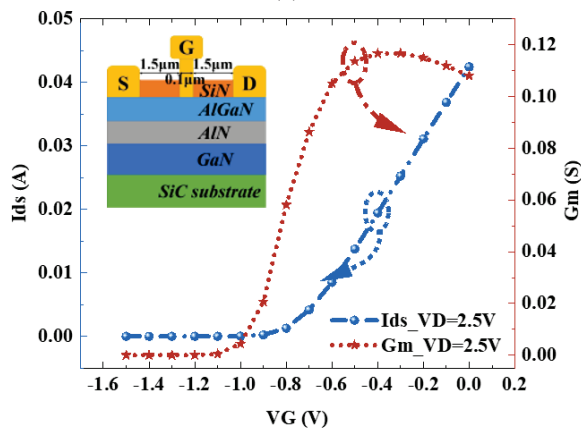
The measurement of the GaN HEMT is tested at ambient temperature ( $25^\circ\text{C}$ ) with a Shiel Environment TS200-SE probe station and a Keysight PNA-X N5245A vector network analyzer. Figure 3 (a) exhibits the I-V characteristics of the  $4 \times 40 \mu\text{m}$  GaN HEMT with the gate voltage changing from  $-0.9$  to  $0$  V, whose amplitude increment is  $0.1$  V. As can be seen from the curves, the knee voltage of the designed GaN HEMT is  $1.5$  V. Thus, these characteristics can achieve a lower noise coefficient and realize the current multiplexing at optimized supply voltages. Moreover, the transfer properties of the GaN HEMT are shown in Fig. 3 (b) with the maximum transconductance of  $750 \text{ ms/mm}$ , which benefits from the ultra-thin AlN barrier layer structure with strong polarization effects. The gain of the HEMT also reaches up to  $10$  dB at  $40$  GHz, as demonstrated in Fig. 4. Furthermore, the self-developed GaN HEMTs exhibit better performances than the GaAs HEMTs with the E-pHEMT process in the noise figure, which is maintained around  $1.0$  dB, shown in Fig. 5. Hence, this GaN HEMT can be used in the design of advanced LNA.

### B. Properties of the GaN LNA

The simulations are performed according to the layout of the GaN LNA with input power of  $2$  W. The test conditions are in agreement with the simulation conditions. Figure 6 demonstrates the comparison between simulations and measurements. It can be seen that the



(a)



(b)

Fig. 3. Output characteristics of the GaN HEMT in the proposed LNA.

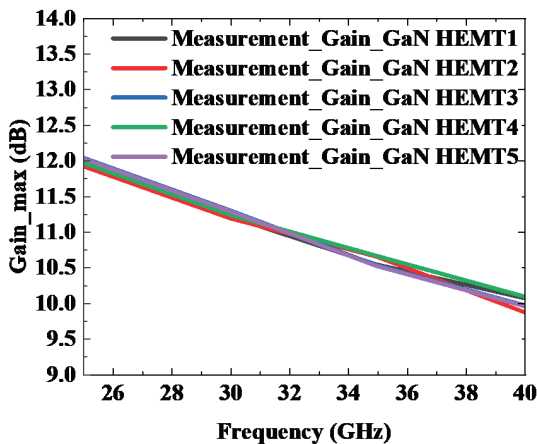


Fig. 4. Comparisons of gain characteristics for the proposed GaN LNA at different HEMT cores.

on-chip measurement of  $S_{21}$  is in great agreement with the simulation curve in the 25-40 GHz band. Remark-

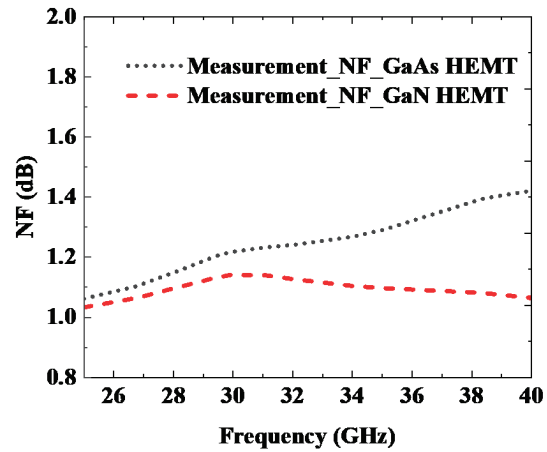
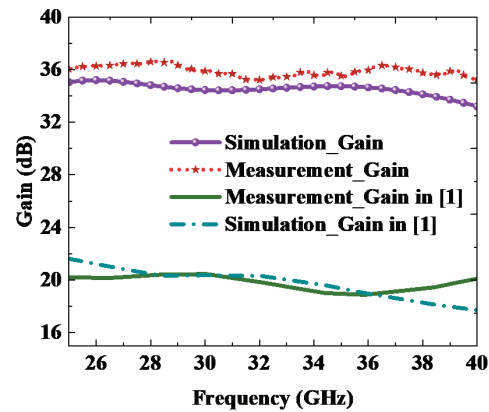
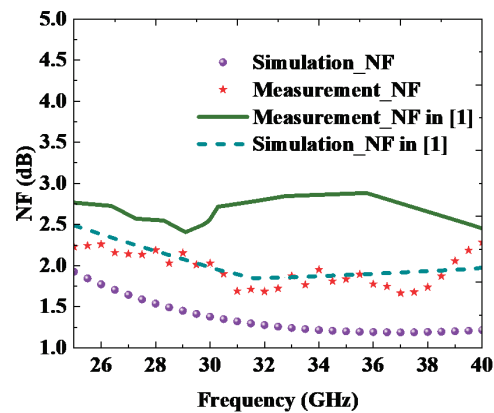


Fig. 5. Superior noise figure of the proposed GaN HEMT.



(a)



(b)

Fig. 6. Comparison of the performance of the proposed LNA: (a) The gain performance of the device and (b) the noise figure of the device.

ably, the proposed GaN LNA achieves a high gain of 35 dB, which is a distinct advantage over other reported

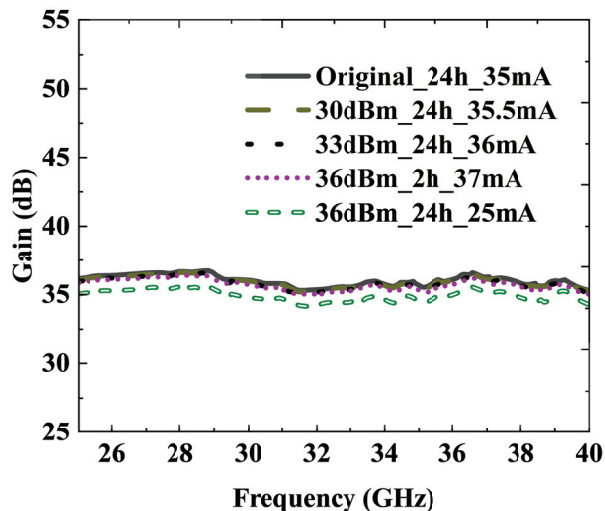


Fig. 7. Attack limit of the GaN LNA.

LNAs. Furthermore, by comparing the NF in the broadband band with the reported result in [1], the NF is reduced more than 0.5 dB, which is one of the advantages of the LNA designed in this paper. To further demonstrate the properties of the GaN LNA in high-power scenario, the attack limit of the GaN LNA is measured. As shown in Fig. 7, the proposed GaN LNA MMIC can withstand high power continuous waves up to 2 W for a long period of time without degradation in performance over the entire range of operating frequencies. As the input power increases, the performance of the LNA decreases and the working time increases. Compared to the LNA based on InP and GaAs [8], the GaN LNA exhibits better reliability under high-power conditions. This is mainly due to the outstanding thermal conductivity of the SiC substrate and the excellent high-power nature of the GaN material.

### C. Consistency test at different bias voltages

To demonstrate the excellent consistency, the performance of the GaN LNA is measured with different bias voltages. Meanwhile, the experiment is carried out at an ambient temperature of 25°C. A constant voltage of 5 V is applied in the drain and the gate voltage is swept from -0.3 V to -0.6 V at intervals of 0.1 V. The corresponding measured DC current is 52 mA, 41 mA, 31 mA, and 21 mA, respectively. The DC power consumption can be calculated as 0.15 W under typical operating conditions with a gate voltage of -0.5 V. This power consumption is extremely prominent for GaN LNA, which mainly benefits from the current multiplexing structure that enables GaN HEMTs to share the input power in series. This fabrication makes GaN LNA more competitive for applications in missile, airborne or space-borne circuits.

As can be seen in Fig. 8, the trends of the gain characteristics, NF and VSWR are essentially the same when different voltage values are applied to the gate. When VG is -0.6 V, the gain features and noise coefficients are more discrete. This is because the limited current density of the core is not sufficient to support marvelous amplification and noise properties. The VSWRs of the input port and the output port are consistent across the entire frequency band. As can be seen from Fig. 8 (b), the standing-wave properties do not become discrete with the difference of gate voltages.

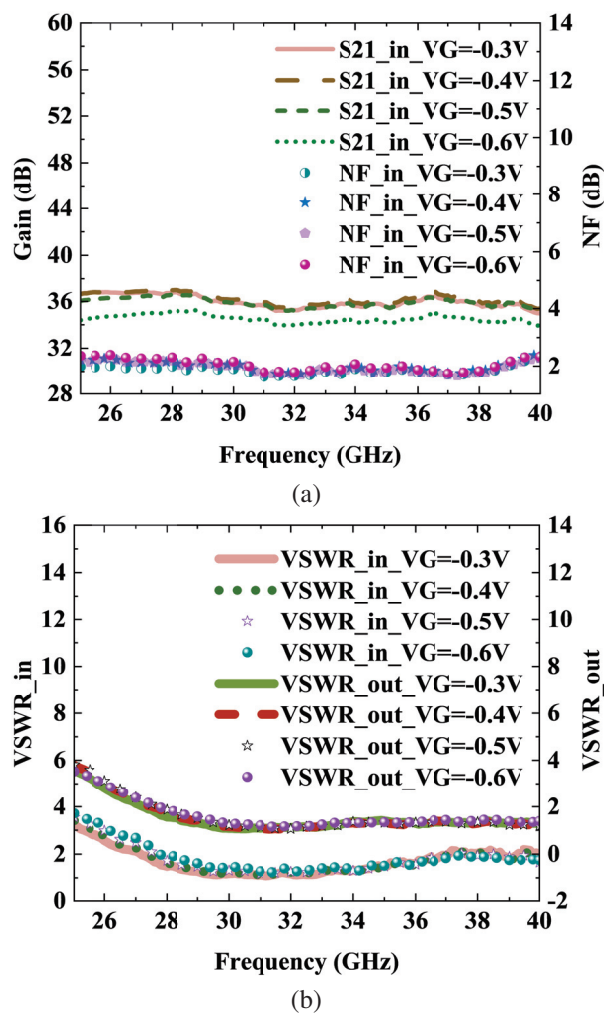


Fig. 8. Comparisons of (a) gain and NF and (b) VSWRs for the proposed GaN LNA at different bias voltages.

The variation trend of VSWR with frequency is the same for different gate voltages. This is mainly to optimize the gate width, gate spacing, and lead placement of the device during the layout design of the GaN LNA to obtain better gate resistance, gate capacitance, source resistance, and source inductance.

### D. High and low temperature performance

In this section, the electrical properties of the GaN LNA are measured at high and low temperatures to assess the operating conditions in harsh environments. The reliability of the GaN LNA is verified at different temperatures with the input power of 2 W, drain and gate voltages of 5 V and -0.5 V. The measured parameters are demonstrated in Fig. 9.

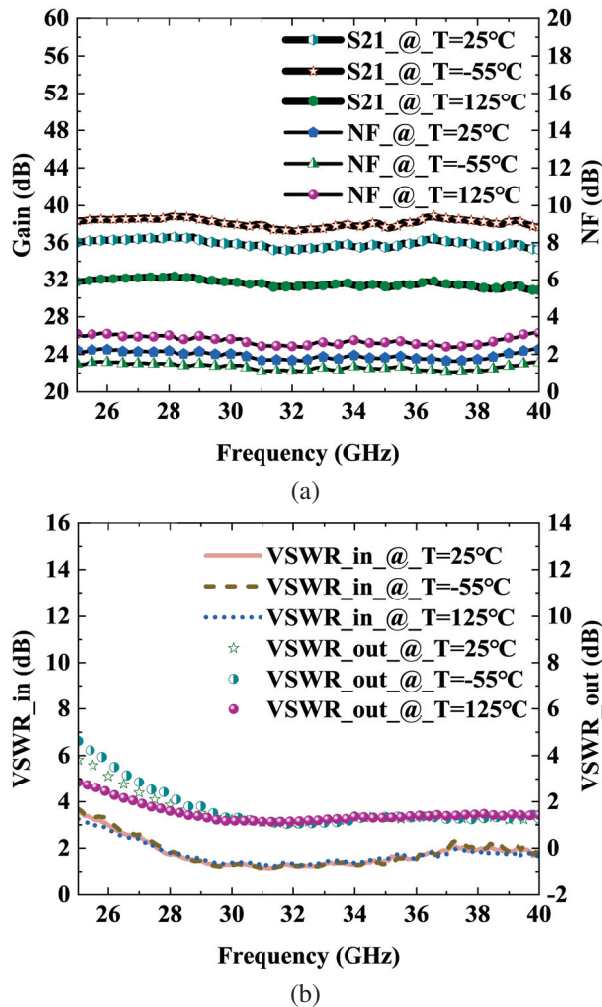


Fig. 9. Comparisons of (a) gain and NF and (b) VSWRs for the proposed GaN LNA at different temperatures.

Throughout the operating band, the gain of the GaN LNA decreases with increasing temperature. This is because the carrier mobility decreases with increasing temperature, leading to a reduction in the transconductance and a worsening of the gain. As can be seen from Fig. 9 (a), the NF of the LNA presents an opposite trend to the gain as a function of temperature, which is mainly due to the enhanced thermal vibration of the lattice and the scattering effect. Moreover, the VSWRs of the input port and output ports vary slightly with temperature in

the intermediate and high-frequency bands, while the dispersion is larger in the low-frequency band, as shown in Fig. 9 (b). This is caused by the fact that the temperature variability properties change the parasitic parameters and further affect the low-frequency properties.

### E. Comparisons with other reported Ka-band GaN LNAs

Some performances of the proposed GaN LNA are listed in Table 1 and compared with some previously reported representative advanced GaN LNAs, including the gain, noise figure, frequency band, DC power consumption, process, and chip core area. To our surprise, the designed GaN LNA monolithic microwave integrated circuit in this work not only realized a gain of 34-37 dB in the Ka-band, which is the highest value compared to other reported works, but also simultaneously possesses a low noise behavior of 1.6-2.2 dB. In addition, the desired DC power consumption of proposed GaN LNA MMIC in this work is as low as 0.15 W. [16] reports a lower DC power consumption, but it performs poorly in other aspects such as bandwidth, gain, and noise. These performances show that the proposed GaN LNA MMIC is a competitive component in millimeter-wave front ends.

Table 1: Performance comparisons of the GaN LNA

Ref.	Gain (dB)	NF (dB)	Frequency Band (GHz)	DC Power (W)	Process	Chip Core Area ( $\text{m}^2$ )
[1]	16-21.5	2.2-4.4	18-56	1.4	0.1 $\mu\text{m}$ GaN/Si	4*50
[3]	25-27	1.7-2.2	33-38	-	0.1 $\mu\text{m}$ GaN/Si	6*30/ 8*40/8*50
[4]	19.5-20.5	1.8-2	27-31	0.15	0.1 $\mu\text{m}$ GaN/Si	4*20
[6]	10-20	1.5-8	0.1-45	5.2	0.15 $\mu\text{m}$ GaN/SiC	-
[7]	21-25	2.4-2.9	25-31	0.3	0.15 $\mu\text{m}$ GaN/SiC	4*25
[15]	23-27	1.3-2.7	Full Ka-band	0.433	0.1 $\mu\text{m}$ GaN/Si	-
[16]	11-18	1.8-2.5	30-39.3	0.124	T4-A	4*20
[17]	20.2-24	2.42-2.56	26-30	0.32	0.15 $\mu\text{m}$ GaN/SiC	-
[18]	19.5-22.5	0.4-1.1	22-30	0.21	0.1 $\mu\text{m}$ GaN/Si	4*50
This work	34-37	1.6-2.2	25-40	0.15	0.1 $\mu\text{m}$ GaN/SiC	4*40

## IV. CONCLUSION

A state-of-the-art 25-40 GHz GaN-on-SiC LNA MMIC is presented in this paper. The LNA demonstrates superior broadband performance by implementing a four-stage-cascade structure using the MOCVD process, current multiplexing scheme, and source impedance matching. Covering the entire operating frequency band, the GaN LNA demonstrates a low NF of 1.6-2.2 dB, an excellent DC power consumption of 0.15 W, a high reliability in harsh temperature scenarios, and a superior

gain of 34-37 dB, offering unparalleled applications to directly integrated with GaN PA and switch to realize miniaturized, high-power, and reliable MMW front-end module.

### ACKNOWLEDGMENT

This work was supported in part by National Natural Science Foundation of China Grant 62201257, 62001231, 62025109, Primary Research & Development Plan of Jiangsu Province BE2022070, BE2022070-1, Jiangsu Province Natural Science Foundation under Grant BK20200467, Jiangsu Funding Program for Excellent Postdoctoral Talent and Postgraduate Research & Practice Innovation Program of Jiangsu Province KYCX22\_0438.

### REFERENCES

- [1] X. Tong, L. Zhang, P. Zheng, S. Zhang, J. Xu, and R. Wang, "An 18–56 GHz wideband GaN low-noise amplifier with 2.2–4.4-dB noise figure," *IEEE Microw. Wireless Compon. Lett.*, vol. 30, no. 12, pp. 1153-1156, Dec. 2020.
- [2] R. S. Pengelly, S. M. Wood, J. W. Milligan, S. T. Sheppard, and W. L. Pribble, "A review of GaN on SiC high electron-mobility power transistors and MMICs," *IEEE Trans. Microw. Theory Techn.*, vol. 60, no. 6, pp. 1764-1783, Feb. 2012.
- [3] C. Florian, P. A. Traverso, and A. Santarelli, "A Ka-Band MMIC LNA in GaN-on-Si 100-nm technology for high dynamic range radar receivers," *IEEE Microw. Wireless Compon. Lett.*, vol. 31, no. 2, pp. 161-164, Jan. 2021.
- [4] L. Pace, P. E. Longhi, W. Ciccognani, S. Colangeli, F. Vitulli, F. Deborgies, and E. Limiti, "DC power-optimized Ka-Band GaN-on-Si low-noise amplifier with 1.5 Db noise figure," *IEEE Microw. Wireless Compon. Lett.*, vol. 32, no. 6, pp. 555-558, Jan. 2022.
- [5] K. W. Kobayashi, V. Kumar, C. Campbell, S. Chen, and Y. Cao, "18-44GHz K/Ka-band robust-35.5 dBm reconfigurable 90nm GaN HEMT LNA," in *2020 IEEE BiCMOS and Compound Semiconductor Integrated Circuits and Technology Symposium (BCICTS)*, Monterey, CA, USA, Nov. 2020.
- [6] K. W. Kobayashi, D. Denninghoff, and D. Miller, "A novel 100 MHz–45 GHz input-termination-less distributed amplifier design with low-frequency low-noise and high linearity implemented with a 6 Inch 0.15 um GaN-SiC wafer process technology," *IEEE J. Solid-State Circuits*, vol. 51, no. 9, pp. 2017-2026, May 2016.
- [7] H. B. Ahn, H.-G. Ji, Y. Choi, S. Lee, D. M. Kang, and J. Han, "25–31 GHz GaN-based LNA MMIC employing hybrid-matching topology for 5G base station applications," *IEEE Microw. Wireless Compon. Lett.*, 2022 (early access).
- [8] X. Tong, R. Wang, S. Zhang, J. Xu, P. Zheng, and F.-X. Chen, "Degradation of Ka-band GaN LNA under high-input power stress: experimental and theoretical insights," *IEEE Trans. Electron Devices*, vol. 66, no. 12, pp. 5091-5096, Nov. 2019.
- [9] X. Tong, S. Zhang, J. Xu, P. Zheng, X. Shi, Y. Huang, O. Wang, and L. Luo, "18-31 GHz GaN wideband low noise amplifier (LNA) using a 0.1 m T-gate high electron mobility transistor (HEMT) process," *Int. J. RF Microw. Comput. Aided Eng.*, vol. 28, no. 8, pp. e214251-e214257, Aug. 2018.
- [10] S. Colangeli, W. Ciccognani, P. E. Longhi, L. Pace, J. Poulain, R. Leblanc, and E. Limiti, "Nondestructive, self-contained extraction method of parasitic resistances in HEMT devices," *IEEE Microw. Wireless Compon. Lett.*, vol. 68, no. 7, pp. 2571-2578, July 2020.
- [11] J.-G. Kim, C. Cho, E. Kim, J. S. Hwang, K.-H. Park, and J.-H. Lee, "High breakdown voltage and low-current dispersion in AlGaIn/GaN HEMTs with high-quality AlN buffer layer," *IEEE Trans. Electron Devices*, vol. 68, no. 4, pp. 1513-1517, Apr. 2021.
- [12] J. Qin, Q. Zhou, B. Liao, J. Chen, and H. Wang, "A comprehensive analysis of the 2-DEG transport properties in InxAl1-xN/AlN/GaN heterostructure: Experiments and numerical simulations," *IEEE Trans. Electron Devices*, vol. 67, no. 12, pp. 5427-5433, Dec. 2020.
- [13] P. Zheng, S. Zhang, J. Xu, R. Wang, and X. Tong, "A 23-31 GHz gallium nitride high-robustness low-noise amplifier with 1.1 dB noise figure and 28 dBm saturation output power," *Microw. Opt. Technol. Lett.*, vol. 62, no. 3, pp. 1077-1081, Nov. 2019.
- [14] R. Ludwig and P. Bretchko. *RF Circuit Design: Theory and Applications*. New York: Prentice Hall, 2000.
- [15] D. Parveg, M. Varonen, and M. Kantanen, "A full Ka-band GaN-on-Si low-noise amplifier," in *2020 50th European Microwave Conference (EuMC)*, Utrecht, Netherlands, Jan. 2021.
- [16] M. Micovic, D. Brown, D. Regan, J. C. Wong, J. Tai, A. Kurdoghlian, F. Herrault, Y. Tang, S. J. Burnham, H. H. Fung, A. Schmitz, I. Khalaf, D. Santos, E. M. Prophet, H. Bracamontes, C. McGuire, and R. Grabar, "Ka-band LNA MMIC's realized in  $f_{max} > 580$  GHz GaN HEMT technology," *2016 IEEE Compound Semiconductor Integr. Circuit Symp. (CSICS)*, Austin, TX, USA, Oct. 2016.
- [17] H. Ahn, H. Ji, D. Kang, S.-M. Son, S. Lee, and J. Han, "A 26–30 GHz GaN HEMT low-noise

amplifier employing a series inductor-based stability enhancement technique,” *Electronics*, vol. 11, no. 17, Sep. 2022.

- [18] X. Tong, S. Zhang, P. Zheng, Y. Huang, J. Xu, X. Shi, and R. Wang, “A 22-30 GHz GaN low-noise amplifier with 0.4–1.1-dB noise figure,” *IEEE Microw. Wireless Compon. Lett.*, vol. 29, no. 2, pp. 134-136, Jan. 2019.



**Zhou Dai** received the MSc. degree from Huazhong University of Science and Technology, Wuhan, China, in 2011. He is currently working toward the Ph.D. degree in electrical engineering in Nanjing University of Science and Technology, Nanjing, China. His research interest is in research on large dynamic and anti-jamming RF front-end ICs.



**Chunyu Li** was born in Jining, China, in 1996. He is currently pursuing the Ph.D. degree in electronic science and technology from Nanjing University of Science and Technology, Nanjing, China. His research interests include integrated circuit modeling, electronic design automation, and computational electromagnetics.



**Tiancheng Zhang** received the Ph.D. degree in communication engineering from the School of Electrical Engineering and Optical Technique, NJUST, Nanjing, China, in 2021. He is currently a postdoctoral fellow in the School of Microelectronics, NJUST, Nanjing, China. His research interests include semiconductor simulation, RF-integrated circuits, and computational electromagnetics.



**Huaguang Bao** received the B.S. and Ph.D. degrees in communication engineering from the School of Electrical Engineering and Optical Technique, Nanjing University of Science and Technology, Nanjing, China, in 2011 and 2017, respectively. From 2017 to 2019, he was a postdoctoral fellow in the Computational Electromagnetics and Antennas Research Laboratory, Department of Electrical Engineering, Pennsylvania State University (USA). He is currently an associate professor with the School of Microelectronics, Nanjing University of Science and Technology. He serves as a reviewer for *IEEE Transactions on Antennas and Propagation*, *IEEE Transactions on Microwave Theory and Techniques*, *Physics of Plasmas*, etc. His research interests include semiconductor simulation, RF-integrated circuits, and computational electromagnetics.